Studies of Structural Patterns at Phase Transitions

Thesis submitted by

Nigel Blair Wilding

For the Degree of

Doctor of Philosophy

Department of Physics
The University of Edinburgh

November 1991

Declaration

The work described in chapter 3 was performed in collaboration with A D Bruce. With this exception, the research described in this thesis was the unaided work of the author.

Signed

N B Wilding

Acknowledgements

I take great pleasure in recording my appreciation of those who have helped and generously supported me throughout the last three years. I am especially grateful to the following:

My supervisor, Professor G S Pawley for creating valuable opportunities and for allowing me 'free rein' to follow the path of my choice;

Dr. P D Hatton for his guidance, cheerfulness and optimism especially when things weren't going to plan, and for introducing me to high-pressure neutron powder diffraction and the restaurants of Grenoble;

Dr. A D Bruce for patient assistance, inspiration and for helping to make the difficult appear easy.

In addition I thank all the above mentioned, for proof reading this thesis and for helpful comments during its preparation. The financial support of a Colin and Ethel Gordon Scholarship from the University of Edinburgh is gratefully acknowledged.

I would also like to take this opportunity to express general thanks to all those friends and colleagues in the Physics department at Edinburgh whose companionship has enriched the last three years.

Lastly and above all, I am grateful to my parents for their unfailing support and encouragement throughout, and to whom this thesis is dedicated.

Abstract

The work described in this thesis comprises two distinct components. In the first part, Monte-Carlo computer simulation methods are employed within a finite-size scaling framework to investigate both universal and non-universal behaviour in two scalar models, the 1-d ϕ^4 model and the 2-d Lennard-Jones fluid. In both these models the properties of interest are obtained from studies of the large-length-scale configurational patterns via measurements of the probability distribution function (PDF) of the coarse-grained (block) ordering variable.

For the 1-d ϕ^4 model, simulations are employed to obtain the block PDF of the spin variable. This function is shown to map onto an analytically-derived expression for the block PDF of the 1-d Ising chain, thus exposing the model's essentially Ising-like character. It is further demonstrated that the corrections to the limiting form of the block PDF reflect system-specific features of the 1-d ϕ^4 model associated with its elementary excitations.

In the 2-d Lennard-Jones fluid, the combined use of simulation and finite-size scaling is shown to provide a powerful method for accurately determining the location of the liquid-vapour coexistence curve and critical point. At the critical point, the limiting form of the coarse-grained density distribution is found to collapse onto a previously determined function characteristic of the 2-d Ising model, thereby confirming and clarifying fluid-magnet universality. Clear evidence is also presented for mixing of the temperature and chemical potential in the two relevant scaling fields–a phenomenon responsible for the failure of the law of rectilinear diameter. As an addendum, a discussion is given of the prospects for generalising to fluids, the cluster updating techniques recently developed to reduce critical slowing down in simulations of spin systems.

The second distinct part of this thesis is concerned with a neutron powder diffraction study of the structural patterns of crystalline cyclohexane. The use of automatic indexing techniques to determine the unit cell and spacegroup of two hitherto unsolved high-pressure phases of cyclohexane is reported. The deduction of

atomic coordinates from lattice energy minimisation calculations and constrained least squares refinement is then described and the limitations of this technique for structure solution are discussed. Finally the physical mechanisms determining the deduced structures of cyclohexane are considered in relation to the general factors believed to influence the adopted crystal structures of simple organic molecular systems.

Contents

List of Figures

Chapter 1

Static Critical Phenomena–an Overview

1.1 Preamble

It seems appropriate to preface this work with a general discussion of those aspects of critical phenomena which will prove relevant to the present studies. Owing to the wide-ranging nature of the background material it will not be possible to perform an exhaustive, or even extensive review. Instead this chapter will merely seek to provide an overview of principal aspects of the theory, placing particular emphasis on those topics which serve to equip the reader for an adequate appreciation of the material to be presented in succeeding chapters. For a more comprehensive coverage, the reader is referred to the introductory reviews appearing in the literature (see e.g. Stanley [1], Ma [2], Wallace and Zia [3], and Fisher [4]).

1.2 Introduction

A wide variety of physical systems undergo rearrangements of their internal constituents in response to the thermodynamic conditions to which they are subject. Two classic examples of systems displaying such phase transitions are the ferromagnet and fluid systems. As the temperature of a ferromagnet is increased, its

magnetic moment is observed to decrease smoothly, until at a certain temperature known as the critical temperature, it vanishes altogether. Similarly, a change of state from liquid to gas can be induced in a fluid system (though not in an ideal gas) simply by raising the temperature. Typically the liquid-vapour transition is abrupt, reflecting the large density difference between the states either side of the transition. However the abruptness of this transition can be reduced by applying pressure. At one particular pressure and temperature the discontinuity in the density difference between the two states vanishes. These conditions of pressure and temperature serve to locate the critical point for the fluid.

In the vicinity of a critical point a system will exhibit a variety of remarkable effects known collectively as critical phenomena. Principal among these effects is the divergence of thermodynamic response functions such as the specific heat and the compressibility or susceptibility. It transpires that the origin of the singularities in these quantities can be traced to large-length-scale co-operative effects between the microscopic constituents of the system. The recalcitrant problem posed by the critical region is how best to incorporate such collective effects within the framework of a rigorous mathematical theory that affords both physical insight and quantitative explanation of the observed phenomena. This matter has been (and still is!) the subject of intense theoretical activity.

The importance of the critical point stems largely from the fact that many of the phenomena observed in its vicinity are believed to be common to a whole range of apparently quite disparate physical systems. This observation implies a profound underlying similarity among physical systems at criticality, regardless of many aspects of their distinctive microscopic nature. These ideas have found formal expression in the so-called 'universality hypothesis' which, since its inception some 25 years ago, has enjoyed considerable success.

In this chapter, principal aspects of the contemporary theoretical viewpoint of static critical phenomena will be reviewed. The ideas of power laws, critical exponents and their relationship to scaling phenomena will be described and set within the context of the powerful renormalisation group technique. The notion of univer-

sality as a phenomenological hypothesis will be introduced and its implications for real and model systems will be explored. Finally, the utility of finite-size scaling methods for computer studies of critical phenomena will be discussed, culminating in the introduction of a specific technique suitable for exposing universality in scalar models.

1.3 The Approach to Criticality

It is a matter of experimental fact that the approach to criticality in a given system is characterised by the divergence of various thermodynamic observables. The archetypal example of a critical system is the ferromagnet, whose critical temperature will be denoted as T_c. For temperatures close to T_c and in vanishing external field ($H = 0$), the response function (in this case the magnetic susceptibility χ) is found to be a singular function, diverging as the power γ of the reduced temperature t $\equiv (T - T_c)/T_c$:-

$$\chi \propto t^{-\gamma} \qquad (H = 0) \tag{1.1a}$$

Similarly, the correlation length ξ, i.e. the distance over which fluctuations of the magnetic moments are correlated, is observed to diverge with an exponent ν.

$$\xi \propto t^{-\nu} \qquad (T > T_c, H = 0) \tag{1.1b}$$

Power law behaviour is also found in the behaviour of the order parameter which measures the degree of order in a system. For the case of a simple magnetic system, the order parameter is taken to be the spontaneous magnetisation m. At temperatures below T_c, the order parameter is non-zero reflecting the presence of a preponderance of magnetic moments (spins) which are mutually aligned. As the critical temperature is approached from below, thermal disorder increases and the magnetisation tends smoothly to zero.

$$m \propto t^{\beta} \qquad (T < T_c, H = 0) \tag{1.1c}$$

The quantities γ, ν, β in the above equations are known as critical exponents. They serve to control the rate at which the various thermodynamic quantities change on the approach to criticality. Further power law behaviour is found in the behaviour of the specific heat (whose exponent is conventionally denoted α) and in the behaviour of the magnetisation as a function of an applied magnetic field (exponent δ).

Remarkably, the form of singular behaviour observed at criticality for the example ferromagnet also occurs in qualitatively quite different systems such as the fluid system. All that is required to obtain the corresponding power law relationships for the fluid is to substitute the analogous thermodynamic quantities in to the above equations. Accordingly the magnetisation is replaced by the density difference $\rho_{liq} - \rho_{gas}$ while the susceptibility is replaced by the isothermal compressibility. The approach to criticality in a variety of qualitatively quite different systems can therefore be expressed in terms of a set of critical exponents describing the power law behaviour for that system.

The principal aim of theories of critical point phenomena is to provide a sound theoretical basis both for the existence of power law behaviour and the factors governing the observed values of critical exponents. Historically, the first step towards these goals was taken by the static scaling hypothesis.

1.4 The Static Scaling Hypothesis

The static scaling hypothesis is essentially a plausible conjecture which appears to be consistent with observed phenomena [5] [6]. Its basic assertion is that the singular dependence of the response functions enters through a single variable, namely the reduced temperature (or alternatively the correlation length ξ) and that any other dependence on temperature is smooth and can be regarded as

constant over a small temperature range around T_c.

The basis for scaling phenomena in near-critical systems is expressed in the claim that: in the neighbourhood of a critical point, the basic thermodynamic functions (most notably the Gibbs Free energy) are generalised homogeneous functions of their variables. For such functions one can always deduce a scaling law such that by an appropriate change of scale, the dependence on two variables (e.g. the temperature and applied field) can be reduced to dependence on one new variable. This claim may be warranted by the following general argument.

A function of two variables $f(u,v)$ is called a generalised homogeneous function if it has the property

$$f(\lambda^a u, \lambda^b v) = \lambda f(u,v) \tag{1.2}$$

for all λ, where the parameters a and b (known as scaling parameters) are constants. Now, the arbitrary scale factor λ can be redefined without loss of generality as $\lambda^a = u^{-1}$ giving

$$f(u,v) = u^{1/a} f(1, \frac{v}{u^{b/a}}) \tag{1.3}$$

A corresponding relation is obtained by choosing the rescaling to be $\lambda^b = v^{-1}$.

$$f(u,v) = v^{1/b} f(\frac{u}{v^{a/b}}, 1) \tag{1.4}$$

This equation demonstrates that $f(u,v)$ indeed satisfies a simple power law in *one* variable, subject to the constraint that $u/v^{a/b}$ is a constant. It should be stressed, however, that such a scaling relation specifies neither the function f nor the parameters a and b.

Now, the static scaling hypothesis asserts that in the critical region, the singular part of the Gibbs free energy G is a generalised homogeneous function of the ther-

modynamic fields. Remaining with the example ferromagnet, the following *ad hoc* scaling assumption [1] can then be made in terms of the reduced temperature and the dimensionless applied field h:-

$$G(\lambda^a t, \lambda^b h) = \lambda G(t, h) \tag{1.5}$$

Of course, the Gibbs free energy provides the route to all thermodynamic functions of interest. Hence an expression for the magnetisation can be obtained simply by taking the field derivative of the Gibbs function for zero applied field $h = 0$

$$m(t, 0) = (-t)^{(1-b)/a} m(-1, 0) \tag{1.6}$$

where the particular choice $\lambda = (-1/t)^{1/a}$ has been made. Equation (1.1c) then allows identification of the exponent β in terms of the scaling parameters a and b.

$$\beta = \frac{1-b}{a} \tag{1.7}$$

By taking appropriate derivatives of the Gibbs function, other relations between scaling parameters and critical exponents may be deduced. Such calculations yield the results $\delta = b/(1-b)$, $\gamma = (2b-1)/a$ and $\alpha = (2a-1)/a$. Relationships between the critical exponents themselves can be obtained trivially by eliminating the scaling parameters from these equations. The principal results (known as "scaling laws") are:-

$$\alpha + \beta(\delta + 1) = 2 \tag{1.8}$$

$$\alpha + 2\beta + \gamma = 2 \tag{1.9}$$

Thus, provided all critical exponents can be expressed in terms of the scaling parameters a and b, then only two critical exponents need be specified, for all others to be deduced. Of course these scaling laws are also expected to hold

for the appropriate thermodynamic functions of analogous systems such as the liquid-gas critical point.

1.4.1 Experimental Verification of Scaling

The validity of the scaling hypothesis finds startling verification in experiment. To facilitate contact with experimental data for real systems, it is first necessary to obtain a scaled equation of state. For a magnetic system the appropriate scaling relation is

$$m(t, h) = \lambda^{b-1} m(\lambda^a t, \lambda^b h) \tag{1.10}$$

Making the substitution $\lambda = t^{-1/a}$ and eliminating the scaling parameters a and b in favour of the exponents β and δ gives

$$\frac{m(t,h)}{t^\beta} = m(1, \frac{h}{t^{\beta\delta}}) \tag{1.11}$$

In fact this last equation is really only a function of one variable. This feature can be brought out by the following redefinition

$$F(H) \equiv m(1, H) \tag{1.12}$$

where $H \equiv t^{-\beta\delta} h(t, M)$.

Measured m-h isotherms for a particular magnetic system, can be used to demonstrate scaling by plotting the data against $M = t^{-\beta} m(t, h)$ and $H = t^{\beta\delta} h(t, M)$. Under this scale transformation, it is found that all isotherms (for t close to zero) coincide to within experimental error [1]. Reassuringly, similar results are found using the scaled equation of state of simple fluid systems such as He^3 or Xe [7].

In summary, the static scaling hypothesis is remarkably successful in providing a foundation for the observation of power laws and scaling phenomena. However,

it furnishes little or no guidance regarding the role of co-operative phenomena at the critical point. In particular it provides no means for calculating the values of the critical exponents appropriate to given model systems.

1.5 Models and Approximations

In order to probe the properties of the critical region, it is common to appeal to simplified model systems whose behaviour parallels that of real materials. The sophistication of any particular model depends on the properties of the system it is supposed to represent. The simplest model to exhibit critical phenomena is the two-dimensional Ising model of a ferromagnet. Actual physical realisations of 2-d magnetic systems do exist in the form of layered ferromagnets such as K_2CoF_4, so the 2-d Ising model is of more than just technical relevance [8].

The 2-d Ising model envisages a regular arrangement of magnetic moments or 'spins' on an infinite plane. Each spin can take two values, $+1$ ('up' spins) or -1 ('down' spins) and is assumed to interact with its nearest neighbours according to the Hamiltonian

$$\mathcal{H}_I = -J \sum_{<ij>} s_i s_j \tag{1.13}$$

where $J > 0$ measures the strength of the coupling between spins and the sum extends over nearest neighbour spins s_i and s_j.

The fact that the Ising model displays a phase transition may be understood in a qualitative sense as follows. At low temperatures there is little thermal disorder and the free energy is a minimum when there is a preponderance of aligned spins and hence a net spontaneous magnetic moment. As the temperature is raised, thermal disorder increases until at a certain temperature T_c, entropy drives the system through a continuous phase transition to a disordered spin arrangement with zero net magnetisation. Although each spin interacts only with its nearest

neighbours, the phase transition occurs due to cooperative effects among a large number of spins. In the neighbourhood of the transition temperature these cooperative effects engender fluctuations that can extend over all length-scales from the lattice spacing up to the correlation length.

Although the 2-d Ising model may appear at first sight to be an excessively simplistic portrayal of a real magnetic system it transpires that close to criticality, many physical observables are not materially influenced by the actual nature of the microscopic interactions. The Ising model therefore provides a simple, yet quantitatively accurate representation of the critical properties of a whole range of real magnetic (and indeed fluid) systems. This universal feature of the model is largely responsible for its ubiquity in the field of critical phenomena.

Of the wide variety of models of interest to the critical point theorist, the majority have shown themselves intractable to direct analytic assault. In a very limited number of instances models have been solved exactly, yielding the critical exponents and the transition temperature [9]. The 2-d spin-$\frac{1}{2}$ Ising model is certainly the most celebrated such example, its principal critical exponents are found to be $\beta = \frac{1}{8}, \nu = 1, \gamma = \frac{7}{4}$. Unfortunately such solutions rarely afford deep insight to the general framework of criticality although they do act as an invaluable test-bed for new and existing theories.

For many years prior to the introduction of the renormalisation group method, the bedrock of information about the criticality in model systems was provided by series expansion techniques. These methods seek to deduce results for the critical region using known results obtained away from criticality. One simple example is the high-temperature series which expresses the Boltzmann factor in terms of a temperature expansion with $1/T$ assumed small.

$$\exp(-\mathcal{H}/k_B T) = 1 - \mathcal{H}/k_B T + \frac{1}{2!}(\mathcal{H}/k_B T)^2 + ... \tag{1.14}$$

Successively higher terms in this series can be regarded as characterising correla-

tions over successively larger distances. Known results for the high-temperature fully disordered phase can be applied to permit the (rather laborious) calculation of the partition function using the significant terms in this expansion. This procedure can yield surprisingly accurate numerical results although it is typical that the expansions break down close to the critical point, a failure that can be traced back to the divergent correlation length. Series expansions are dealt with in some detail by Gaunt [10].

1.6 The Renormalisation Group

The crucial feature of the critical region is the existence of correlated microstructure on *all* length-scales up to and including the correlation length. Such a profusion of degrees of freedom can only be accurately characterised by a very large number of variables. As already described, approximation schemes fail in the critical region because they only incorporate interactions among a few spins, while neglecting correlations over larger distances. Similarly, the scaling hypothesis fails to provide more than a qualitative insight into the nature of criticality because it focuses on only one length-scale, namely the correlation length itself. Evidently a fuller understanding of the critical region may only be attained by taking account of the existence of structure on all length-scales. Such a scheme is provided by the renormalisation group method, pioneered by K.G. Wilson, which stands today as the cornerstone of the modern theory of critical phenomena.

1.6.1 Philosophy and Methodology

The central thesis of the renormalisation group (RG) method is a stepwise elimination of the degrees of freedom of the system on successively larger length-scales. Many specific realisations of this procedure have been formulated but all contain this one basic ingredient. For illustrative convenience, real-space RG techniques will be described for a lattice of N spins $\{\sigma_x\}$. Corresponding arguments can

however be developed in Fourier space and for continuous (off-lattice) systems.

The RG method is defined for a *near-critical* system in terms of a two stage process involving a coarse-graining operation followed by a rescaling. The first step, the coarse-graining operation, entails the elimination of a number of neighbouring spins in favour of a single new spin chosen to reproduce the effect of its environment. One common method for achieving this is to perform a partial trace over $(N - N')$ of the original spin variables $\{\sigma_x\}$, in such a way that the N' surviving spins $\{\sigma_{x'}\}$ form a new lattice with spacing larger than that of the physical system by a factor $b \gg 1$. Absorbing factors of $(-k_B T)^{-1}$ one can write

$$\exp(\mathcal{H}') = Tr'_{N-N'}(\exp(\mathcal{H})) \tag{1.15}$$

where the effective Hamiltonian $\mathcal{H}'$ can be viewed as characterising the interaction among those spin variables that survive the coarse-graining procedure.

Clearly, the coarse-graining operation reduces the number of spin variables from N to $N' = N/b^d$. In order to preserve the spatial density of spins, it is therefore necessary that all surviving spins have their spatial vectors rescaled by the factor b. Explicitly therefore, the lattice spacing of surviving spins is shrunk back to the lattice size of the original system before coarse-graining.

$$x' = x/b \tag{1.16}$$

The essential condition to be satisfied by the RG operation is that the partition function must be preserved

$$Z_{N'}(\mathcal{H}') = Z_N(\mathcal{H}) \tag{1.17}$$

In order to satisfy this condition and hence maintain the basic spin-fluctuation amplitude, the scales of the coarse-grained variables must be amplified by a constant factor $\Lambda(b)$.

$$\sigma_x \rightarrow \sigma_{x'} = \Lambda(b)\sigma_x \tag{1.18}$$

This rescaling, which completes the RG transformation, ensures that configurations of coarse-grained spins appear with the correct relative probability via the effective Hamiltonian $\mathcal{H}'$.

Consider now the Hamiltonian representing the system before and after the RG operation. For generality it is necessary to assume that the Hamiltonian $\mathcal{H}$ of the original system is a function of a set of coupling constants $\{K_i\} \equiv \{J_i/k_BT\}$, reflecting the possibility of many different types of spin interactions. The effective Hamiltonian $\mathcal{H}'$ of the coarse-grained system is also expressed in terms of a set of couplings which characterise the interactions among the coarse-grained spins σ'_x. In general however, the set of couplings appropriate to the coarse-grained system differs from the set for the initial system although they implicitly encapsulate all the information regarding the initial system. The most that can be said about the new couplings is that they are some function of the old couplings

$$K'_i = f(K_1, K_2, ...) \equiv f(\mathbf{K}) \tag{1.19}$$

Symbolically, the RG transformation can be expressed by some function $\Re_b$ relating the effective Hamiltonian of the coarse-grained variables to the Hamiltonian before coarse-graining

$$\mathcal{H}' = \Re_b(\mathcal{H}) \tag{1.20}$$

Furthermore as its name implies, it is possible to implement the RG operation iteratively, such that a fraction b^d of the coarse-grained spins surviving the first application are themselves eliminated under a second RG operation. However for this to succeed, it is necessary that two applications of the operation with scale-factor b is equivalent to a single application with scale-factor b^2.

$$\Re_b \Re_b = \Re_{b^2} \tag{1.21}$$

The fulfillment of this condition is contingent upon $\Lambda(b)$ taking the form

$$\Lambda(b) \sim b^c \tag{1.22}$$

where c is independent of b.

By now it should be apparent that the net effect of the RG transformation is to reduce the number of length-scales associated with the *description* of the system. At each successive RG iteration, fluctuations on progressively larger length scales are subsumed, thereby reducing the ratio of the correlation length to the lattice spacing. Effectively therefore, the RG may be viewed as transforming a system close to criticality into one further from criticality. Unfortunately, the form of $\mathcal{H}'$ can no-more be calculated exactly than could the original Hamiltonian $\mathcal{H}$. However, because the renormalised Hamiltonian is less critical than the original Hamiltonian, the approximation schemes that fail close to criticality *are* potentially of use for solving the Hamiltonian of the renormalised system.

1.7 The Fixed Point Concept

Consider now the situation precisely at the critical point. Since the correlation length is infinite at criticality, a finite number of coarse-graining steps cannot decrease the ratio of the lattice spacing to the correlation length. Thus after any number of RG iterations, the system is still at its critical point. Within the RG framework, this phenomenon of scale invariance can be formally expressed in terms of the effective Hamiltonian which controls the coarse-grained coordinates

$$\mathcal{H}^* = \Re_b \mathcal{H}^* \tag{1.23}$$

where $\mathcal{H}^*$ represents a Hamiltonian which is invariant under the RG. The solution to this equation (in terms of the effective couplings K^* which serve to define $\mathcal{H}^*$) is known as a fixed point. It will usually be found that a fixed point solution exists only for one particular choice of the auxiliary scaling operation $\Lambda(b) \sim b^c$. It may be shown (appendix A.1) that the appropriate choice is $c = -\beta/\nu$.

The fixed point concept can best be elucidated by considering the space of coupling constants of the system. In general, this coupling space will span an infinite number of dimensions, reflecting the possibility of many different types of spin interaction, not only among the 'bare' spins, but also among the coarse-grained spins. According to the RG theory, there exists within the full coupling space a large subspace known as the critical surface. This critical surface is defined as the set of all coupling constants (in units of $1/k_B T_c$) which locate the critical temperature for models of a given class. As previously claimed, the effect of the RG transformation on the effective coupling constants of a system is, in general, to produce a new set of couplings. However, the ratio of lattice size to correlation length for a critical system is unchanged by the RG operation–the system remains at criticality. Thus if the set of effective couplings $\{K_i\}$ at each successive RG step is represented by a point on the critical surface, points for a series of RG steps trace out a trajectory or flow-line *on* the critical surface. This flow-line emanates from the point corresponding to the critical couplings of the initial system, and for b sufficiently large, it converges on the fixed point. The existence of this limit reflects the fact that for large enough b the effective Hamiltonian $\mathcal{H}^*$ is invariant under the RG.

1.8 Perturbations, Exponents and Scaling

The role of critical exponents in determining the characteristic near-critical behaviour of a system emerges in a natural way from the RG formalism. To appreciate this, it is instructive to consider the behaviour of points in coupling space that lie close to the fixed point. This can be achieved by expanding $f_i(\mathbf{K})$ around

$\mathbf{K}^*$. To linear order,

$$K_i' \approx f_i(\mathbf{K}^*) + \frac{\partial f_i}{\partial K_j}(\mathbf{K}^*) \cdot (K - K^*)_j \tag{1.24}$$

where the summation convention has been assumed. At the fixed point itself $K_i^* = f_i(\mathbf{K}^*)$, thus

$$(K' - K^*)_i = M_{ij}(K - K^*)_j \tag{1.25}$$

where

$$M_{ij} = \frac{\partial f_i}{\partial K_j}(\mathbf{K}^*) \tag{1.26}$$

The eigenvalues $\Lambda_a(b)$ and eigenvectors $v_j^{(a)}$ of M_{ij} are defined by the following eigenvalue equation:-

$$\sum_j v_j^{(a)} M_{ji} = \Lambda_a(b) v_i^{(a)} \qquad a = 1, 2, ... \tag{1.27}$$

Perturbations from the fixed point can then be expanded in the basis of these eigenvectors.

$$\mathbf{K} - \mathbf{K}^* = \sum_a \mu_a v_a \tag{1.28}$$

Equation (1.25) thus becomes

$$\mathbf{K}' - \mathbf{K}^* = \sum_a \mu_a' v_a \tag{1.29}$$

with the perturbation components μ_a satisfying the relation

$$\mu_a'(b) = \Lambda_a(b) \mu_a \tag{1.30}$$

These perturbation components are known as 'scaling fields' and equation (1.30) is a recursion formula describing their evolution under the coarse-graining operation. Dependent on the value of $\Lambda_a(b)$, the μ_a are expected to exhibit differing transformation behaviour. For the case when $\Lambda_a(b) > 1$, it follows that $\mu'_a > \mu_a$ and hence the effective coupling $\mathbf{K}'$ is further from $\mathbf{K}^*$ than was $\mathbf{K}$. The scaling field associated with this eigenvalue is therefore amplified by the RG and the effective coupling is driven away from its fixed point value. Such a scaling field is said to be '*relevant*'. Conversely, when $\Lambda_a(b) < 1$, it follows that $\mu'_a < \mu_a$ and the effective coupling moves closer to the fixed point value. The scaling field associated with the eigenvalue in this latter case is therefore diminished under the RG operation and is said to be *irrelevant* to the fixed point.

Within the construct of the critical surface, the eigenvectors of the coupling combination matrix M_{ij} define special directions relative to the critical surface. Specifically, the eigenvectors associated with relevant scaling fields are normal to the critical surface, while those associated with irrelevant scaling fields lie within the critical surface itself. Under the coarse-graining operation, the flow of the effective coupling will be modified according to the values of the relevant and irrelevant scaling fields. Consider the case of a finite relevant scaling field, corresponding to a small but finite deviation from criticality. Initially the effective coupling will flow towards the fixed point along the direction of the irrelevant eigenvector. However deviations from criticality are amplified by the RG operation which reduces the correlation length. Hence, as the RG is iterated the coupling flow ultimately diverges away from the fixed point *along* the eigenvector corresponding to the relevant scaling field. Only when all the relevant scaling field are zero will the effective coupling flow asymptotically approach the fixed point. Figure 1.1 shows a simplified schematic representation of this process. The most important couplings in the original system are represented on the ordinate, while all others describing the effective Hamiltonian are represented on the abscissa. It is assumed that the original Hamiltonian of the 'bare' systems is characterised by a single nearest-neighbour coupling constant (c.f. the Ising model).

Thus a given system is unstable with respect to perturbations out of the criti-

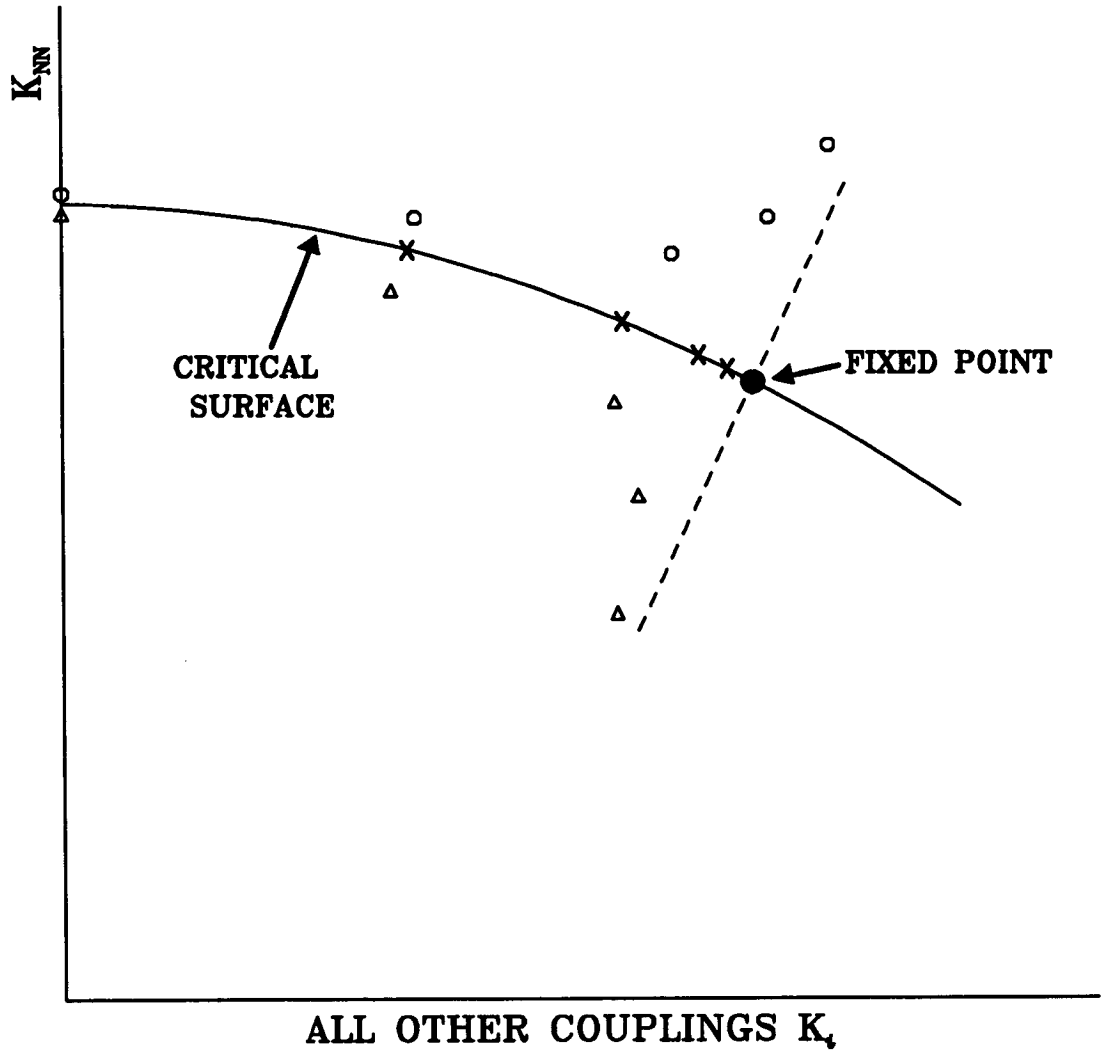

Figure 1.1: Schematic representation of the flow-process of the effective Hamiltonian in coupling space under the RG transformation. The vertical axis corresponds to the nearest-neighbour coupling constant, while all other coupling constants are represented by the horizontal axis. For sufficiently large b, the effective coupling flow for slightly super-critical ($\triangle$) and slightly sub-critical (o) systems diverges along the direction of the relevant eigenvector of the temperature scaling field (shown as a broken line). Precisely at criticality the effective coupling flow ($\times$) asymptotically converges on the fixed point.

cal surface but stable to perturbations within the critical surface. From this it should be clear, that the relevant or unstable scaling fields represent precisely those quantities that have to be tuned in order to be at the critical point. For magnetic systems there are, in general, two relevant scaling fields which can be identified with the reduced temperature and the applied field. The physical interpretation of the irrelevant scaling fields is however slightly less tangible, they measure the extent to which the value of the scale factor b fails as an approximation to the asymptotic limit. This measure is usually termed the 'correction to scaling'.

The significance of critical exponents, can now be re-examined in the light of the foregoing analysis. Firstly it should be evident that the critical exponents (β, γ, ν etc) are intimately related to the eigenvalues $\Lambda_a(b)$ of the relevant perturbation eigenvectors. Intuitively this can be deduced from equation (1.30) which shows that the eigenvalues determine the rate at which the deviation from criticality grows under the RG transformation. This, of course, is exactly the role played by the critical exponents themselves. As a concrete example, consider the scaling field μ_1 which is assumed to correspond to perturbations of T away from T_c.

$$\mu_1 \propto (T - T_c) \tag{1.31}$$

Hence from the recursion formula (1.30)

$$(T - T_c)' = \Lambda_1(b)(T - T_c) \tag{1.32}$$

However, under the RG transformation the correlation length of a near-critical system is reduced by a factor of the coarse-graining scale factor b.

$$\xi' = b^{-1}\xi \tag{1.33}$$

Recalling the behaviour of the correlation length $\xi \propto (T - T_c)^{-\nu}$, then shows that

$$\Lambda_1(b) \propto b^{1/\nu} \tag{1.34}$$

This is one example of a more general result, namely that the eigenvalues $\Lambda_a(b)$ take the form

$$\Lambda_a(b) \propto b^{\lambda_a} \tag{1.35}$$

where the eigenvalue exponents λ_a are some function of the critical exponents. The rescaling factor b may then be seen to be effectively arbitrary since by iterating equation (1.30) l times one finds that the scaling fields evolve according to

$$\mu_a^{(l)}(b) = \Lambda_a^l(b)\mu_a = b^{l\lambda_a}\mu_a = (b_l)^{\lambda_a}\mu_a \tag{1.36}$$

with $b_l{=}b^l$. It follows from equation (1.36) that two points in coupling space are related by a *single* coarse-graining operation. Clearly therefore, the large-length-scale properties of all near-critical systems differ only in a matter of length-scales. This is, of course, just the assertion made on phenomenological grounds by the scaling hypothesis.

In general, there will be two relevant scaling fields μ_1 and μ_2, corresponding respectively to deviations of the temperature and reduced field from their critical values. Invoking specific results for the eigenvalue exponents λ_a (appendix A.2), the RG transformation properties of μ_1 and μ_2 can be written explicitly:-

$$\mu_1(b) = \Lambda_1(b)\mu_1 = a_1 b^{\lambda_1} t \;=\; a_1 b^{1/\nu} t \tag{1.37a}$$

$$\mu_2(b) = \Lambda_2(b)\mu_2 = a_2 b^{\lambda_2} h \;=\; a_2 b^{d-\beta/\nu} h \tag{1.37b}$$

where $h = h - h_c$ and a_1, a_2 are both system-specific parameters.

Clearly, the quantities $\mu_1(b)$ and $\mu_2(b)$ form a coordinate system which provides a *unique* measure of the location and direction of flow of the effective coupling in coupling space. However, as will become apparent in chapter 3, the form of the scaling fields given in equations (1.37a) and (1.37b), strictly only applies to a system whose Hamiltonian is symmetric with respect to positive and negative

values of the reduced ordering field. Although most magnetic systems satisfy this criterion, fluids do not.

Finally, it is possible to express the effective Hamiltonian $\mathcal{H}$ as a function of the scaling fields. Near the fixed point:

$$\mathcal{H} = \mathcal{H}^* + \sum_i \mu_i(b)\theta_i \tag{1.38}$$

where the variable θ_i are called scaling operators and are defined by equation (1.38). The scaling operators are the quantities conjugate to the scaling fields. For a simple magnetic system, θ_2 may be identified as the magnetisation (conjugate to the applied field) while θ_1 is the energy density (conjugate to the temperature).

1.9 Universality

The universality hypothesis constitutes one of the cornerstones of the contemporary theoretical view of critical phenomena and is its central unifying theme. It is founded upon the observation that, in the vicinity of a critical point, the thermodynamic properties of whole classes of physical systems exhibit a remarkably degree of insensitivity to the (possibly) quite distinctive nature of their microscopic interactions. As its basic tenet, the hypothesis holds that systems possessing the same set of 'symmetries' also possess an identical set of critical exponents and scaling functions. Such systems are said to belong to the same 'universality class'.

Those system symmetries that are known (thus far!) to delineate the universality classes are:-

- The spatial dimensionality of the system (d).
- The degree of isotropy of the order parameter (n).
- The range of the interactions.

- The rotational symmetry of the configurational energy.

A number of so-called 'standard models' are adopted as representative members of the most common universality classes. The nominated models are the simplest of their universality class and are classified according to the dimensionality of the order parameter (n). For $n = 1$ (scalar) models the standard model is the Ising model which was introduced in section 1.5 and is defined by equation (1.13). Models for which the order parameter is $n = 2$ (vector models) are typified by the X-Y model, defined by the equation

$$\mathcal{H} = -\sum_{<ij>} J(S_i^x S_j^x + S_i^y S_j^y) \tag{1.39}$$

The order parameter of the X-Y model is the vector sum of the spins in the x-y plane and the model is appropriate for describing easy-plane magnets. Isotropic magnetic systems (for which $n = 3$) are represented by the Heisenberg model. This model is defined by the equation

$$\mathcal{H} = -\sum_{<ij>} J(S_i^x S_j^x + S_i^y S_j^y + S_i^z S_j^z) \tag{1.40}$$

Lastly, there is the spherical model which assumes an infinite number of spin components $n = \infty$. This model seems to have no physical analogue, but it does have the advantage that it is exactly solvable.

The key theoretical elements underlying the notion of universality are to be found within the RG formalism. Under the RG transformation, *all* trajectories that start anywhere on the same critical surface, are borne towards the *same* fixed point and hence the same scale-invariant limit. Only gross differences in symmetries between systems are capable of altering the fixed point which controls critical behaviour. One fixed point (and hence one critical surface) can therefore be considered as generic to a whole class of models possessing the same symmetries. For systems of a given universality class, the convergence of the effective Hamiltonian to the fixed point may be expressed algebraically as follows:-

$$\lim_{b\to\infty} \Re_b \mathcal{H} = \mathcal{H}^* \tag{1.41}$$

where $\mathcal{H}$ denotes the specific microscopic Hamiltonian of a critical system before coarse-graining. Under repetition of the RG operation, the effective Hamiltonian contracts to the fixed point along the direction of the leading irrelevant eigenvector. Thus for b sufficiently large, different members of the same universality class are controlled by the same fixed point and hence the same eigenvectors and eigenvalues corresponding to perturbations away from criticality. It follows that all such systems share the same set of critical exponents and scaling functions.

Although the origin of universality can be traced to the controlling fixed point, it should be emphasised that the system need not be precisely at criticality for universal behaviour to be apparent. In fact, universality is to be expected *whenever* both b and ξ are large compared to the smallest length-scale. Provided this condition is satisfied, the system specific details (associated with transient flow towards the fixed point along the irrelevant eigenvector) will be erased. The location in coupling space of the effective Hamiltonian will then be uniquely described by the relevant scaling fields $\mu_1(b)$ and $\mu_2(b)$ and the effective Hamiltonian is said to reside on a 'universal manifold'. Thus provided their scaling fields are identical, different systems (which are member of a common universality class) will be described by the same effective Hamiltonian. In such circumstances it is to be expected that configurations of coarse-grained coordinates will be statistically indistinguishable.

1.9.1 Experimental Tests of Universality.

Experimental data abounds for most facetsof critical phenomena, especially for the values of critical exponents. Although it is not appropriate to review the relevant literature in great depth at this juncture, (though see references [11, 8, 12] for comprehensive reviews), some results will be cited to illustrate one instance of the validity of the universality hypothesis.

Three systems of general interest are: uniaxial ferromagnets, single component fluids and order-disorder structural phase transitions with short-range interactions. Each of these systems possesses the same symmetries as the 3-d Ising model and are accordingly all expected to belong to the 3-d Ising universality class. In the first category, measurements of the critical exponents of a uniaxial (anti)ferromagnet system have been made for FeF_2 by Belanger and Yoshizawa [13]. These workers employed neutron scattering techniques to determine the critical exponents controlling the correlation length and the susceptibility. They found $\nu = 0.64$ (0.632), $\beta = 0.325$ (0.326) and $\gamma = 1.25$ (1.25) where the numbers in parenthesis are the 3-d Ising-model values calculated from field theoretical methods.

Turning next to uniaxial fluids, highly accurate experiments have been performed by Hocken and Moldover [14] on xenon, sulphur hexafluoride and carbon monoxide. Experiments on critical fluids are technically difficult to perform for a number of reasons, principally because the divergent compressibility leads to gravity-induced density gradients in the sample. It is therefore only latterly that measurements have been possible of sufficient precision to verify the predictions of the universality hypothesis. The measured values of the principal exponents for SF_6 are $\nu = 0.623, \beta = 0.323, \gamma = 1.266$.

Few realisations of the 3-d Ising universality class are to be found among the ranks of order-disorder structural phase transitions. Most structural transitions are mediated by long-range dipolar interactions which bring them outwith the Ising class. For those Ising-like systems such as ND_4Cl that do exist, it is often rather difficult to attain the range of reduced temperature for which asymptotic scaling is valid. Nevertheless the order parameter exponent $\beta = 0.31$ has been measured for this material by Yelon *et al* [15], a result that is in reasonable accord with the 3-d Ising result.

It seems that at least in the case of the 3-d Ising universality class, there is substantial experimental evidence favouring the validity of the universality classification. In fact a similar body of evidence exists for other universality classes such as that typified by the 3-d Heisenberg model (see e.g. the work on EuS by Als-Nielson *et*

al [16]). Taken together, all the available evidence weighs heavily in favour of the general validity of the universality hypothesis.

1.10 Practical Methods for RG Calculations

1.10.1 Analytic Methods

Practical RG methods may be broadly categorised as based on either real-space or Fourier-space representations. The former category are used predominantly for lattice-based systems of low-dimensionality, while Fourier-space techniques are more useful for systems with continuous degrees of freedom (such as fluids) and for systems of high dimensionality. For a lattice system, one might implement a real-space RG calculation by first performing a spatial average over groups of neighbouring lattice variables. In contrast when employing Fourier-space methods, one describes the system in terms of plane waves of the ordering variable (the density in the case of a fluid). The coarse-graining then involves an integration over the shorter wave-length components. Of course the essential physics of the critical region must be independent of the particular coarse-graining method chosen to expose it. The choice of method is therefore merely one of calculational expediency.

The principal difficulty facing real-space RG calculations is the proliferation of coupling constants appearing in the effective Hamiltonian. Although the basic interaction range of the underlying lattice may only extend to nearest-neighbour spins, new and more exotic couplings are introduced at each step of a real-space RG scheme. These new couplings describe rather more complex interactions between the block variables, e.g. second and third neighbour interactions. The algebraic complexity associated with calculations of $\mathcal{H}'$ therefore increases at each iteration. To deal with this complexity a commonly adopted strategy is to make an approximation that eliminates all but a finite number of interactions. This truncation is usually justified on the grounds that the renormalised coupling con-

stants are fairly short ranged, so their effect can be ignored with relatively little error. The task therefore becomes one of determining which interactions can be reliably neglected, and estimating the error arising from their truncation. Once a good estimate for the fixed point couplings has been obtained, further analysis may yield information on the values of critical exponents. Most success in the area of analytic real-space RG has centred on exact blocking-schemes for finite lattices for which the range of couplings is limited by the size of the lattice. A few exact results also exist for infinite systems.

In practice many problems are often more amenable to assault by Fourier-space RG methods. Implementation of these techniques shows that all systems with short-ranged interactions, exhibit only very weak fluctuations in four dimensions (the upper critical dimension for Ising-like systems). At this dimensionality, such systems therefore exhibit essentially classical (mean-field) behaviour. From this observation it transpires that the critical exponents of systems with dimensionality $d < 4$ may be expressed perturbatively in terms of a power series in the (small) parameter $\epsilon = 4 - d$. These 'epsilon-expansions' yield surprisingly accurate values for the critical exponents in three dimensions, compared with experiment and computer simulation.

Notwithstanding the considerable successes of analytic RG calculations, it is the exception rather than the rule, that they yield quantitatively reliable estimates for critical exponents and amplitudes. There remain a great many systems that cannot be accurately investigated using current analytic techniques. This applies particularly to systems of lower spatial dimension for which real-space methods are often intractable and whose large-length-scale behaviour cannot be reliable characterised using the epsilon expansion. The task of investigating these systems therefore falls predominantly to computer simulation.

1.10.2 Computer Simulation Techniques

In those instances where a model has not yielded to analytic solution, it is common to appeal to computer simulation techniques. Computer simulation represents a powerful tool for studies of phase transitions and critical phenomena. In many respects a computer simulation resembles an experiment. No *a-priori* bias is incorporated in a simulation, one simply specifies the physical laws governing the interactions between the constituents of the system and allow the simulation to evolve as it will. In common with real experiments, simulations offer the possibility of new discoveries, whilst possessing the additional advantage that complete control is retained over all parameters of the model. For these reasons computer simulations plays an increasingly important role in the study of phase-transitions and critical phenomena.

Computer simulations methods have been successfully married with RG techniques to circumvent the problems associated with the proliferation of coupling constants generated by real-space RG transformations. A technique known as the Monte-Carlo Renormalisation Group method (MCRG) employs a computer to generate a sequence of configurations characteristic of the original Hamiltonian on a finite lattice. RG transformations can then be applied to each configuration to produce a sequence of block-spin configurations appropriate to the effective Hamiltonian. The method has the advantage that, unlike analytic real-space methods, there is no error involved in truncating interactions to form an approximate effective Hamiltonian. The configurations at each iteration are therefore distributed according to an effective Hamiltonian that derives exactly from its predecessor. Correlation functions may be calculated at each RG step and these provide information on effective couplings that can in turn be used to estimate critical exponents.

Notwithstanding its advantages over analytic techniques, the MCRG method is not completely error-free. Computers can only simulate a finite system and the effective Hamiltonian at each step is therefore necessarily only an approximation to that of the infinite system. This problem is not usually too serious provided

the effective range of the interactions in the effective Hamiltonian does not exceed the system size. Comparisons of data from systems of different sizes will indicate whether this is the case.

As alluded above, the most serious drawback of computer simulations of critical phenomena in general, is that their spatial extent is often small relative to the correlation lengths over which co-operative phenomena can occur. In these circumstances, a simulation can develop spurious artifacts and non-physical features, usually termed 'finite-size effects'. The most significant breakthrough in enabling the accurate study of the critical region by numerical simulation came with the development of finite-size scaling, a method which circumvents many of the difficulties associated with the study of criticality in finite systems.

1.11 Finite-Size Scaling

The theory of finite-size scaling was first proposed by Fisher [17]. It provides a framework for the inclusion of finite-size effects within the context of a scaling theory expressed in terms of the critical exponents of the corresponding *infinite* system. In essence, finite-size scaling invokes a scaling ansatz for the Helmholtz free energy, parameterised in terms of the system size and the correlation length ξ. For a hypercubic system of side L^d the Helmholtz free energy F may be written

$$F(h,t,L) \cong L^{(2-\alpha)/\nu}\mathcal{F}(ht^{-\beta\delta}, L^{1/\nu}t) \tag{1.42}$$

where $\mathcal{F}$ is a scaling function and in this context t$\equiv$ 1-T/T$_c(\infty)$ where T$_c(\infty)$ is the transition temperature in the thermodynamic limit. A derivation of equation (1.42) on the basis of renormalisation group methods can be found in Suzuki [18]. Corresponding finite-size scaling relations for the magnetisation, the magnetic susceptibility and the specific heat follow directly from equation (1.42).

Although finite-size scaling is very important in the context of films and sur-

faces, arguably its greatest utility lies in its relevance to computer simulations. As direct experimental confirmation of theoretical predictions often exceeds the capability of modern techniques, the task of verification may fall to computer simulation. Unfortunately, owing to the constraints of current computer technology, simulations often operate with model systems whose size is insufficient to provide reliable conclusions regarding the validity of theoretical predictions pertaining to the thermodynamic limit. Clearly then, a scaling theory that explicitly embodies finite-size effects is potentially of great service. A convenient realisation of finite-size scaling ideas appropriate for computer simulation, is to be found in the properties of the probability distribution function (PDF) of block coordinates.

1.11.1 Block Distribution Functions

An important result to emerge from finite-size scaling and renormalisation group methods, concerns the scaling and universal properties of block distribution functions. In real space, a block coordinate may be defined as the instantaneous value of the local ordering variable (assumed scalar) spatially averaged over a block of linear dimension L. The construction of block coordinates may be regarded as a form of coarse-graining operation. Denoting the block coordinate as u_L and the local ordering variable as u_i,

$$u_L \equiv \frac{\zeta_L}{L^d} \sum_i^{L^d} u_i \tag{1.43}$$

where ζ_L is the block variable scale factor to be prescribed below.

Formally, the probability of a measurement of u_L yielding a given value u'_L is defined by the equation

$$P_L(u'_L) = < \delta(u'_L - u_L) > \tag{1.44}$$

It will be found convenient for the purposes of analysis to use the integral representation of the δ-function to recast this relation in the form

$$P_L(u'_L) = \frac{1}{2\pi}\int_{-\infty}^{\infty} \hat{P}_L(Q)\exp(-iQu'_L)dQ \tag{1.45}$$

where

$$\hat{P}_L(Q) =< \exp(iQu_L) >, \tag{1.46}$$

is a characteristic function. From the properties of characteristic functions [19], $\hat{P}_L(Q)$ may itself be written as a M^{c}Claurin expansion in terms of the cumulants $J_L^{(n)}$ defined as the connected parts of the moments of $P_L(u'_L)$. The cumulant expansion takes the form

$$\hat{P}_L(Q) = \exp(\sum_{n=1}^{\infty} \frac{(iQ)^n}{n!} J_L^{(n)}), \tag{1.47}$$

and proves valuable for the analysis of the universal properties of the block PDF.

1.11.2 Universal Configurational Structure

In what follows a slightly modified version of a general argument due to Bruce [20] is presented, which serves to show that in the limit of large L and large ξ, the cumulants $J_L^{(n)}$ and hence the distribution $P_L(u_L)$ itself, assume limiting forms that are universal functions of the relevant scaling fields $\mu_1(L)$ and $\mu_2(L)$.

Consider first a set of scalar coordinates $u(x_i)$, associated with the N sites of a hypercubic lattice. The connected n-point correlation function at the reduced temperature t and reduced field h is

$$K^{(n)}(x_1...x_n; t; h) =< u(x_1)...u(x_n) >_c \tag{1.48}$$

where it is assumed that the average is evaluated in the canonical ensemble and the subscript c denotes connected part.

Suppose now, that the sites $x_1...x_n$ are separated by distances large compared to the lattice spacing. An RG operation may be performed on the partition function in the form of a partial trace over some fraction of the $\{u(x_i)\}$ sites. It is assumed that the $u(x_1)...u(x_n)$ are among the coordinates that survive this operation and which form a new lattice of spacing exceeding that of the original system by a factor $b \gg 1$. The RG operation is then completed by scaling the new lattice size back to that of the original lattice and rescaling the coordinates, according to

$$u(x_i) = a_0 b^{-\beta/\nu} u'(x/b) \tag{1.49}$$

where a_0 is a system specific constant. The following identity for the correlation functions may then be seen to hold

$$< u(x_1)...u(x_n) >_c = (a_0 b^{-\beta/\nu})^n < u'(x_1/b)...u'(x_n/b) >_c \tag{1.50}$$

where the average on the RHS of this equation is evaluated for the configurational energy of the effective Hamiltonian $\mathcal{H}'$. For b and ξ both large, the RG scaling hypothesis predicts that the location of $\mathcal{H}'$ on the universal manifold will be determined uniquely by the relevant scaling fields $\mu_1(b) = a_1 b^{1/\nu} t$ and $\mu_2(b) = a_2 b^{d-\beta/\nu} h$. Combining equations (1.48) and (1.50) thus shows that

$$K^{(n)}(x_1...x_n; t; h) = (a_0 b^{-\beta/\nu})^n \tilde{K}^{(n)}(x_1/b...x_n/b; \mu_1(b); \mu_2(b)) \tag{1.51}$$

where the functions $\tilde{K}^{(n)}$ are universal functions of $\mu_1(b)$ and $\mu_2(b)$.

Now, the cumulants appearing in the expansion of the characteristic function $\hat{P}_L(Q)$ of the block PDF are defined as

$$J_L^{(n)} = \zeta_L^n \sum_{\{x_1\}\in S(L)} ..... \sum_{\{x_n\}\in S(L)} K^{(n)}(x_1...x_n; t; h) \tag{1.52}$$

where S(L) is the set of all coordinates in the block. To the extent that the block-size L is large, the principal contributions to these cumulants derive from correlations between coordinates whose site separation is large. Accordingly the functions $K^{(n)}$ appearing in equation (1.52) may be approximated by their scaling forms. If further, one sets the arbitrary scale factor b equal to the block size L, then

$$J_L^{(n)} = [\zeta_L a_0 L^{-\beta/\nu}]^n \tilde{J}^{(n)}(\mu_1(L), \mu_2(L)) \tag{1.53}$$

where the *universal* functions $\tilde{J}^{(n)}(\mu_1(L), \mu_2(L))$ are defined as

$$\tilde{J}^{(n)}(\mu_1(L), \mu_2(L)) = \sum_{\{x_1\}\in S(L)} ..... \sum_{\{x_n\}\in S(L)} \tilde{K}^{(n)}(x_1...x_n; \mu_1(L), \mu_2(L)) \tag{1.54}$$

Finally, in order to guarantee the existence of a fixed point form of the block PDF it is necessary to specify the scaling factor ζ_L. Setting the variance of the fixed point block PDF $< u_L^2 >= J_L^{(2)} \equiv 1$ implies that

$$\zeta_L^{-1} = a_0 L^{-\beta/\nu} [\tilde{J}^{(2)}(0,0)]^{1/2} \tag{1.55}$$

It follows that provided both L and ξ are large compared to the lattice spacing, then the characteristic function $\tilde{P}_L(Q)$ and thus the block PDF itself are indeed universal functions of $\mu_1(L)$ and $\mu_2(L)$. A finite-size scaling ansatz for the block PDF, expressed in terms of the relevant scaling fields, can therefore be written [21]

$$P_L(u_L) = \zeta_L \tilde{P}(\zeta_L u_L, \mu_1(L), \mu_2(L)) \tag{1.56}$$

where $\tilde{P}$ is a universal function of the scaling fields $\mu_1(L) = a_1 L^{1/\nu} t$ and $\mu_2(L) = a_2 L^{d-\beta/\nu} h$. Here the block-variable scale factor $\zeta_L = a_0^{-1} L^{\beta/\nu}$ in the argument of $\tilde{P}$ serves to ensure the existence of a fixed point. The prefactor of ζ_L merely ensures that the block PDF remains normalised as the block variable scale is eroded.

In the special case when $\mu_2 = 0$, one finds that equation (1.56) simplifies to scale as a function of a *single* variable $z \equiv L/\xi$. Setting $\mu_2(L) = 0$ and making use of the relation $\xi \approx t^{-\nu}$, gives

$$P_L(u_L) = \zeta_L \tilde{P}(\zeta_L u_L, z^{1/\nu}) \tag{1.57}$$

The finite-size scaling properties of block coordinates expressed through equation (1.56), can be exploited by computer simulation to yield detailed information on critical scaling behaviour. This information is delivered in the form of whole scaling functions (principally $\tilde{P}$) which are expected to be common to members of the same universality class. By measuring the scaling behaviour of the block PDF (and its derivatives) for a number of different system sizes, one can also deduce values for the critical exponents (most significantly the exponent ratios $1/\nu$ and β/ν).

The great utility of the block PDF method for investigating critical phenomena, was first demonstrated by Binder [21] who performed monte-carlo simulations of the 2-d and 3-d Ising models. Binder's study elucidated the precise nature of the Ising fixed point block PDF (whose form had already been approximately derived using RG methods by Bruce [20]), and allowed him to accurately measure the critical exponents. The universality of the limiting form of the critical block PDF was also subsequently confirmed by Nicolaides and Bruce who carried out simulations on other members of the 2-d Ising universality class, most notably the 2-d ϕ^4 model [22].

The power of the block PDF method should be apparent, Indeed, for real-space problems, it may arguably be considered superior to the MCRG approach in

the sense that it provides a more direct route to scaling properties and critical exponents. In the MCRG method, configurations are generated merely as a means of calculating effective couplings from which scaling properties and exponents are then deduced. However, all the scaling information is implicit in the configurations themselves and can be extracted directly from the finite-size scaling behaviour of the block coordinates, thereby obviating the need to calculate effective couplings and avoiding the errors introduced therein.

To summarise the results of this section, it is found that in the regime where both L and ξ are large, the block distribution function exhibits universal behaviour as a function of the variables $\mu_1(L) = a_1 L^{1/\nu} t$ and $\mu_2(L) = a_2 L^{d-\beta/\nu} h$. The critical limit (for which $t, h = 0$) represents a special case of this general result. Precisely at criticality the scaling fields vanish and consequently the asymptotic form of the block PDF is invariant with respect to changes in the block size. Such scale invariance is an essential feature of the critical point: when viewed on all (sufficiently large) length-scales, configurational patterns appear statistically indistinguishable regardless of the microscopic parameters that characterise the 'bare' Hamiltonian. Of course this finding simply reflects the fact that at criticality, all configurations of coarse-grained variables are controlled by the fixed point Hamiltonian $\mathcal{H}^*$. However, because each universality class is associated with a distinct fixed point, the limiting fixed point form of the block PDF is expected to be unique to a universality class. It may therefore be usefully regarded as a hallmark or signature of a given universality class. [1]

1.12 Concluding Remarks

It has been seen that the RG method provides a formalism whereby the great complexity associated with the critical region can be simplified in a step-wise fashion. The method succeeds in placing the phenomena of scaling and universality on

[1] It should be noted that the universal form of the block PDF is dependent on the choice of boundary conditions applied to the block itself [21].

a firm footing and in some instances permits accurate calculations of the critical properties of model systems. Notwithstanding these successes, many model systems exist for which current RG techniques do not yield accurate predictions of critical point quantities. In consequence the RG has been unable to provide a thorough test of the universality hypothesis. In view of this, it is clearly important that universality be submitted to ever more stringent tests both by experiment and computer simulation.

The work described in the following two chapters details the application of the block PDF formalism described above, for investigations of universality in two scalar models. In chapter 2, the 1-d ϕ^4 model is studied with a view to resolving contention surrounding its supposed Ising-like behaviour. In chapter 3, simulations of the liquid-gas critical point are used to expose the physical basis of fluid-magnet universality and to elucidate the principal system-specific features of near-critical fluids.

Chapter 2

Universality in the One-Dimensional Continuous Spin Model

2.1 Introduction

A structural phase transition occurs when a material changes its crystallographic structure [12]. The prototype microscopic model for a structural phase-transition is known as the continuous spin (or ϕ^4) model. This model may be envisaged in terms of an assembly of particles (of unit mass) whose high temperature equilibrium positions define a hypercubic lattice. Each particle resides in a double-well potential $V_s(u)$ and is coupled to its immediate neighbours by harmonic forces. It is assumed that $V_s(u)$ has a uniaxial anisotropy, restricting particle movements to a single direction. Accordingly the position of each particle is described by a scalar displacement u_i, measured with respect to its lattice site. The single-particle potential itself, can be regarded as arising from a passive, incompressible, sublattice of atoms which do not actively participate in any phase transition. A one-dimensional realisation of the ϕ^4 system is depicted schematically in figure 2.1.

In the absence of an ordering field the configurational Hamiltonian of the ϕ^4 system takes the form

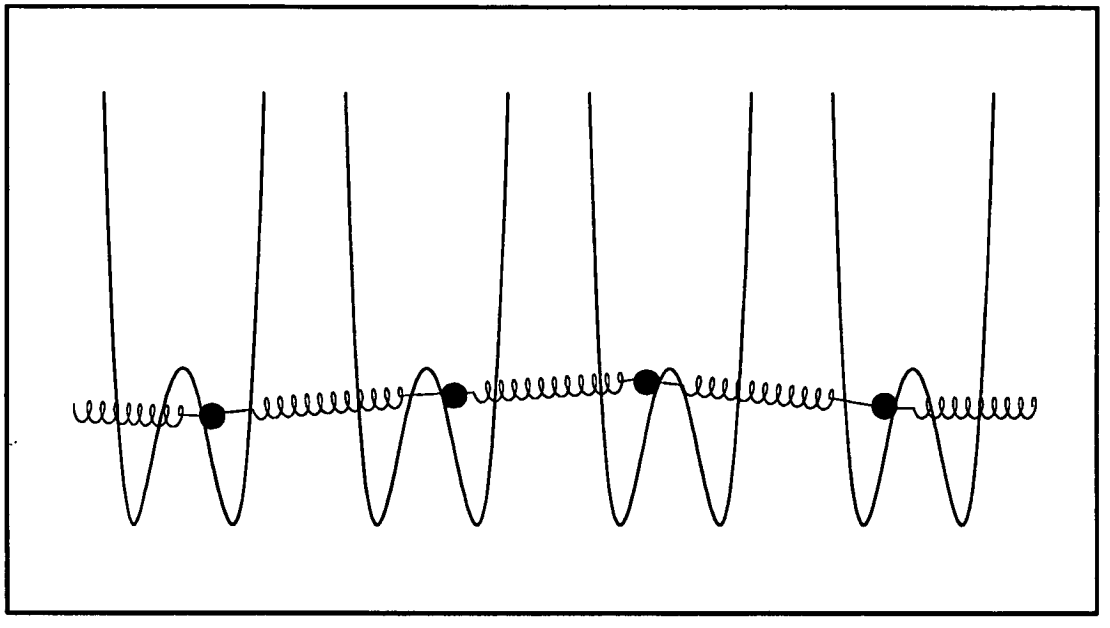

Figure 2.1: Schematic representation of the 1-d ϕ^4 model

$$\mathcal{H} = \frac{J}{2} \sum_{<ij>}^{n.n.} (u_i - u_j)^2 + \sum_i V_s(u_i) \tag{2.1}$$

with

$$V_s(u) = Au^2 + Bu^4; \qquad A < 0, B > 0 \tag{2.2}$$

Here the coupling constant J determines the strength of the coupling between nearest-neighbour (n.n) particles, while the parameters A and B serve to characterise the potential well.

For spatial dimensions $d \geq 2$ the ϕ^4 model exhibits a continuous phase transition. The order parameter for this transition corresponds simply to the net particle displacement $< u_i >$. That such a phase transition exists can be appreciated in a qualitative sense as follows. At zero temperature the energy (2.1) must be at a minimum. This corresponds to a fully ordered system with all particles residing in just one of the two degenerate ground states: $u_i = +u_o$ or $u_i = -u_o$, where

$\pm u_o = \pm(|A|/2B)^{\frac{1}{2}}$ locate the well-minima. In this state the energy per particle, ϵ_o, simply corresponds to the well-depth: $\epsilon_o = -A^2/4B$. As the temperature is raised, small 'islands' or clusters of the alternative low-temperature structure are formed within the otherwise ordered arrangement. These clusters are bounded by large-amplitude distortions or 'domain walls' which separate them from the majority phase. The spatial extent of the clusters may be regarded informally as some measure of the correlation length. Further increasing the temperature causes the clusters to grow in size until eventually, at some transition temperature, the proportion of particles associated with the clusters equals that associated with the original low temperature structure. At this point a continuous phase transition occurs to a state in which there is no net preponderance of one phase over the other. Close to the transition, response functions such as the susceptibility and the specific heat diverge. At and above the transition temperature, the order parameter $< u_i >$ vanishes and each particle is equally likely (on average) to be found in either of the well minima.

One system that exhibits an order-disorder phase transition similar to that described above is the ferroelectric material $NaNO_2$. At high temperatures, this substance has a disordered (para-electric) phase in which the N atom of the triangular NO_2 group lies with equal probability along the positive and negative directions of the b-axis of the unit cell. Below the phase transition, the N atoms assume a more ordered arrangement, being all aligned in the same sense along the b-axis. It should also be mentioned, however, that many structural phase transitions do not conform to the order-disorder model. Systems such as strontium titanate ($SrTiO_3$) exhibit a so-called 'displacive' phase transition. For this latter category of materials, the typical thermal energy of the particles participating in the phase transition is always large compared to the well depth and the phase-transition must be explained in terms of unstable phonon modes.

The one-dimensional realisation of the ϕ^4 model (which forms the focus of the present work) corresponds to a chain of particles. In common with all 1-d systems having short-range interactions, it cannot exhibit an order-disorder phase-transition at finite temperatures. This reflects the fact that in the thermodynamic

limit, the increase in the entropy-related part of the free energy, from the insertion of a domain wall into an ordered chain, is always less than the associated increase of internal energy [23]. The ordered arrangement is therefore unstable against domain wall formation for all $T > 0$ and hence no *stable* long-range order can be established.

Although the 1-d ϕ^4 model possesses no phase transition, it does exhibits two types of elementary excitations. In one dimension the nature of these excitations has been illuminated analytically [24, 25]. The principal excitations are solitary non-linear distortions (kinks) of a domain-wall nature, separating islands of the two favoured low temperature structures. These domain-wall excitations interact only weakly with one another and exhibit remarkable stability and other particle-like behaviour. At low temperatures, the correlation length is inversely related to the kink population density, which has a thermally activated form controlled by a kink energy of order the well-depth, so that $\ln \xi \sim \mid \epsilon_0 \mid /T$.

The second type of excitation are small-amplitude (harmonic) oscillations of the particles about the well-minima. These oscillations resemble phonons in character and have an associated coherence length $\xi_{ph} \sim (J/|A|)^{\frac{1}{2}}$ [24]. Much of the importance of the 1-d ϕ^4 model stems from the fact, that the basic features of its excitations (analytically tractable in one-dimension), persist to physically realistic higher dimensions for which a phase transition does take place. This in turn indicates that many of the interesting features of the ϕ^4 model are attributable to the double-welled character of the particle potential, rather than to the existence of a phase transition itself.

Notwithstanding the lack of a phase transition (and an associated non-trivial fixed point), the 1-d ϕ^4 model is still expected to exhibit universal behaviour with respect to its trivial fixed point at $T = 0$. The short-ranged character of the particle interactions and the scalar nature of the local ordering variable both suggest that the model should fall into the 1-d Ising universality class–the default for systems of these symmetries. To test this assertion, and in the light of a claim that universality fails for the 1-d ϕ^4 model [26], it seems worthwhile to conduct

an investigation into the large-length-scale properties of the model.

According to the arguments developed in the preceding chapter, the spectrum of coarse-grained configurations of a given system is expected to exhibit universal behaviour whenever the coarse-graining length and the correlation length are large compared to all microscopic lengths (the latter of which are represented principally in the present context by the phonon coherence length). From a practical standpoint, this universality may be exposed by obtaining the block distribution function. In the limit of large block size and in the absence of an ordering field, the block PDF assumes a form that is unique to a universality class and that scales as a single variable $z \equiv L/\xi$, the ratio of the block size to the correlation length. The issue of whether or not the 1-d ϕ^4 model actually falls into the Ising universality class may therefore be resolved from studies of the block PDF of both the 1-d ϕ^4 and the 1-d spin-$\frac{1}{2}$ Ising model. If the large-length-scale properties of the 1-d ϕ^4 model are indeed Ising-like in character, it is to be expected that there should exist a direct one-to-one mapping between the block PDFs of these systems for a given value of z. It is the purpose of the work described in this chapter to determine whether such a mapping can be effected.

2.2 The Transfer Matrix Method

One-dimensional systems lend themselves to a certain degree of analytic tractability. Indeed for the case of a 1-d assembly of N spins each having m discrete energy states it is possible to reduce the evaluation of the partition function to the calculation of the eigenvalues of a matrix–the so called transfer matrix [27]. To illustrate this method, consider the joint energy $E(x_i, x_{i+1})$ of a pair of neighbouring spins x_i and x_{i+1}. If it is assumed that the assembly has cyclic boundary conditions, then the partition function may be written

$$
\begin{aligned}
Z_N &= \sum_{x_i} \exp\{-\beta[E(x_1,x_2)+E(x_2,x_3)+....E(x_N,x_1)]\} \\
&= \sum_{i,j,...,l=1}^{m} V_{ij}V_{jk}...V_{li} \qquad (2.3)
\end{aligned}
$$

where the $V_{ij} = \exp(-\beta E_{ij})$ are elements of an $m \times m$ matrix $\mathbf{V}$, known as the transfer matrix.

It transpires that the sum over the matrix elements in equation (2.3) is simply just the trace of $\mathbf{V}^N$, given by the sum of its eigenvalues:-

$$Z_N = \lambda_1^N + \lambda_2^N + ...\lambda_m^N \qquad (2.4)$$

For very large N, this expression simplifies further because the largest eigenvalue λ_1 dominates the behaviour since $(\lambda_2/\lambda_1)^N$ vanishes as $N \rightarrow \infty$. Consequently in the thermodynamic limit one may put $Z_N = \lambda_1^N$ and the problem reduces to identifying the largest eigenvalue of the transfer matrix.

2.3 The Block PDF of the 1-d Periodic Ising Chain

In this section transfer matrix methods are employed to obtain an analytic expression for the block PDF of the 1-d Ising model. The form of the block PDF depends on the choice of boundary conditions both for the block and for the system itself [21]. The system considered in this work was a linear chain Ising model of fixed length N having cyclic boundary conditions. For simplicity the block size L was chosen to coincide with the system size so that $L = N$. With this choice, the boundary conditions on the block are simply those which apply to the system as a whole. Other types of boundary conditions have been considered by other authors e.g. Bruce, who calculated the distribution function for the case when the block is a sub-unit of the total system [20].

In the absence of an ordering field, the configurational energy of the 1-d Ising model takes the form

$$\mathcal{H}_o = -K \sum_{i=1}^{N} \sigma(x_j)\sigma(x_{j+1}); \qquad K = J/kT \tag{2.5}$$

The total magnetisation variable σ_N for the chain is then simply

$$\sigma_N = \frac{1}{N} \sum_{j=1}^{N} \sigma(x_j) \tag{2.6}$$

where the index j runs over the N sites of the chain and $\sigma(x_j)$ takes the values ± 1. The equilibrium probability distribution of this variable may then be written formally as

$$P_N(\sigma_N) \equiv < \delta(\sigma_N - \frac{1}{N} \sum_{j}^{N} \sigma(x_j)) > \tag{2.7}$$

It is useful to focus on the Fourier transform of the distribution function

$$P_N(\sigma_N) = \frac{1}{2\pi} \int_{-\infty}^{\infty} \hat{P}_N(Q) e^{-iQ\sigma_N} dQ \tag{2.8}$$

where

$$\hat{P}_N(Q) = < \exp iQ\sigma_N > = \frac{Z(Q/N)}{Z(0)} \tag{2.9}$$

and $Z(h)$ is defined by the configuration sum

$$Z(h) = \sum_{\{\sigma\}} e^{-\mathcal{H}_o + ih \sum_j \sigma(x_j)} \tag{2.10}$$

Expressed in this form, the task of determining $P_N(\sigma_N)$ is simply one of calculating the Fourier transform of the partition function of the Ising model. This task can be accomplished analytically by employing the transfer matrix method.

The appropriate transfer matrix is that of the spin-$\frac{1}{2}$ Ising model in the presence of an applied field.

$$F(h) = \begin{pmatrix} e^{ih+K} & e^{-K} \\ e^{-K} & e^{-ih+K} \end{pmatrix} \tag{2.11}$$

This matrix has two eigenvalues which can be readily calculated in the usual fashion. They are

$$\lambda_{\pm} = e^{K}\cosh(1 \pm \alpha(h)) \tag{2.12}$$

where

$$\alpha(h) = \left(1 - \frac{2\sinh 2k}{e^{2K}\cos^2 h}\right)^{1/2} \tag{2.13}$$

The transform of the block PDF then follows as

$$\hat{P}_N(Q) = \frac{Z(Q/N)}{Z(0)} = \frac{\sum_{\gamma=1,2}[\lambda_\gamma(Q/N)]^N}{\sum_{\gamma=1,2}[\lambda_\gamma(0)]^N} \tag{2.14}$$

Substituting in the form of the eigenvalues $\lambda_{\pm}$ yields

$$\hat{P}_N(Q) = \frac{e^{NK}\cos^N(\frac{Q}{N})}{2^N(\cosh^N K + \sinh^N K)}\left[(1+\alpha(\frac{Q}{N}))^N + (1-\alpha(\frac{Q}{N}))^N\right] \tag{2.15}$$

In the universal regime of large N and low temperature (for which ξ is large on the scale of the lattice spacing $a = x_{i+1} - x_i$) this expression for $\hat{P}_N$ simplifies considerably. To facilitate the simplification, consider first the behaviour of the pair correlation function $\Gamma(r_{ij})$ for the Ising model. It can be shown [1] that

$$\Gamma(r_{ij}) = [\tanh K]^{r_{ij}} = \exp[(\ln\tanh K)r_{ij}] \tag{2.16}$$

where $r_{ij} = |x_j - x_i|/a$. For low temperatures (large K), $\tanh K \simeq 1 - 2e^{-2K}$ so that the correlation length (in units of the lattice spacing a) is

$$\xi = -1/\ln\tanh K \simeq e^{2K}/2 \tag{2.17}$$

Also in the same limit, one finds $(1-e^{-2K})^N \equiv (1+z/2N)^N \simeq e^{z/2}$, where $z = N/\xi$. Feeding these results back into equation (2.15) then yields

$$\hat{P}_N(Q) \simeq \frac{1}{2\cosh(z/2)}\left\{\left[\cos(Q/N) + [\cos^2(Q/N) - 1 + e^{-4K}]^{1/2}\right]^N + \left[\cos(Q/N) - [\cos^2(Q/N) - 1 + e^{-4K}]^{1/2}\right]^N\right\} \tag{2.18}$$

To the extent that the ratio Q/N is small, the cosines can be expanded to first order as a power series giving

$$\hat{P}_N(Q) \simeq \frac{\cosh(\frac{z^2}{4} - Q^2)^{1/2}}{\cosh(z/2)} \tag{2.19}$$

This final expression for $\hat{P}_N(Q)$, valid in the large N, low temperature regime may be Fourier transformed analytically. Employing results tabulated by Oberhettinger, one finds [28]

$$P_N(\sigma_N) = \frac{1}{2\cosh(z/2)} \left[\frac{zI_1(\frac{z}{2}(1-\sigma_N^2)^{1/2})}{2(1-\sigma_N^2)^{1/2}} \Theta(1-\sigma_N^2) + \delta(1-\sigma_N) + \delta(1+\sigma_N) \right] \tag{2.20}$$

where I_1 is a modified Bessel's function and $|\sigma_N| \leq 1$.

Equation (2.20) is the principal result of this section. It constitutes an explicit finite-size scaling expression for the one-dimensional spin-$\frac{1}{2}$ Ising model for the particular case when the block-size coincides with the chain-length N and *periodic* boundary condition are imposed on the chain. The expression is valid in the limit of large block-size N, and low temperature (so that ξ is large). It depends solely on the ratio of the chain length to the correlation length.

It transpires, that the PDF (2.20) has a whole spectrum of states bounded by two extremes which merit specific attention. Firstly the temperature may be so low that the average thermal energy per particle is small on the scale of the well-depth. The particles are then localised in the vicinity of the well minima. As the temperature approaches zero for fixed N, the correlation length grows systematically larger on the scale of the block-length. Very few domain-walls will be found within a block and the probability distribution of the block magnetisation variable therefore assumes a sharply peaked form whose maxima lie close to the fully ordered states $\sigma_N = \pm 1$. It follows that in the limit as T vanishes for fixed N (i.e. $z \rightarrow 0$), the magnetisation distribution can be expressed by a pair of delta functions. This is consistent with equation (2.20) given that the first term

vanishes as $z \to 0$.

Alternatively the temperature may be fixed at some finite value but the block-size is permitted to become very large on the scale of the correlation length so that $z \to \infty$. Simple fluctuation theory then dictates that in this limit the magnetisation distribution will be a gaussian centred on $\sigma_N = 0$. That this is also consistent with equation (2.20) may be readily verified directly from equation (2.19)

$$\lim_{z\to\infty} \hat{P}_N(Q) \simeq \exp(\frac{z}{2}[1 - 2Q^2/z^2 + ...])/\exp(z/2) = \exp(-Q^2/z), \qquad (2.21)$$

which implies that the magnetisation distribution $P_N(\sigma_N)$ is itself also a gaussian. This result (which may be regarded as an expression of the central limit theorem) is reflected in the asymptotic gaussian form of the modified Bessel function in the limit of large z.

Intermediate between the two limits $z \to 0$ and $z \to \infty$, the distribution function is non-trivial in character. In particular, the first term in (2.20) will not, in general, be gaussian and the delta-functions will contain finite weight. Figure 2.2(a) shows the behaviour of the distribution function calculated for a representative selection of values of z. The singular structure at $\sigma_N = \pm 1$ has been suppressed in the figure, but its weight is implied by the constraint that the overall integrated weight is normalised to unity. From the figure it is evident that the distribution evolves smoothly between the limiting behaviour described above.

Finally, it is instructive to compare the block PDF of the periodic Ising chain (2.20) to that of the sub-block expression derived by Bruce [20]. Differences between the two expressions can be traced to the fact that the periodic chain can only support an even number of kinks. Figure 2.2(b) shows examples of the sub-block PDF for distributions having the same values of z as those in figure 2.2(a). Comparison of the two figures shows that for large z, the distributions are essentially identical, but that they differ significantly for small z. This observation reflects what one might expect intuitively, namely that the influence of the boundary conditions on the large-length-scale behaviour depends on the magnitude of the correlation

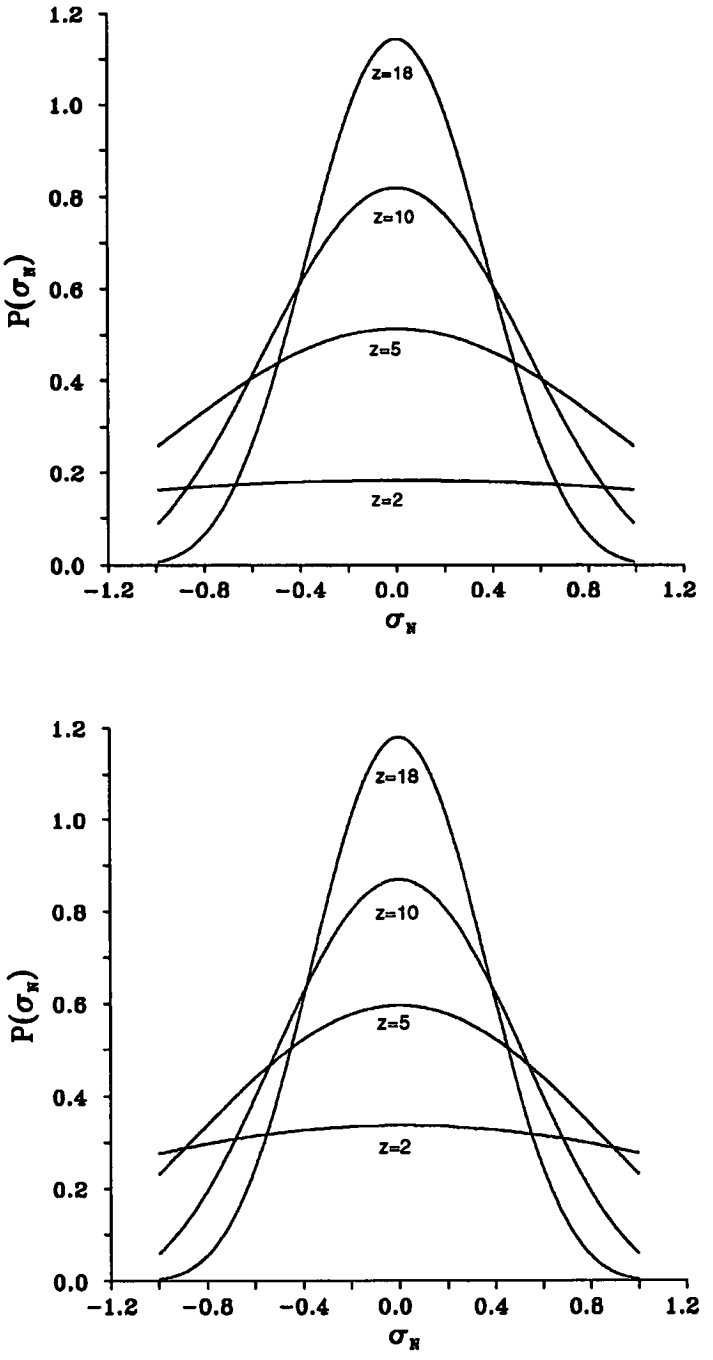

Figure 2.2: The limiting one-dimensional form of the Ising block PDF for selected values of z. (a) Periodic-block boundary conditions. (b) Sub-block boundary conditions.

length *relative* to the system size. If the correlation length is small compared to the system size, then the block PDF will be relatively insensitive to the boundary conditions. Conversely, if the correlation length is comparable with the system size then the boundary conditions *will* have a major influence on the block PDF. Specifically, particles in the periodic system will tend to form an ordered arrangement more easily than those in sub-blocks. Consequently for a given value of z (assumed small), greater weight is associated with the (implied) delta-function peaks of the periodic system than with those of the sub-block system.

2.4 The Block PDF of the 1-d ϕ^4 Model

As its name implies, the continuous spin model does not possess a finite set of single particle energy states. In consequence, the partition function cannot be expressed in terms of a transfer matrix of finite dimension and must instead be treated by transfer *operator* methods. Unfortunately, such methods do not furnish an exact expression for the distribution of the block coordinate $\sigma_N = L^{-1}\sum_i u_i$ of the 1-d ϕ^4 model. Nevertheless, they do indicate that the large-length-scale behaviour is dominated by the two largest eigenvalues of the transfer operator [29]. This finding itself implies that the block PDF of the 1-d ϕ^4 model should coincide asymptotically with that of the spin-$\frac{1}{2}$ Ising model [20]. Notwithstanding this proposition, direct confirmation of the universality of the 1-d ϕ^4 model has hitherto, been lacking.

One route via which the block distribution function *can* be accessed directly is the method of computer simulation. This section describes a computer study undertaken to calculate the block PDF of the 1-d ϕ^4 model.

The simulated systems comprised a periodic chain of N particles. The block size was chosen to equal the system size so that L=N, thus facilitating contact with the expression for the block PDF of the Ising chain (2.20) having the same boundary conditions. Systems having N= 128 and N= 256 particles were studied for a

number of couplings. Particle configurations were generated using a Metropolis Monte-Carlo algorithm. The form of this algorithm adapted to deal with continuous variables, is that of Bruce [30]. General aspects of Monte Carlo methods for the simulation of statistical systems are described by Binder and Heermann [31].

The program was implemented in parallel on the AMT Distributed Array Processors (DAPs) at the Edinburgh Parallel Computing Centre. The DAP computer consists of an array of 4096 linked but independent processors which execute instructions on their data concurrently. The processor links can be configured in software to form either a square grid of processors or alternatively (and as adopted in the present study), a one dimensional processor-chain. Many computational problems (especially lattice-based spin/particle systems) possess a high degree of inherent parallelism and so benefit enormously from implementation on a machine of parallel architecture. A common strategy is to assign each spin or particle to the control of one processor. The links between nearest neighbour processors then provide for the calculation of particle interactions. In this way, many particles can be updated simultaneously, subject to the condition they do not interact. Parallelism, when exploited to the full, can therefore greatly enhance the speed and efficiency of computer simulations. As a result, larger systems can be studied and superior statistics can be accumulated. Further details of the DAP architecture and parallel mapping strategy are described in appendix B.1 and reference [32].

In the present work, each particle was placed under the control of one processor. The characteristics of the processor array then favour systems sizes of the form $N = 2^n$ with $N = 4096$ as the upper limit. As the number of available processors greatly exceeds the number of particles in each of the systems studied, it was possible to simulate a number of independent systems simultaneously, thus enhancing considerably the rate of data acquisition. The simulations were all performed at the so-called 'border' point in the ϕ^4 parameter space (A$= -J$) since this point lies intermediate between the displacive and order-disorder regimes of the ϕ^4 model. So defined, only one free variable is required with which to tune the correlation length, namely the nearest neighbour (reduced) coupling K$= J/K_BT$. For the N=128 system simulations were performed at reduced couplings of K$=$ 0.75 and

K= 0.95 while for the larger system N= 256, couplings of K= 0.95 and K= 1.071 were employed

Prior to data collection, it was necessary to thoroughly equilibrate each system at the designated coupling. To this end, a number of preliminary monte-carlo sweeps of the system were performed. This equilibration procedure ensures that the generated configurations are independent of the initial configuration and thus truly representative of thermodynamic equilibrium. For the lower couplings, equilibration runs comprised 10^6 monte-carlo sweeps of the system. At the highest coupling $K = 1.071$, (for which equilibration problems were more acute), the equilibration period was extended to 2×10^6 monte-carlo sweeps. Once equilibrated, approximately 5×10^4 observations of the block variable $\sigma_N = N^{-1} \sum_i u_i$ were collected, each separated by 200 intermediate monte carlo sweeps to reduce correlations between the observed values. The observations of σ_N were accumulated to form a histogram of $P_N(\sigma_N)$ in accordance with its definition (equation 2.7).

To facilitate the mapping of the simulation data onto the Ising expression (equation 2.20), it was necessary to establish (for a given coupling constant), the value of the correlation length ξ and hence the factor $z \equiv N/\xi$. The appropriate value of ξ is, of course, that pertaining to the infinite length system, since it is this quantity that is used in the derivation of equation (2.17). Values of ξ were measured from the correlation function (out to a distance of 64 neighbours) at couplings of $K = 0.75$ and $K = 0.95$ in a simulation of $N = 16384$. This method yielded values of $\xi = 5.14$ and $\xi = 22.34$ respectively.

One disadvantage imposed by the DAP architecture is that system sizes must preferably take the form N= 2^n. This constraint causes some difficulty if one wishes to investigate scaling behaviour by studying different system sizes at the *same* value of z. For the chosen systems sizes, N= 128 and N= 256, it was necessary to search for two couplings whose associated correlation lengths were also related by a factor of two. A coupling of K=1.071 was found to yield the correlation length $\xi = 44.67$, almost exactly twice that of $\xi = 22.34$ obtained with a coupling of $K = 0.95$.

By way of a consistency check on the measured values of the correlation length, ξ was also measured independently from the 'kink' or domain wall population of the chain. In the low temperature limit it is to be expected that kinks are distributed according to a Poisson distribution. It can then be readily shown that the correlation length (in units of the lattice spacing) is

$$\xi = \frac{1}{2p} \tag{2.22}$$

where p is the probability of finding a kink per unit length. In order to exploit this relation to measure the correlation length, some computational criterion for defining a kink was necessary. The chosen criterion required that the difference in the displacements of two neighbouring particles $u_{n+1} - u_n$ should exceed the absolute displacement $|u_{n+1}|$, $|u_n|$ of both particles.

Measurements of the kink population were performed for a system of $N = 16384$ particles at couplings of $K = 0.95$ and $K = 0.75$. For the former coupling, this procedure yielded $\xi = 22.29$ in good agreement with the value obtained from correlation functions. At lower couplings the measured correlation length was $\xi = 4.96$, in less satisfactory agreement. The discrepancy in this latter measurement is probably attributable, in part at least, to the breakdown at higher temperatures of the validity of the poissonian distribution as a description of the kink number density distribution. Moreover at higher temperatures, where the particles are not localised at the well minima, the whole concept of what constitutes a kink becomes less well-founded. From a computational standpoint therefore it seems that although kink density measurements provide a reasonable measure of the correlation length at low temperatures, the method is no substitute for the calculation of ξ from correlation functions. In the results that follow the stated values of ξ derive solely from correlation function.

Figures 2.3 and 2.4 present the measured ϕ^4 block distribution function (data points) for two different values of z. In both cases, the expression (2.20) for the limiting form of the block PDF of the Ising model is also shown (smooth curve). The data in figure 2.3 corresponds to a value of $z = 128/5.14 = 24.90$, obtained for

a coupling $K = 0.75$. The permitted tuning of the block variable scale σ_N has been applied to bring the variance of the ϕ^4 distribution function into coincidence with that of the Ising coarse-grained variable (c.f. chapter 1). Clearly for this value of z, the system is in the displacive regime, as evidenced by the near-gaussian nature of the distribution function. Although the correlation length $\xi = 5.14$ is not particularly large, the accord between the scaled distribution of the ϕ^4 model and the Ising curve is striking.

Figure 2.4 provides substantially more compelling evidence of the essentially Ising-like nature of the 1-d ϕ^4 model. The results in this figure correspond to a value of $z = 5.73$. Unlike the approximately gaussian function depicted in figure 2.3, the form of the distribution in figure 2.4 is non-trivial. It therefore represents a considerably more exacting test of universality. The data shown was obtained from studies of two *different* system sizes. The first system, consisting of N= 128 particles was simulated for a coupling of $K = 0.95$, while the second—twice the length of the first, was studied for a coupling of $K = 1.071$. As detailed previously, the stated couplings serve to maintain the same value of z for both system sizes. In both instances the block variable of the simulation data has been scaled to equate the variance of the distributions with that of the Ising curve.

Except in the vicinity of $\sigma_N = 1$, the simulation results collapse onto one another and onto the Ising curve. In the vicinity of $\sigma_N = 1$ the simulations show near-gaussian peaks narrowing with increasing systems size, thus realising asymptotically the δ-functions in equation (2.20). This smearing-out of the delta functions into near-gaussian peaks is a non-universal feature of the 1-d ϕ^4 model and represents the leading corrections to the asymptotic form of the block PDF. To understand more fully the nature of these corrections, it is necessary to incorporate the effect of small spatial fluctuations of the particles within the particle well. This matter forms the subject of the following subsection.

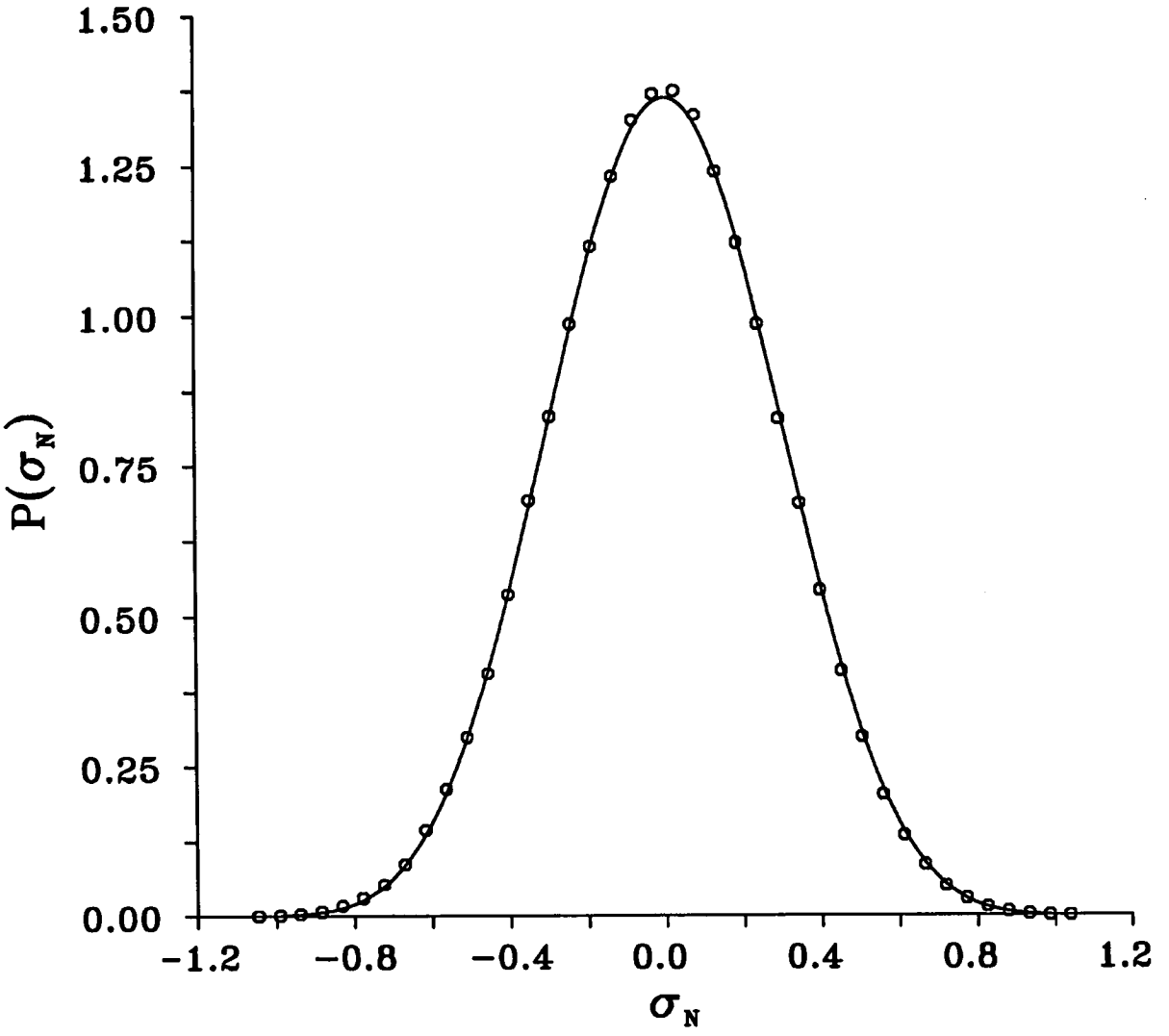

Figure 2.3: Estimates for the probability distribution $P_N(\sigma_N)$ of the coarse-grained variable of the 1-d ϕ^4 model with $z \equiv N/\xi = 24.90$. The statistical uncertainties do not exceed the symbol sizes. The exact expression (equation 2.20), which is valid in the large N, ξ regime is represented by the full curve

EX BIBL UNIV. EDI

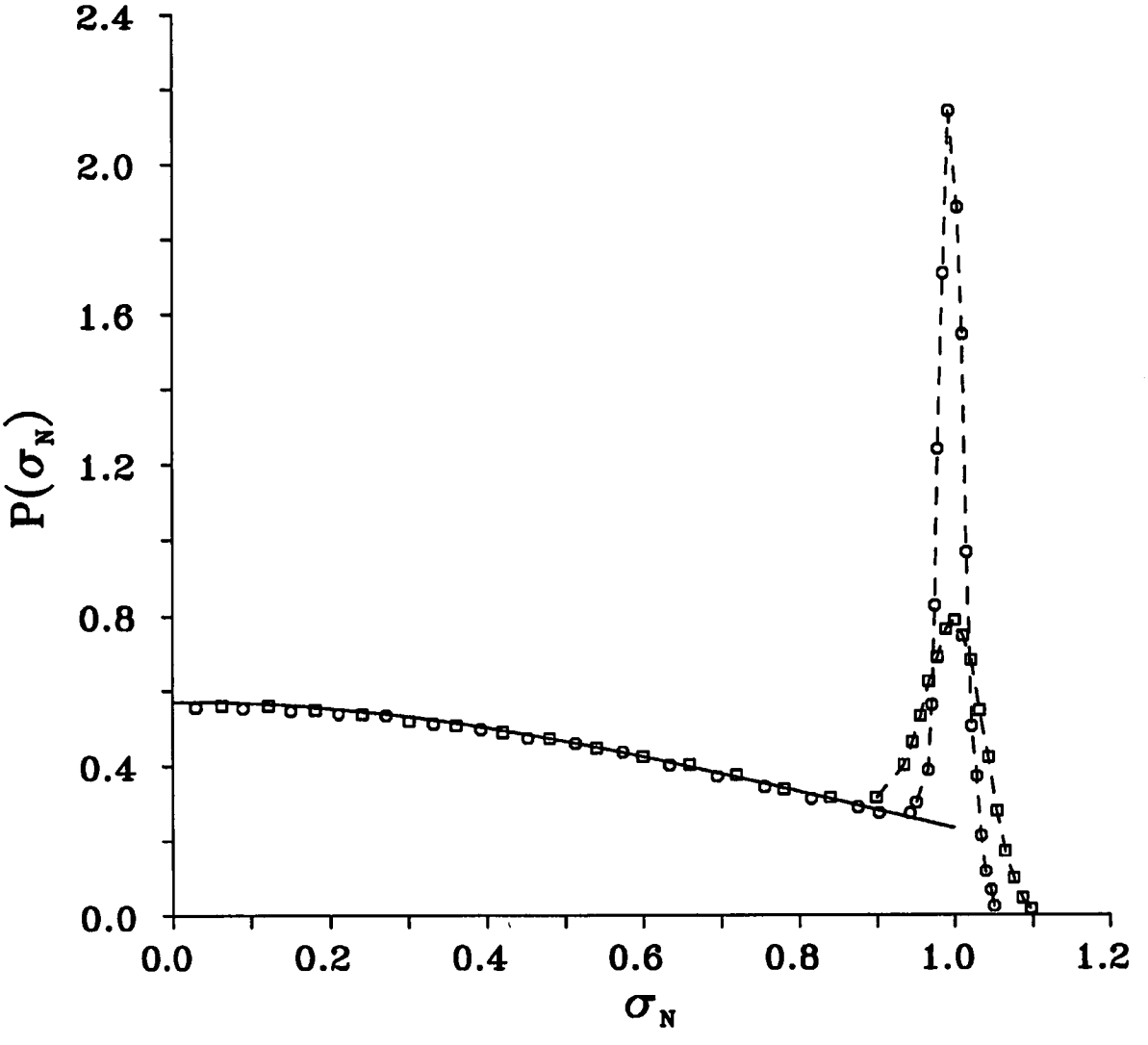

Figure 2.4: Estimates for the probability distribution $P_N(\sigma_N)$ of the coarse-grained variable of the 1-d ϕ^4 model with $z \equiv N/\xi = 5.73$. Two cases are shown: N=128, $\xi = 22.34(\square)$ and N=256, $\xi = 44.67$(o). The statistical uncertainties do not exceed the symbol sizes. The exact expression (equation 2.20), which is valid in the large N, ξ regime is represented by the full curve, with the singular structure at $\sigma_N = 1$ suppressed. The broken lines through the near-Gaussian peaks serve merely to guide the eye.

2.4.1 Leading Corrections to the Asymptotic Form

In one dimension, the leading corrections to the asymptotic Ising form (2.20) are non-universal, reflecting specific microscopic properties of the given system. In the case of the ϕ^4 model, the corrections are attributable to small amplitude oscillations of the particles within the single-particle well—phonons. These oscillations disturb the otherwise ordered character of the clusters and for finite block-size this is reflected by a smearing-out of the singular structure near $\sigma_N = \pm 1$ into the near-gaussian peaks seen in fig 2.4.

To determine in a rigorous fashion the leading corrections to the block PDF requires the evaluation of the two next-largest eigenvalues of the transfer operator for the 1-d ϕ^4 model. No exact expressions exist for these eigenvalues. However, an approximate perturbative calculation can be performed, based on the following simple phenomenological argument [20, 25].

At low temperatures the particle displacement u_i can be decomposed into an Ising-like variable $\pm\sigma_0 = \pm u_0$ and a small-amplitude harmonic fluctuation g(x).

$$u(x) = \sigma(x) + g(x) \tag{2.23}$$

The harmonic fluctuations $g(x)$ have RMS amplitude g_0 and a correlation length ξ_{ph}. Except in the vicinity of a kink (whose number density is assumed small), correlations between the $g(x)$ coordinates and the σ variables can be assumed negligible. The dominant correction to the moments of the block PDF can therefore be assumed to arise from correlations between the $g(x)$ variables themselves. If further, one retains only two-body correlations between the $g(x)$ coordinates (assuming higher order correlations to be small in comparison), the leading correction involves only the second moment of the block PDF. Accordingly, one can write

$$M_L^{(2)} = M^{(2)\infty} + \Delta M_L^{(2)} \tag{2.24}$$

where

$$\Delta M_L^{(2)} = L^{-2} \sum_{x_1=1}^{L} \sum_{x_2=1}^{L} < g(x_1)g(x_2) > \tag{2.25}$$

represents the leading correction to the second moment of the block PDF and

$$< g(x_1)g(x_2) >= g_o^2 \exp(-|x_2 - x_1|/\xi_{ph}) \tag{2.26}$$

It may then be readily shown that

$$\Delta M_L^{(2)} \approx \frac{2g_0^2\xi_{ph}}{\sigma_0^2 L} \tag{2.27}$$

Finally, recalling the definition 1.47 of the block PDF in terms of its cumulant expansion, and noting that $J_L^{(2)} = M_L^{(2)}$, one immediately finds

$$\hat{P}_L(Q) = \hat{P}_L^{\infty}(Q)\hat{P}_{ph}(Q) \tag{2.28}$$

where

$$\hat{P}_{ph}(Q) = \exp(-Q^2 g_0^2 \xi_{ph}/\sigma_0^2 L) \tag{2.29}$$

In other words, the measured block PDF comprises a *convolution* of the limiting Ising function with the non-universal (gaussian) correction function deriving from phonon oscillations. With this perspective it is easier to understand the discrepancies, apparent in figure 2.4, between the measured PDF and its limiting form. The deviations are most pronounced in the vicinity of $\sigma_N = \pm 1$ simply because the limiting function (2.20) is singular at this point. Indeed, due to the action of the δ-functions, the near-gaussian peaks in the measured distribution represent precisely the non-universal component of the block PDF whose Fourier transform features in equation (2.29). Away from $\sigma_N = \pm 1$, the limiting function is relatively smooth and flat; the convolution with the phonon-based correction therefore yields negligible discrepancy in this region.

2.5 Pluralism in the 1-d ϕ^4 model?

Claims (alluded to in the introduction) that universality fails in the 1-d ϕ^4 model, have centred around a transfer-matrix analysis performed by Baker [26]. In his analysis, Baker finds a temperature dependence for the correlation length that differs radically from that of the 1-d Ising model, thus leading him to conclude in favour of pluralism (the antithesis of universality) in the 1-d ϕ^4 model. The source of this apparent failure of universality can, however, be traced to Baker choice of a physically unreasonable temperature dependence for the model parameters A and B featuring in equation (2.2).

The essential features of Baker's argument are as follows. Suppose, that the potential parameters A and B are chosen to be temperature–*dependent*, such that $\mathrm{A}= -\mathrm{J}+\mathrm{kT}\tilde{\mathrm{A}}$ and $\mathrm{B}=\tilde{\mathrm{g}}_o\mathrm{kT}$, with $\tilde{\mathrm{g}}_o$ and $\tilde{\mathrm{A}}$ constants. The 'ground state' energy (minimum energy at a given T) will then also be temperature-dependent: $\epsilon_o \sim -1/\mathrm{T}$. Now, as recorded in the introduction, the correlation length has a thermally activated form that behaves as $\ln\xi \sim \mid \epsilon_o \mid /\mathrm{T}$. Thus for Baker's form of the potential parameters, the correlation length will grow as $\ln\xi \sim 1/T^2$. This result is indeed, radically different from that of the standard one-dimensional Ising model for which $\ln\xi \sim 1/\mathrm{T}$ (c.f. equation 2.17). However, its peculiar nature reflects the physically artificial temperature-dependence of Baker's choice for the model potential. The choice is unreasonable because it implies 'critical' behaviour in the temperature dependence of the ground-state energy which diverges as $T \rightarrow 0$.

The 'failure' of universality identified by Baker is thus of a trivial kind, which is always possible to engineer if one so wishes. It has no bearing on the validity of the hypothesis in the context of physically *realistic* models. Moreover, and notwithstanding manually-inserted temperature-dependent pathologies, key elements of the universality phenomenon can always be exposed by parameterising the problem in terms of length-scales. Thus whenever the correlation length is asymptotically large on microscopic length-scales, coarse-grained configurational patterns will be universal and statistically self-similar. This point is graphically

illustrated for the 1-d ϕ^4 model in figure 2.4.

2.6 Concluding Remarks

Evidently the results of figures 2.3 and 2.4 bear out the universality of the scaling function (2.20) and the picture it expresses: the large-length-scale configurational patterns of the 1-d ϕ^4 model match quantitatively those of the 1-d Ising model. That such a mapping exists is a consequence of RG-based scaling theory and represents perhaps the single most exacting test of the universality hypothesis. The results therefore lend very strong support to the contention that the one-dimensional ϕ^4 model does indeed belong to the Ising universality class.

The limiting universal form of the block PDF for 1-d Ising systems also provides insight into the nature of the typical ordering configurations in this class of models. As $\xi \to \infty$, for large but finite block-size, the order is seen to reside entirely in clusters, whose typical size is characteristic of the correlation length. These clusters are local regions of perfect homogeneous order, separated from their neighbours (whose order is necessarily of the opposite sense) by spatially-localised cluster-walls or kinks. As these kinks represent the only disturbance to the order of the system, it is possible to formulate the limiting properties of 1-d systems purely in terms of the statistical mechanics of the kink population [25].

From the results presented in this chapter, it should be apparent that the block distribution method provides a simple, yet powerful technique for investigating universality in scalar models. As will become apparent in the following chapter, the method finds even greater utility in higher dimensions where it can be employed to locate critical points with high accuracy and to probe subtle theoretical predictions whose direct experimental verification has proved problematic.

Chapter 3

Critical behaviour in the Two-Dimensional Lennard-Jones Fluid

> Plus ça change, plus c'est la même chose.
> —Alphonse Karr

3.1 Preamble

In the field of critical phenomena, the major advances over the last two decades have been in the context of magnetic systems. Experimental studies of near-critical magnets have yielded a vast body of data on quantities such as critical indices and correlation functions [8]. Considerable theoretical progress has also been made through Renormalisation Group studies of lattice-based spin models such as the Ising and Heisenberg models and continuum models such as the Landau-Ginsburg-Wilson model. Both the experimental and theoretical work have been supported and complemented by extensive computer simulations, providing new insight into the microscopic nature of cooperative phenomena in critical magnets.

By contrast, the continuous phase transition associated with the liquid-vapour critical point remains relatively poorly characterised compared to its magnetic counterpart. The evidence that has emerged from experimental and theoretical

investigations of the universality class of the transition is rather circumstantial and somewhat less than satisfying. Furthermore, little progress seems to have been made towards a determination for even simple model systems of the non-universal quantities associated with the fluid critical point. Principal among the non-universal respects in which the critical fluid differs from its Ising counterpart is the nature of the relevant scaling fields which, it has long been appreciated, should comprise *mixtures* of the temperature and chemical potential. However the fundamental issue of the physical character of these scaling fields seems to have been somewhat neglected.

This chapter reviews principal aspects of the progress to date and highlights some of the main difficulties that have hindered experimental, theoretical and computational investigations of the liquid-vapour critical point. Shortcomings in the current knowledge of both universal and non-universal features of critical fluids are discussed and addressed by means of extensive Monte-Carlo simulations of the 2d Lennard-Jones fluid. The simulations confirm the Ising-like nature of the critical fluid while serving to illustrate, at a configurational level, the sense and depth of the universality. With regard to the non-universal features of the fluid critical point, the simulations graphically expose the physical manifestations of the mixed character of the relevant scaling fields and yield the first accurate estimates for the critical temperature.

3.2 Introduction

On the basis of the universality hypothesis, it has been widely, though tentatively assumed that single-component fluids and simple uniaxial magnets are members of a common 'Ising' universality class–the default for systems with short range interactions and a scalar order parameter [33, 2, 34]. Unfortunately, both the experimental and theoretical verification of fluid-magnet universality has proved troublesome. On the experimental front, studies of critical phenomena in fluids are hampered by gravity effects, which induce a density gradient in the sample in

the region of high-compressibility close to the critical point. For several years this gradient effect precluded accurate measurements of fluid critical properties [34]. Only latterly (with the advent of novel optical diffraction techniques) has it been possible to compensate for the effects of gravity and obtain reliable estimates of critical exponents. Reassuringly, these measurements do now seem to be in general agreement with the predictions of the universality hypothesis, albeit in a surprisingly small range of reduced temperature [35]. However, such evidence must necessarily be regarded as somewhat circumstantial, since the exponents themselves convey no insight into the *sense* in which the critical fluid resembles the critical magnet.

Theoretical studies of universality in critical fluids have also encountered a number of obstacles. The main difficulties seem to stem from the fact that the fluid Hamiltonian, unlike that of the magnet, is not symmetric with respect to positive and negative values of the ordering (chemical potential) field. This lack in fluids of the so-called 'particle-hole symmetry' which prevails in magnetic systems has, at times, engendered concern regarding fluid-magnet universality. Some attempts were made to address this matter by incorporating particle-hole asymmetry within the framework of a partly phenomenological Landau-Ginzburg-Wilson (LGW) model. This was effected by inserting *odd* powers of the local ordering field ϕ into the LGW Hamiltonian. Although it was feared initially that these new powers of ϕ may act as relevant perturbations, driving the system to a fixed point other than that of the Ising model [36], subsequent $4 - d$ expansion calculations suggested that the new perturbations are actually irrelevant (at least near $d = 4$), leading instead to additional correction-to-scaling exponents [37].

In fact, the bulk of theoretical work on criticality in fluids has been confined to somewhat artificial systems (such as the asymmetric LGW model) which do not accurately portray microscopic properties such as the interparticle potential. Ideally, more realistic models of fluids should be studied if a comprehensive theoretical understanding of fluid criticality is to emerge. However, although it is possible to recast the partition function of a realistic fluid model in a form ostensibly amenable to renormalisation group methods [33], some basic aspects of

the subsequent analysis have proved recalcitrant [38, 39]. Notwithstanding this, recent advances have been made by Reatto *et al* [40, 41] who developed a novel computational formalism for dealing with critical fluids. Their method yields numerically impressive results for both universal and non-universal critical point parameters, though it seems to rely implicitly upon a small '$4 - d$' approximation. Unfortunately, because of the originality of its formulation, the new method fails to illuminate the essential Ising-like nature of the critical fluid. Consequently the issue of fluid-magnet universality (at least in physical dimensions) remains somewhat equivocal.

The extent of the current knowledge of *non-universal* features of critical behaviour in model fluids is also less than complete. It has long been appreciated that the absence of particle-hole symmetry in fluids should result in relevant scaling fields which comprise *mixtures* of the chemical potential and the temperature. Although there is some understanding of the system-specific factors which control the extent of this mixing [42, 43, 44], little has been done to expose the physical character of the relevant scaling fields themselves. Instead, attention has focused principally on one predicted manifestation of field mixing, a rectilinear diameter ρ_d (the mean of the densities of the two phases on the coexistence curve) displaying a weak energy-like singularity on the approach to criticality [45, 46]. The existence of this singularity (which represents a departure from the classical 'law of rectilinear diameter' requiring a *linear* variation of ρ_d with reduced temperature), does indeed appear to have been borne out by some experiments on critical fluids [47, 48, 49], though not all [50, 51].

As regards computer simulation studies of the liquid-vapour critical point, there is no work even remotely comparable with the work on lattice models. This dearth of large-scale simulations is presumably attributable to the inherent computational difficulties of the fluid system. Unlike many lattice-based spin models (e.g. the Ising model) having discrete spin interactions energies, calculations of particle interactions in fluids can be extremely computationally intensive due to the continuous nature of the interaction potential. The computational problem of locating the critical point in fluids is also substantially harder than in systems

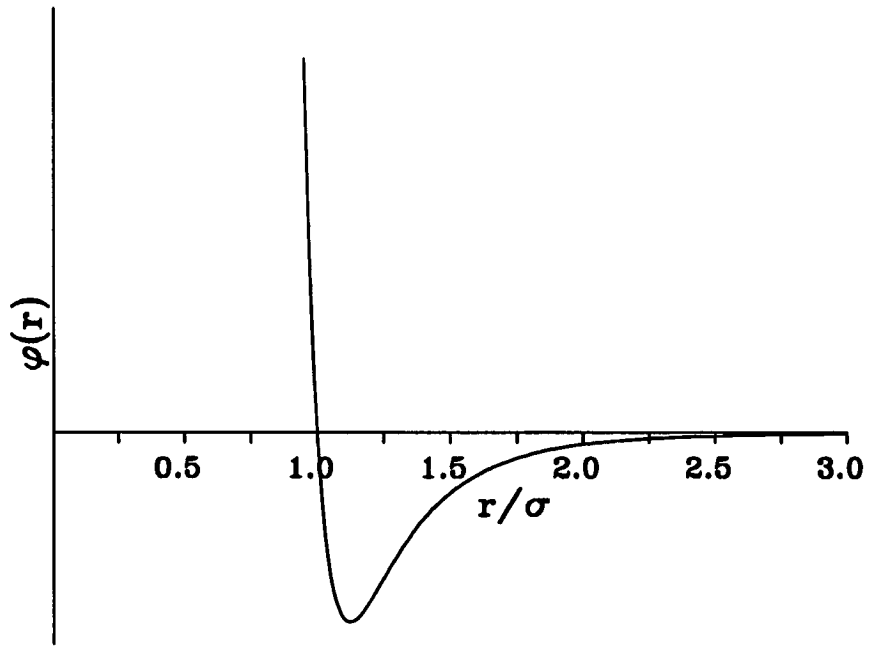

Figure 3.1: The form of the Lennard-Jones potential.

having particle-hole symmetry. While in the Ising magnet, the line of phase co-existence is prescribed by symmetry; in the fluid it must be identified empirically. In addition there are the usual problems of critical slowing down that plague all conventional studies of criticality and that all too often represent the limiting factor for the viability of large-scale simulations of the critical region.

Most previous computational studies have focussed on the prototype model for a realistic fluid–the Lennard-Jones (LJ) system. In this model, particles interact via a semi-empirical pairwise potential. The form of this potential is shown in figure 3.1; it is characterised by a steep repulsive core and a short-range attractive well. Although the LJ system is not a highly accurate representation of a real fluid (see e.g. a comparison with Argon gas [52]), it is the most computationally tractable system with the credentials of a real fluid. In two dimensions, the LJ system finds direct experimental relevance for low-dimensional systems such as submonolayer fluids [53].

Using Monte-Carlo and Molecular Dynamics methods, several groups have mapped

the phase diagram and determined the equation of state for both the 2d and 3d Lennard-Jones systems [54, 55, 56, 57, 58]. However, these studies focussed largely on the one and two-phase regions of the phase diagram. Such efforts that were made to explore the critical region, were not accompanied by a finite-size scaling analysis. Perhaps as a consequence, the various studies yielded quite disparate estimates of the critical temperature and no reliable results regarding the universal properties of the model.

One previous attempt has, however, been made to apply finite-size scaling techniques to the fluid problem. Rovere *et al* [59, 60] employed Monte-Carlo methods to study the liquid-vapour transition of the 2d Lennard-Jones fluid in the canonical (NVT) ensemble. Their study was performed with the aid of a block distribution analysis similar to those described in the preceding chapters, but extended to off-lattice problems. Their approach involved the Monte-Carlo study of the distribution of fluctuations in the *density* of the fluid. Since the density of the system as a whole is fixed in the canonical ensemble, fluctuations were studied within *sub-volumes* of linear dimension l of a system of linear dimension L. Although this approach has the potential to expose the connection with the distribution function of the order parameter in lattice-based members of the 2d Ising universality class, the results obtained were largely qualitative. This failure would seem to reflect the limitations imposed by the choice of the canonical ensemble for the study. Specifically, in order to ensure that density fluctuations were not suppressed it was necessary to choose a sub-block size l, *small* relative to the system size L. Consequently the results were adversely influenced by finite size effects.

In the present work, the 2d Lennard-Jones fluid is revisited with a view to performing a more detailed exposition of its critical behaviour [61]. The strategy of the work follows in the spirit of that by Rovere *et al*, but with significant differences and extensions. Its essential features are as follows. A Monte-Carlo study of the probability distribution of the particle density has been performed within the *grand-canonical* (μVT) ensemble. In this ensemble, the density of the system as a *whole* is a statistical variable and consequently many of the problems encountered in the canonical case can be circumvented. In particular, density

fluctuations can be studied on length-scales comparable with that of the system itself, thereby ameliorating the problems associated with finite size effects. The distribution function of the density is analysed within a finite-size scaling theory, the structure of which is similar to that developed to describe the properties of block coordinates in lattice-based spin systems. The theory has, however, been generalised to take account of the reduced symmetry of the fluid, of which the mixed character of the relevant scaling fields is an essential corollary. According to this theory, field mixing manifests itself most significantly, as a *correction* to the limiting large L behaviour of the critical density distribution. The functional form of this correction has a different symmetry from the limiting form (it is an odd function) and is prescribed by independently-determined functions characteristic of the Ising universality class. As will be seen, the simulations bear out both the universality of the limiting form of the density distribution and, more remarkably, the existence and form of the correction.

3.3 Background

The system considered in this work is a classical, single-component fluid whose particles interact via a pairwise potential ϕ which is a function of the particle separation. The configurational energy Φ (in units of k_BT) is simply the sum over the interactions among the N particles which comprise the fluid.

$$\Phi(\{\vec{r}\}) = \sum_{i<j=1}^{N} \phi(\mid \underline{r}_i - \underline{r}_j \mid) \tag{3.1}$$

The interaction potential ϕ is assumed to take the Lennard–Jones form (c.f figure 3.1)

$$\phi(r) = w[(\sigma/r)^{12} - (\sigma/r)^{6}] \tag{3.2}$$

where σ is a parameter which serves to set the interaction range while w measures the well-depth (in units of k_BT). The particles are confined to a volume $V = L^d$,

(with $d = 2$ in the simulations described later) but it is assumed that the system is thermodynamically 'open' so that particles can be exchanged with a particle reservoir. Both the total energy and the system density are therefore statistical variables whose behaviour is characterised by the grand-canonical partition function, which takes the form:

$$\mathcal{Z}_L = \sum_{N=0}^{\infty} \prod_{i=1}^{N} \left\{ \int d\vec{r}_i \right\} e^{[\mu N - \Phi(\{\vec{r}\})]} \tag{3.3}$$

where μ is the chemical potential (in units of $k_B T$). Within this framework the well depth w and the chemical potential μ define the parameter space for the LJ fluid.

The quantities of central concern are the number density

$$\rho = L^{-d} N \tag{3.4a}$$

and the configurational energy density

$$u = L^{-d} w^{-1} \Phi(\{\vec{r}\}) \tag{3.4b}$$

which has been written in units of the dimensionless well-depth, w. In equilibrium, the statistical behaviour of these variables is fully described by their joint probability distribution, defined formally by

$$p_L(\rho, u) = < \delta \left[\rho - L^{-d} N \right] \delta \left[u - L^{-d} w^{-1} \Phi(\{\vec{r}\}) \right] > \tag{3.5a}$$

or, more explicitly,

$$p_L(\rho, u) = L^d \mathcal{Z}_L{}^{-1} \prod_{i=1}^{N=L^d \rho} \left\{ \int d\vec{r}_i \right\} e^{L^d [\mu \rho - w u]} \delta \left[u - L^{-d} w^{-1} \Phi(\{\vec{r}\}) \right] \tag{3.5b}$$

Within the parameter space of the LJ fluid, the critical point is uniquely specified by critical values μ_c and w_c of the (reduced) chemical potential and well-depth. The deviations of these two control parameters from their critical values

$$t \equiv w_c - w \qquad h \equiv \mu - \mu_c \tag{3.6}$$

control the sizes of the two relevant scaling fields, τ and h, of the fluid fixed point characterising the critical behaviour [62]. It transpires that in the absence of particle-hole symmetry, these scaling fields are expected to comprise linear combinations of the well-depth (temperature) and chemical potential [45].

$$\tau = w_c - w + s(\mu - \mu_c) \qquad h = \mu - \mu_c + r(w_c - w) \tag{3.7}$$

where s and r are system-specific parameters determining the extent of the mixing. Conjugate to the two scaling fields are the two relevant operators, $\mathcal{E}$ and $\mathcal{M}$ defined by the relations

$$< \mathcal{E} >= L^{-d} \frac{\partial \ln \mathcal{Z}_L}{\partial \tau} \qquad < \mathcal{M} >= L^{-d} \frac{\partial \ln \mathcal{Z}_L}{\partial h} \tag{3.8}$$

In systems exhibiting particle-hole symmetry (such as the Ising model), these quantities are simply the energy density and order parameter (magnetisation) respectively. However for fluids, the mixed character of the relevant scaling fields implies that the conjugate operators are themselves linear combinations of the energy and particle densities:

$$\mathcal{E} = \tfrac{1}{1-sr}\left[u - r\rho\right] \qquad \mathcal{M} = \tfrac{1}{1-sr}\left[\rho - su\right] \tag{3.9}$$

where the pre-factor $(1 - sr)^{-1}$ derives from the Jacobian of the transformation of variables. The joint distribution of the mixed operators is simply related to that of the energy and number densities.

$$p_L(\rho, u) = \tfrac{1}{1-sr} p_L(\mathcal{M}, \mathcal{E}) \tag{3.10}$$

In the vicinity of the critical point (where the correlation length ξ is assumed large), one can make a phenomenological postulate (valid for sufficiently large L),

for the finite-size scaling behaviour of this joint distribution of energy and density fluctuations:

$$p_L(\mathcal{M},\mathcal{E}) \simeq \Lambda_{\mathcal{M}}^{+}\Lambda_{\mathcal{E}}^{+}\tilde{p}_{\mathcal{M},\mathcal{E}}(\Lambda_{\mathcal{M}}^{+}\delta\mathcal{M}, \Lambda_{\mathcal{E}}^{+}\delta\mathcal{E}, \Lambda_{\mathcal{M}}h, \Lambda_{\mathcal{E}}\tau) \tag{3.11a}$$

where

$$\Lambda_{\mathcal{E}} = a_{\mathcal{E}}L^{\lambda_{\mathcal{E}}} \qquad \Lambda_{\mathcal{M}} = a_{\mathcal{M}}L^{\lambda_{\mathcal{M}}} \qquad \Lambda_{\mathcal{M}}\Lambda_{\mathcal{M}}^{+} = \Lambda_{\mathcal{E}}\Lambda_{\mathcal{E}}^{+} = L^d \tag{3.11b}$$

and

$$\delta\mathcal{M} \equiv \mathcal{M} - <\mathcal{M}>_c \qquad \delta\mathcal{E} \equiv \mathcal{E} - <\mathcal{E}>_c \tag{3.11c}$$

with

$$\lambda_{\mathcal{E}} = 1/\nu \qquad \lambda_{\mathcal{M}} = d - \beta/\nu \tag{3.11d}$$

the exponents associated with the two relevant scaling fields $\Lambda_{\mathcal{M}}$ and $\Lambda_{\mathcal{E}}$. The subscripts c in equations (3.11c) signify that the averages are to be taken at criticality. Modulo the choice of the non-universal scale factors $a_{\mathcal{M}}$ and $a_{\mathcal{E}}$ (equation 3.11b), it is expected that the function $\tilde{p}_{\mathcal{M},\mathcal{E}}$ will be universal.

The finite-size scaling ansatz (equation 3.11a) is motivated by basic RG postulates [20] and represents a generalisation of the usual finite-size scaling expression characterising the behaviour of the order parameter (magnetisation) in systems exhibiting particle-hole symmetry (c.f.§ 1.11.2) [21]. This special case is recovered by making the substitutions $\mathcal{M} \rightarrow M$ (the magnetisation), $\mathcal{E} \rightarrow E$ (the energy density), $\tau \rightarrow t$, with h the magnetic field. Integration over the energy fluctuations then yields:

$$p_L(M) \simeq \Lambda_{\mathcal{M}}^{+}\tilde{p}_{\mathcal{M}}(\Lambda_{\mathcal{M}}^{+}M, \Lambda_{\mathcal{M}}h, \Lambda_{\mathcal{E}}t) \tag{3.12a}$$

where

$$\tilde{p}_{\mathcal{M}}(x,y,z) \equiv \Lambda_{\mathcal{E}}^{+}\int d\mathcal{E}\,\tilde{p}_{\mathcal{M},\mathcal{E}}(x, \Lambda_{\mathcal{E}}^{+}\delta\mathcal{E}, y, z) \tag{3.12b}$$

which is simply a restatement of equation (1.56).

Preliminary evidence supporting the validity of the generalised scaling ansatz (equation 3.11a) as a description of the near-critical properties of fluids is provided by its predictions concerning the behaviour of the rectilinear diameter ρ_d, the mean of the densities of the two phases on the liquid-vapour coexistence curve. According to scaling theories of the fluid free-energy and equation of state [44, 45], the rectilinear diameter is expected to display a weak energy-like singularity on the approach to criticality. The amplitude of this singularity is predicted to be proportional to the parameter s controlling the degree of mixing of the chemical potential μ into the temperature-like scaling field τ. That this is consistent with equation (3.11a) can be seen as follows.

The average density of the system is given by

$$< \rho >= \int \int \rho p_L(\rho, u) du d\rho \tag{3.13}$$

now, employing equations (3.9) and (3.10) one finds

$$\begin{aligned} < \rho > -\rho_c &= (1 - sr)^{-2} \int d\mathcal{E} \int d\mathcal{M} \, (\mathcal{M} + s\mathcal{E}) p_L(\mathcal{M}, \mathcal{E}) \\ &= (1 - sr)^{-2} \{ < \mathcal{M} > + s < \mathcal{E} > \} \end{aligned} \tag{3.14}$$

The rectilinear diameter is defined as

$$\begin{aligned} \rho_d - \rho_c &= \frac{1}{2} \left\{ < \rho >^+ + < \rho >^- \right\} - \rho_c \\ &= (1 - sr)^{-2} \left\{ < \mathcal{M} >^+ + < \mathcal{M} >^- + s(< \mathcal{E} >^+ + < \mathcal{E} >^-) \right\} \end{aligned} \tag{3.15}$$

where here the superscripts $^+$ and $^-$ denote quantities measured on either side of the coexistence curve (defined by $h = 0$). The known symmetries of the Ising problem then imply that

$$< \mathcal{M} >^{\pm} \sim \pm \mid \tau \mid^{(d - \lambda_{\mathcal{M}})/\lambda_{\mathcal{E}}} \tag{3.16a}$$

$$< \mathcal{E} >^{\pm} \sim \mid \tau \mid^{(d - \lambda_{\mathcal{E}})/\lambda_{\mathcal{E}}} \tag{3.16b}$$

It therefore follows that

$$\rho_d - \rho_c \sim \frac{s}{(1-sr)^2} \mid \tau \mid_{h=0}^{(d-\lambda\varepsilon)/\lambda\varepsilon} \sim s \mid t \mid^{1-\alpha} \tag{3.17}$$

where $\rho_c \equiv < \rho >_c$, and the scaling relation $d = (2-\alpha)/\nu$ has been employed. The scaling ansatz (equation 3.11a) is therefore seen to reproduce the diameter singularity observed in critical fluids.

The specific concern of the present work is with the block distribution function of the fluid number density. From equations (3.5a), (3.9), (3.10) and (3.11a),

$$\begin{aligned} p_L(\rho) &= \int du p_L(\rho, u) \\ &\simeq \Lambda_{\mathcal{M}}^{+}\Lambda_{\mathcal{E}}^{+} \int d\mathcal{E}\, \tilde{p}_{\mathcal{M},\mathcal{E}}(\Lambda_{\mathcal{M}}^{+}[\rho - \rho_c - s\delta\mathcal{E}], \Lambda_{\mathcal{E}}^{+}\delta\mathcal{E}, \Lambda_{\mathcal{M}}h, \Lambda_{\mathcal{E}}\tau) \end{aligned} \tag{3.18}$$

Now, in the vicinity of the critical point, the typical size of fluctuations in the energy-like operator, $\delta\mathcal{E}$, will vary with system size L as $[\Lambda_{\mathcal{E}}^{+}]^{-1} = L^{-(1-\alpha)/\nu}$, while the typical scale of the ordering operator fluctuation, $\delta\mathcal{M}$ will vary as $[\Lambda_{\mathcal{M}}^{+}]^{-1} = L^{-\beta/\nu}$. Accordingly, and to within corrections which are down on the leading term retained by of order $L^{-(1-\alpha-\beta)/\nu}$, the contribution of the energy fluctuations to the first argument of the function $\tilde{p}_{\mathcal{M},\mathcal{E}}$ in equation 3.18 can be neglected. The integration on $\mathcal{E}$ can then be performed, yielding

$$p_L(\rho) \simeq \Lambda_{\mathcal{M}}^{+}\tilde{p}_{\mathcal{M}}(\Lambda_{\mathcal{M}}^{+}[\rho - \rho_c], \Lambda_{\mathcal{M}}h, \Lambda_{\mathcal{E}}\tau) \tag{3.19}$$

where $\tilde{p}_{\mathcal{M}}$(x,y,z) is the universal function (identified in equation 3.12a), appropriate to the distribution of the magnetisation in the Ising context. This is the first key result of this section: In the vicinity of the critical point (and to within the accuracy afforded by the aforementioned corrections), the limiting density distribution of the 2d fluid is expected to match the limiting magnetisation distribution of the 2d Ising ferromagnet. In particular, precisely at criticality, equation (3.19) implies (recalling 3.11b):

$$p_L(\rho) \simeq a_{\mathcal{M}}{}^{-1} L^{\beta/\nu} \tilde{p}^*_{\mathcal{M}} \left(L^{\beta/\nu} a_{\mathcal{M}}{}^{-1}[\rho - \rho_c]\right) \tag{3.20}$$

where

$$\tilde{p}^*_{\mathcal{M}}(x) = \tilde{p}_{\mathcal{M}}(x, y = 0, z = 0) \tag{3.21}$$

is a function describing the universal and statistically scale-invariant configurational spectrum characteristic of the critical point of Ising-like systems. The form of this function has been well-established in studies of the 2d spin-$\frac{1}{2}$ Ising model and its claim to describe other members of the 2d Ising universality class substantiated by studies of the spin-1 Ising model and the ϕ^4 model [22].

In addition to the anticipated universality of the *critical* density distribution function, equation (3.19) also implies universal behaviour for the *near-critical* form of $p_L(\rho)$, subject only to the requirement that L and ξ are both large on microscopic length-scales. This near-critical universality may be verified either by determining $p_L(\rho)$ for points in the neighbourhood of the critical point, or alternatively and more straightforwardly, by exploiting the properties of the *derivatives* of the *fixed-point* distribution function with respect to the control parameters w (which determines the critical temperature) and the chemical potential μ. If $p_L(\rho)$ is indeed a universal function for points in parameter space lying close to the critical point, then its functional form can be represented as a Taylor expansion with respect to the universal fixed point form $\tilde{p}^*_{\mathcal{M}}$. It follows that the terms in this expansion (most significantly the first derivatives) must collectively be universal. The form of the first derivatives of $p_L(\rho)$ can be deduced by appeal to its definition equation (3.6a), from which one finds

$$\frac{\partial p_L(\rho)}{\partial \mu} = L^d \left[\rho - < \rho >\right] p_L(\rho) \tag{3.22a}$$

and

$$\frac{\partial p_L(\rho)}{\partial w} = -L^d \left[< u(\rho) > - < u >\right] p_L(\rho) \tag{3.22b}$$

where $< u(\rho) >$ is the mean energy density for a given ρ. These derivative functions play a dual role. Firstly in the context of the simulations (to be described in the following section) they provide a means for locating and tracking

the coexistence curve. Secondly and more significantly, they together provide a testable universal relation embodying one form of the scaling field mixing, namely the contribution of the temperature to the scaling field h. Specifically, utilising the proposed density scaling form (3.19), together with the w-dependence of the scaling fields recorded in equations (3.7) and (3.6) and feeding the consequences into equation (3.22b), one finds that at criticality (for which $< u > \equiv u_c$)

$$< u(\rho) > - u_c \simeq L^{-d} \left\{ r \Lambda_{\mathcal{M}} \tilde{p}_{\mathcal{M}}^{(1,0)}(\Lambda_{\mathcal{M}}^{+}[\rho - \rho_c]) + \Lambda_{\varepsilon} \tilde{p}_{\mathcal{M}}^{(0,1)}(\Lambda_{\mathcal{M}}^{+}[\rho - \rho_c]) \right\} \quad (3.23)$$

where

$$\tilde{p}_{\mathcal{M}}^{(1,0)}(x) = \frac{\partial \ln \tilde{p}_{\mathcal{M}}(x, y, 0)}{\partial y} \Big|_{y=0} \quad (3.24a)$$

$$\tilde{p}_{\mathcal{M}}^{(0,1)}(x) = \frac{\partial \ln \tilde{p}_{\mathcal{M}}(x, 0, z)}{\partial z} \Big|_{z=0} \quad (3.24b)$$

are universal functions. The first of these functions has a simple form:

$$\tilde{p}_{\mathcal{M}}^{(1,0)}(x) \equiv x \quad (3.25)$$

a result which follows from the Ising context (equation 3.12a) together with the identity $\partial \ln p_L(\mathcal{M})/\partial h = L^d \mathcal{M}$. The second function is non-trivial: its form has (like that of $\tilde{p}_{\mathcal{M}}^{*}$) been established in earlier Monte Carlo studies of the Ising universality class [22]. Substituting (3.25) into (3.23) and appealing to (3.11b) yields

$$< u(\rho) > - u_c \simeq r[\rho - \rho_c] + a_{\varepsilon} L^{-d+1/\nu} \tilde{p}_{\mathcal{M}}^{(0,1)}(a_{\mathcal{M}}{}^{-1} L^{\beta/\nu}[\rho - \rho_c]) \quad (3.26)$$

where r (equation 3.7) controls the temperature-dependence of the ('ordering') scaling field h, and thus the limiting critical slope of the coexistence curve which is identified by the condition $h = 0$ (c.f. figure 3.2).

Equation (3.26) provides an explicit test of one form of field-mixing, a thermal contribution to the ordering scaling field. To illustrate the consequences of the other form of mixing (the contribution of the chemical potential to the thermal

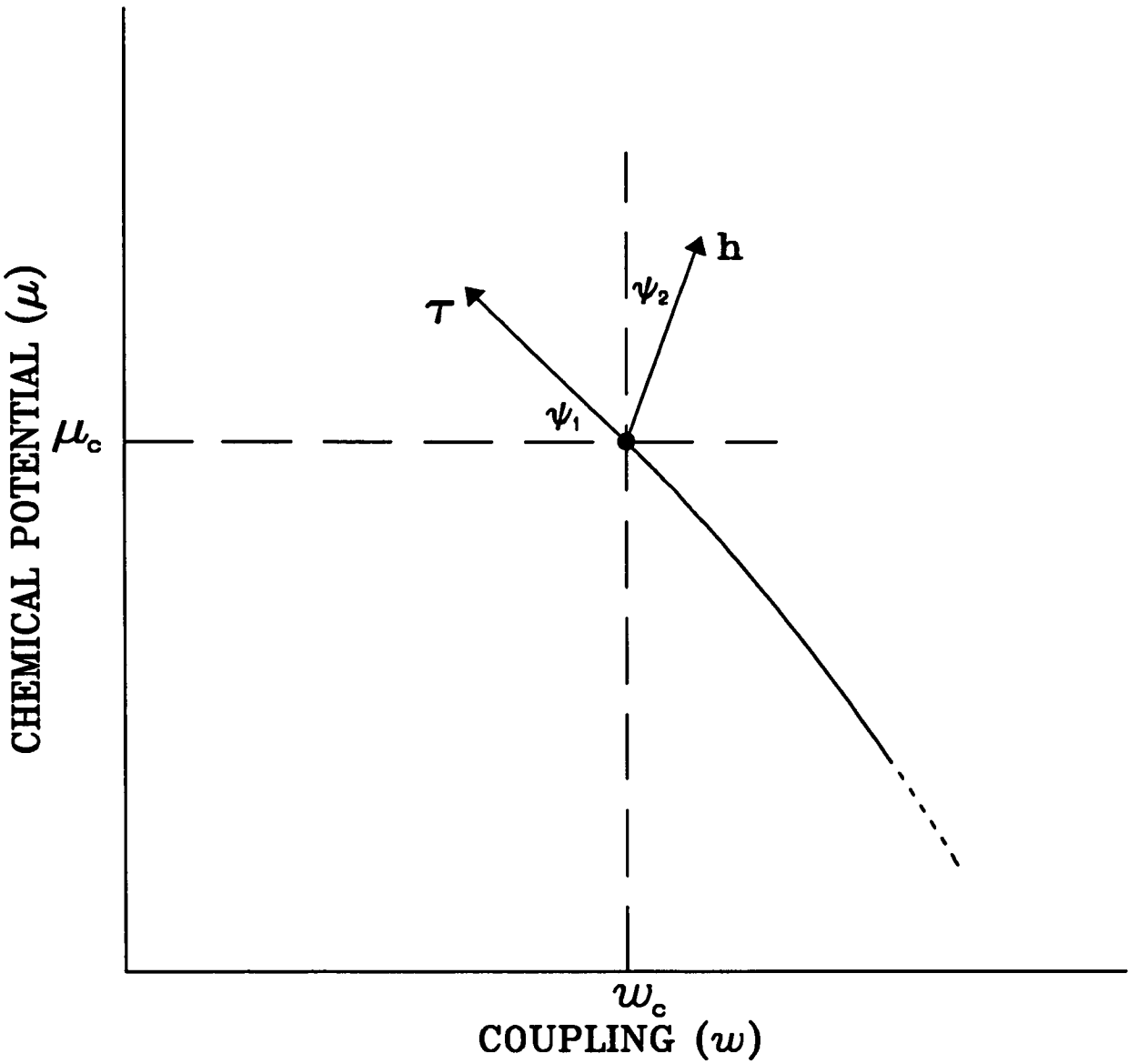

Figure 3.2: Schematic representation of the liquid-vapour coexistence curve showing the directions of the relevant scaling fields. The angles ψ_1 and ψ_2 are related to the field-mixing parameters s and r (equation 3.7) by $r = \tan\psi_1$ and $s = \tan\psi_2$.

scaling field τ) it is necessary to go beyond the approximations underlying equation (3.19) and consider the contribution of the energy fluctuations to $\tilde{p}_{\mathcal{M}}$. This may be achieved on a perturbative basis by expanding equation (3.18) in powers of the mixing parameter s . In this way, the leading corrections can be separated out from equation (3.19) to give

$$p_L(\rho) \simeq \Lambda_{\mathcal{M}}^{+}\tilde{p}_{\mathcal{M}}(\Lambda_{\mathcal{M}}^{+}[\rho-\rho_c], \Lambda_{\mathcal{M}}h, \Lambda_{\mathcal{E}}\tau) + \Delta p_L(\rho) \tag{3.27}$$

with

$$\begin{aligned}\Delta p_L(\rho) &= -s\int d\mathcal{E}\frac{\partial}{\partial\rho}\delta\mathcal{E}p_L(\mathcal{M},\mathcal{E}) \\ &= -s\frac{\partial}{\partial\rho}\left\{[< u(\rho) > -u_c - r(\rho-\rho_c)]\,p_L(\rho)\right\} + O(s^2)\end{aligned} \tag{3.28}$$

Substituting this result into equation (3.26) then gives

$$\Delta p_L(\rho) \simeq \Lambda_{\mathcal{M}}^{+}\left[-sa_{\mathcal{E}}\; {a_{\mathcal{M}}}^{-1}L^{-(1-\alpha-\beta)/\nu}\right]\frac{\partial}{\partial x}\left\{\tilde{p}_{\mathcal{M}}^{(0,1)}(x)\tilde{p}_{\mathcal{M}}^{*}(x)\right\}_{x={a_{\mathcal{M}}}^{-1}L^{\beta/\nu}[\rho-\rho_c]} \tag{3.29}$$

Equation (3.29) is the second key result of this section. The leading correction to the density distribution (which derives from the contribution of the energy operator in the fluctuation spectrum of the density) is seen to reveal the L-dependence anticipated in the argument used to justify equation (3.19). This correction term explicitly captures the consequences of the field-mixing represented in the parameter s. Moreover it is prescribed by functions $\tilde{p}_{\mathcal{M}}^{(0,1)}$ and $\tilde{p}_{\mathcal{M}}$ which are characteristic of the Ising universality class and both *even* in the scaling variable x. Equation (3.29) therefore represents the leading contribution to the critical distribution that is *odd* in the scaling variable x. However, and notwithstanding its status as a 'correction' to the leading behaviour, it transpires that the symmetry of these functions can be exploited through computer simulation to provide striking corroboration of both the existence and functional form of the correction.

Finally, it will prove useful to consider the finite-size scaling properties of the isothermal compressibility $K_T(L)$. According to the fluctuation response theorem $K_T(L)$ is defined as follows:-

$$< (\Delta\rho)^2 >_L = < (\rho - < \rho >)^2 >_L = L^{-d} < \rho >^2 k_B T K_T(L) \qquad (3.30)$$

It then follows from the structure of the scaling form (3.19) that the second moment of the density distribution behaves as

$$< (\Delta\rho)^2 >_L = L^{-2\beta/\nu} f_2(\Lambda_{\mathcal{M}} h, \Lambda_{\mathcal{E}} \tau) \qquad (3.31)$$

where f_2 is some scaling function. Combining equations (3.30) and (3.31), and making use of the scaling relation $\gamma + 2\beta = d\nu$ then yields

$$K_T(L) = L^{\gamma/\nu} (< \rho >^2 k_B T)^{-1} f_2(\Lambda_{\mathcal{M}} h, \Lambda_{\mathcal{E}} \tau) \qquad (3.32)$$

which shows that the isothermal compressibility scales with system-size as $L^{\gamma/\nu}$. This relation provides a further test of universality (this time embracing the value of the exponent ratio γ/ν), that can also be exploited by simulation.

To summarise the principal results of this section, it is found that in the critical region, the joint distribution of the fluctuations of the energy and number densities is describable by a finite-size scaling expression given by equation (3.11a). This relation implies that the limiting distribution of the number density coincides with the limiting distribution of the magnetisation in the Ising model, as expressed by equation (3.19). The leading correction to the large L density distribution is found to manifest the mixed character of the scaling fields that results from broken particle-hole symmetry. This correction has a *different* symmetry from the asymptotically-dominant form and is prescribed by independently-determined functions characteristic of the Ising universality class. Accordingly it represents a potentially distinctive signature of the field-mixing phenomenon.

3.4 Monte Carlo Studies

3.4.1 Computational Aspects

The Monte Carlo (MC) simulations described here were implemented in parallel on the Distributed Array Processors (DAPs) at the Edinburgh Parallel Computing Centre. The DAP consists of a large number of independent processing elements (PE's) which are arranged as a two-dimensional square array. The edges of the array are connected together to form a torus topology. Processors execute instructions concurrently and communicate with their four nearest neighbours via orthogonal data highways. Although each processor operates on its own data, all processors execute *identical* instructions in lockstep. The DAP is therefore known as a Single Instruction Multiple Data (SIMD) computer.

Many systems for which a MC update scheme is typically implemented, possess a high degree of inherent parallelism. The parallel architecture of the DAP computer allows this parallelism to be exploited for dramatic improvements in simulation speed. Systems that benefit from a parallel implementation can therefore be tackled much more effectively on a parallel computer than on a machine of conventional architecture. Indeed, the benefits that accrue from a parallel implementation often scale linearly with the number of processors brought to bear on the problem. Thus, compared with commonly available serial machines, a modestly-sized parallel computer (having some 10^3 processors) can yield a speed increase of up to three orders of magnitude.

The 2d Lennard-Jones fluid is a system that possesses a high degree of parallelism and is therefore a good candidate for simulation on the DAP computer. In order to effect the mapping of the fluid onto the DAP architecture, a *geometrical* decomposition was employed. This involved partitioning the 2-dimensional simulation space into a square array of $\mathcal{L} \times \mathcal{L}$ square 'cells', each of side 'a'. Periodic boundary conditions were applied to the array as a whole. Each cell was assigned to the control of an individual member of the processor array, in the sense that the given

processor element was responsible for handling the coordinates and interactions of those particles within the given cell. The DAP architecture and general aspects of parallel mapping strategy are described in appendix B.1 and in reference [32]. A review of liquid-state simulations is given by Allen and Tildesley [63].

The choice of the cell size 'a' required that a compromise be struck between two unfavourable limits. If the cell size is too small then particles in one cell interact with particles in many distant cells. Consequently the task of calculating the interactions involves communication between many different PE's thus impairing the speed of the simulation. Conversely, if the cell size is too large then the simulation becomes badly 'load-balanced' in the sense that those cells which control a 'dense' region of the system have a considerably heavier computational burden than those that control only a few particles. In practice, the cell size was set equal to the Lennard-Jones cutoff $a = r_c$, the choice of which is described below. This assignment ensured that interactions emanating from particles in one cell do not extend beyond the 8 cells adjacent to it.

The choice of the system size $\mathcal{L}$ was motivating primarily by the concern that it should be large enough to minimise errors from corrections to scaling. Unfortunately, an upper limit on the choice of $\mathcal{L}$ is imposed by the need to perform adequate equilibration and to gather sufficient statistics in the face of critical-slowing-down. The possible choices of $\mathcal{L}$ are further restricted by the characteristics of the DAP processor array which, for reasons of efficiency, favour choices of the form $\mathcal{L} = 2^n$. In practice it was found feasible to study two system sizes consistent with the above considerations. The two cases studied had $\mathcal{L} = 8$ and $\mathcal{L} = 16$ containing respectively of order 100 and 400 particles at criticality. As the number of available processors (4096) greatly exceeds the number of cells in both cases, it was possible to study a number of independent systems simultaneously, thus enhancing considerably the rate of data acquisition once all systems had equilibrated.

When simulating systems whose interaction potential decays rapidly with particle separation, it is usual to truncate the potential to reduce the computational effort.

In the present work the LJ potential was truncated at $r_c = 2.0\sigma$. This value is at the lower end of the range of cutoff values to be found in the literature e.g. Rovere *et al* have $r_c = 2.5\sigma$, while Singh *et al* chose $r_c = 10\sigma$. It was chosen partly in anticipation of the computational difficulties associated with the critical point but mainly in recognition of the fact that differences in the assignment of r_c have no consequences for the universal parameters. It should be noted however that the choice of the cutoff does have consequences for assignments of non-universal parameters such as the critical temperature.

A Metropolis Monte Carlo algorithm was employed for the simulations. Its form is similar to that described by Adams for the grand canonical ensemble [64], but is tailored for the critical region by implementing only particle transfers (insertions and deletions); no particle movement algorithm is employed. This choice (which clearly realises an ergodic system), has the advantage that it concentrates the computational effort on the long-lived density fluctuations which are the bottleneck for phase-space evolution in the critical region. Unfortunately, the acceptance rate for this procedure can be quite low, especially at high densities were there are few opportunities to insert new particles and existing particles are typically bound tightly to their neighbours.

For future reference, it should be noted that the algorithm uses not the true (reduced) chemical potential μ, but an effective chemical potential μ^* which is related to the true chemical potential by the relation

$$\mu = \mu^\star + \mu_0 - ln\left(\frac{N}{\mathcal{L}^d}\right) \tag{3.33}$$

where μ_0 is the chemical potential in the non-interacting (ideal gas) limit. Use of this effective value ensures that the algorithm satisfies detailed balance. Its form reflects the differences in which the insertion and deletion operations sample phase space. When nominating a candidate particle for deletion one simply chooses a particle at random from those present. In contrast, when inserting a particle, one must first choose a random insertion site from the whole volume before attempting to insert the particle. The relative asymmetry of these operations is responsible

for the appearance of the particle number and system size in equation (3.33).

Following convention, all future references to the particle density will be expressed in terms of the mean number of particles, $\rho^\star$, contained within the region defined by the Lennard-Jones potential parameter σ:

$$\rho^\star = \rho\sigma^d = N\left[\frac{\sigma}{\mathcal{L}a}\right]^d \tag{3.34}$$

The observables sampled from the simulation data were the block probability distribution $p_L(\rho)$ and the energy function $u(\rho)$ (which is used to determine the derivative function $\partial p_L(\rho)/\partial\epsilon^*$). In accordance with its definition, $p_L(\rho)$ was determined in the form of a histogram. The energy function $u(\rho)$ was also determined in histogram form by accumulating the interaction energy for each value of ρ explored in the course of the simulation.

3.4.2 Equilibration and Sampling Considerations

The principal concern of this work is with the behaviour on and around the liquid-vapour coexistence curve and the critical point in which it formally terminates. Extended equilibration times are associated with both of these regions. In the vicinity of the coexistence curve metastability effects are generally to be expected, signalled by an abrupt shift in the system density at some point along the Markov chain. In the neighbourhood of the critical point, the phenomenon of critical-slowing-down hinders equilibration. Since serious measuring errors can arise from an improperly equilibrated system, considerable efforts were expended to try to gauge the time required for proper equilibration.

To this end, the average density and block distribution function were monitored throughout the simulation runs in an attempt to identify any transient (non-equilibrium) effects. This monitoring was effected by dividing each run into a number of consecutive measuring periods, each consisting of some 2×10^5 Monte

Carlo steps *per cell* (MCS). Observations of the density were accumulated over each measuring period and used to construct the block distribution function. In order to reduce correlations in the data, successive observations were separated by a number of intermediate MCS. Comparisons of the data built up over each period thus served to aid the identification of any systematic trends in the behaviour.

Using this strategy, test runs were carried out in the vicinity of the coexistence curve, located in a manner described in the following subsection. The test runs comprised a pair of simulation runs, each assigned identical model parameters but different starting configurations. In one case the run was started from a pure vapour configuration while in the other a pure liquid configuration was used. The behaviour observed in the test runs was found to be dependent on the system size, the initial configuration and the chosen position on the phase boundary.

Well within the two-phase region, metastability effects were very pronounced. An example of this is illustrated in figure 3.3 which shows the time evolution of the density distribution for a system of size $\mathcal{L} = 16$ that lies close to the coexistence curve at a temperature 1% below criticality. The distributions shown represent data accumulated over a series of measuring periods. The initial state of the system lies in the pure vapour phase; the chemical potential slightly favours the liquid phase. Evidently, the system remains in the metastable vapour phase for approximately 6×10^5 MCS before condensing, over a relatively short period, to the liquid phase where it remains. In this regime, the equilibration period (controlled by the potential extent of metastability) was set at 1×10^6 MCS. Corresponding tests on the $\mathcal{L} = 8$ system, revealed no abrupt shifting of the sampled density, showing that metastability problems are less acute, presumably as a result of the smaller free energy barrier. For the $\mathcal{L} = 8$ system, 3×10^5 MCS was found to be adequate for equilibration.

Closer to the critical point the behaviour was markedly different. The density fluctuations were found to be very much longer lived than in the two-phase region. This was manifest as slow oscillations of the density between well separated ranges which represent the vestiges of the coexisting phases. The presence of these

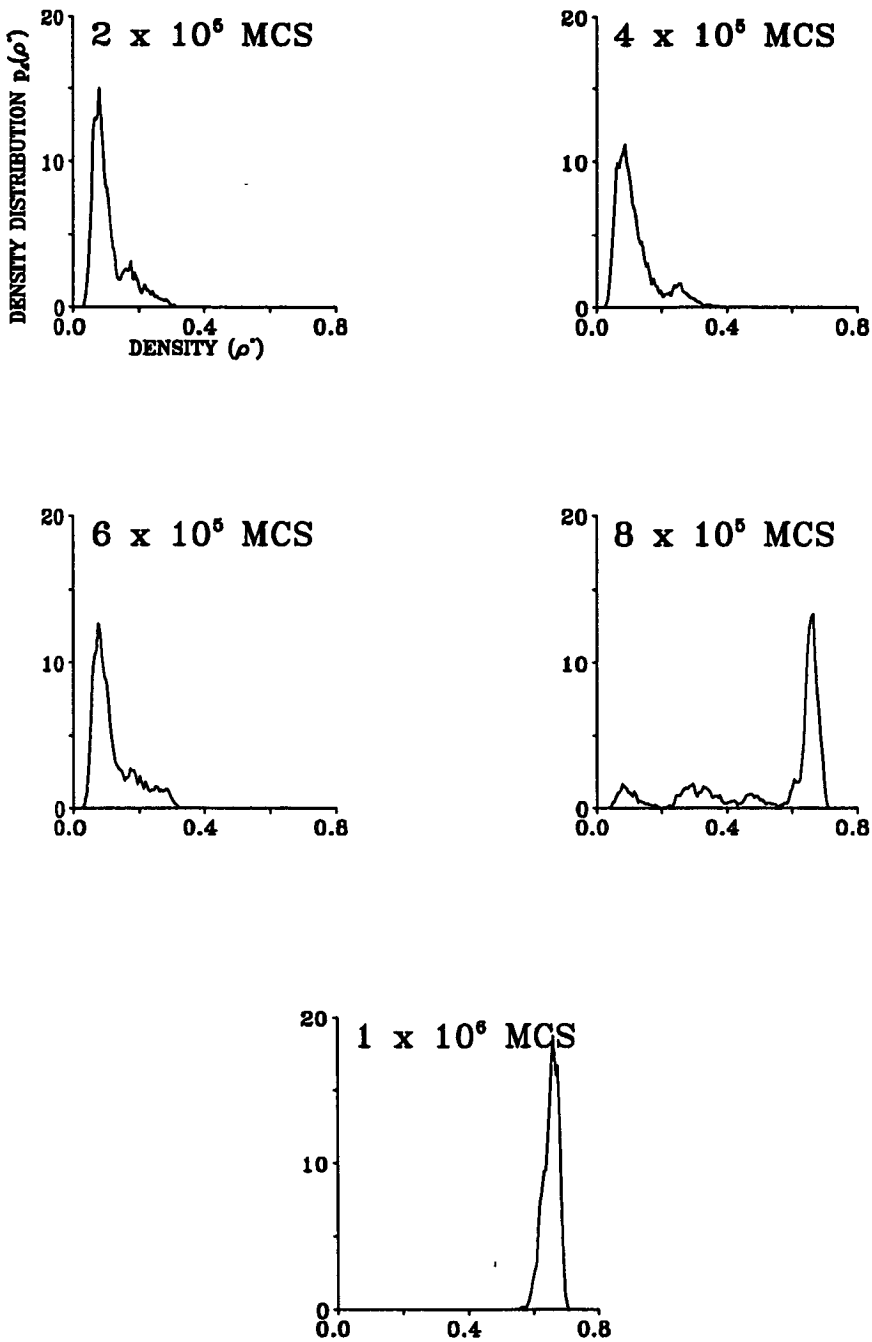

Figure 3.3: The time-evolution of the density distribution of a $\mathcal{L} = 16$ system initially in a metastable vapour phase, at a temperature 1% below criticality.

fluctuations made it difficult to discern underlying trends in the density behaviour. The problems are illustrated in figure 3.4, which shows the time-evolution of the density distribution very close to criticality (again for $\mathcal{L} = 16$), the data being gathered in the same fashion as described above. In this regime, guided by the behaviour of the mean density, equilibration periods of 2.5×10^6 and 4×10^5 were used for the $\mathcal{L} = 16$ and $\mathcal{L} = 8$ systems respectively. For both system sizes, the number of equilibration steps required in the region beyond the critical point was considerably less than in the critical region and decreased systematically with increasing temperature. Typical critical configurations for the $\mathcal{L} = 16$ system are shown in figure 3.5.

The number of sample observations required to build a time-invariant distribution free of spurious structure, also depended on the proximity to the critical point. For the $\mathcal{L} = 16$ system in the two phase region, the data shown below typically involved 1×10^6 observations, each separated by 15 intermediate MCS. In the critical region observation periods were required to be long compared to the typical time-scale of the critical fluctuations. Measuring periods comprising up to 2×10^6 observations separated by 25 intermediate MCS were therefore utilised. Observations times of approximately half these values were found to be adequate for the $\mathcal{L} = 8$ system.

3.4.3 Locating the Coexistence Curve and Critical Point

The computational problem posed by the location of the critical point in the fluid is substantially harder than its magnetic counterpart. In (symmetric) magnetic systems the coexistence curve is prescribed by symmetry. By contrast in the fluid, no information is available *a-priori* regarding the locus of the phase boundary which must therefore be determined empirically, as a prelude to locating the critical point itself.

Precisely on the liquid-vapour phase boundary, the free energy of the coexisting phases is equal and the system fluctuates with equal probability between the two phases. Accordingly, the measured block distribution function $p_L(\rho)$ on the coexis-

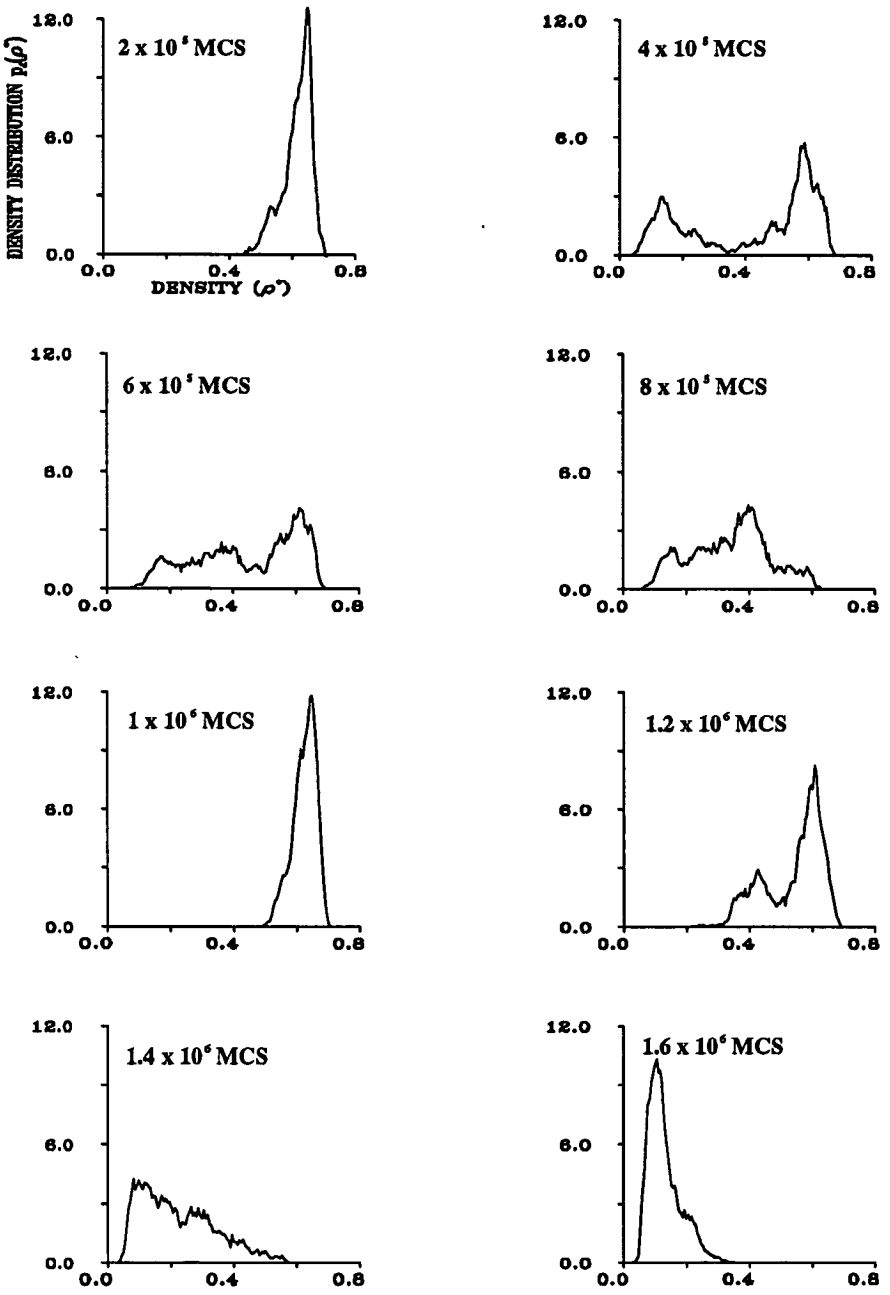

Figure 3.4: The time-evolution of the density distribution of a $\mathcal{L} = 16$ system at criticality, showing the large, slow fluctuations in the density.

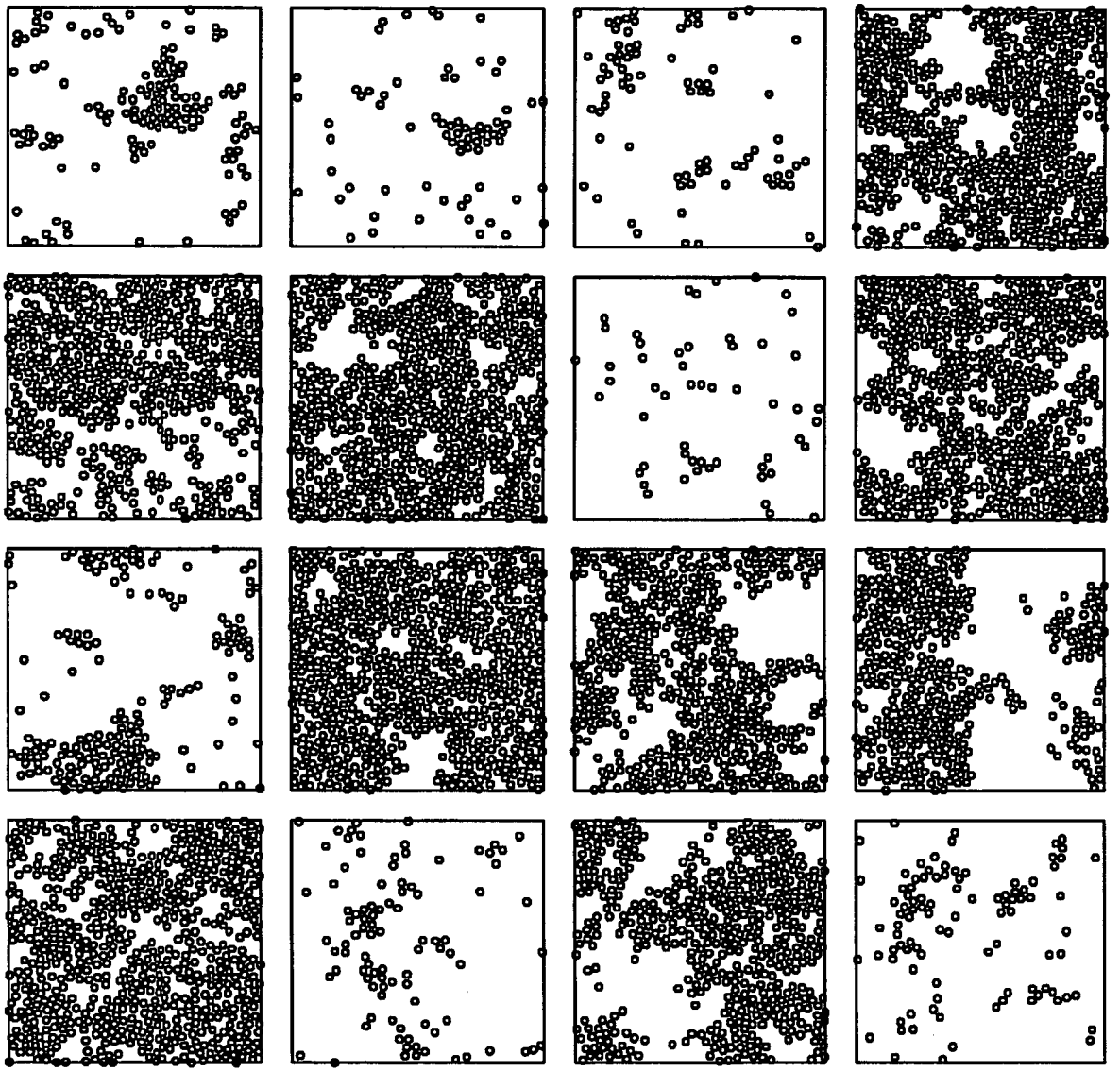

Figure 3.5: Typical particle configurations of the $\mathcal{L} = 16$ system at criticality.

tence curve must be doubly peaked with equal weight in each peak. A reasonable criterion for mapping the coexistence curve (and hence for locating the critical point), is therefore to tune the model parameters ($\mu^\star$ and w) such that equal weight is maintained in both peaks. In practice, this task is made substantially easier by the use of the *derivatives* of the density distribution with respect to the control parameters μ and w. The derivative with respect to w is provided by the energy function measured in the simulation (equation 3.22b); the derivative with respect to μ is trivially related to the distribution itself (equation 3.22a). Appeal to these derivatives provides initial estimates (subsequently refinable) for the changes in μ and w that, together, preserve the equality of heights of the two peaks.

Equilibrium measurements of the block distributions function along the coexistence curve are given in figure 3.6 and figure 3.7 for the $\mathcal{L} = 8$ and $\mathcal{L} = 16$ system sizes respectively. Each distribution has been normalised to unit integrated weight. The distributions shown are those which most closely satisfy the equal height criterion.

The feasibility of using the equal-height criterion for accurately locating the coexistence curve, depends crucially on the system size under study. For a given choice of w, great precision was required in the choice of μ to fulfill the criterion: in the $\mathcal{L} = 8$ system it was necessary (for a given choice of coupling w) to specify the chemical potential μ to 4 significant figures. For the $\mathcal{L} = 16$ system, the coexistence curve was identifiable (at substantially more computational cost) to 5 significant figure. These finding reflect the fact that for small system sizes, the discontinuity in the density at the phase boundary is smeared out by finite size effects. Consequently the region of coexistence is moderately wide and the block distribution function relatively stable against small changes in the model parameters. In contrast, for larger system sizes the transition becomes very abrupt and $p_L(\rho)$ becomes extremely sensitive to changes in the model parameters. The coexistence curve in $w - \mu$ space that derives from the distributions of figures 3.6 and 3.7 is presented in figure 3.8. The results for both system sizes are fully consistent with one another to high precision.

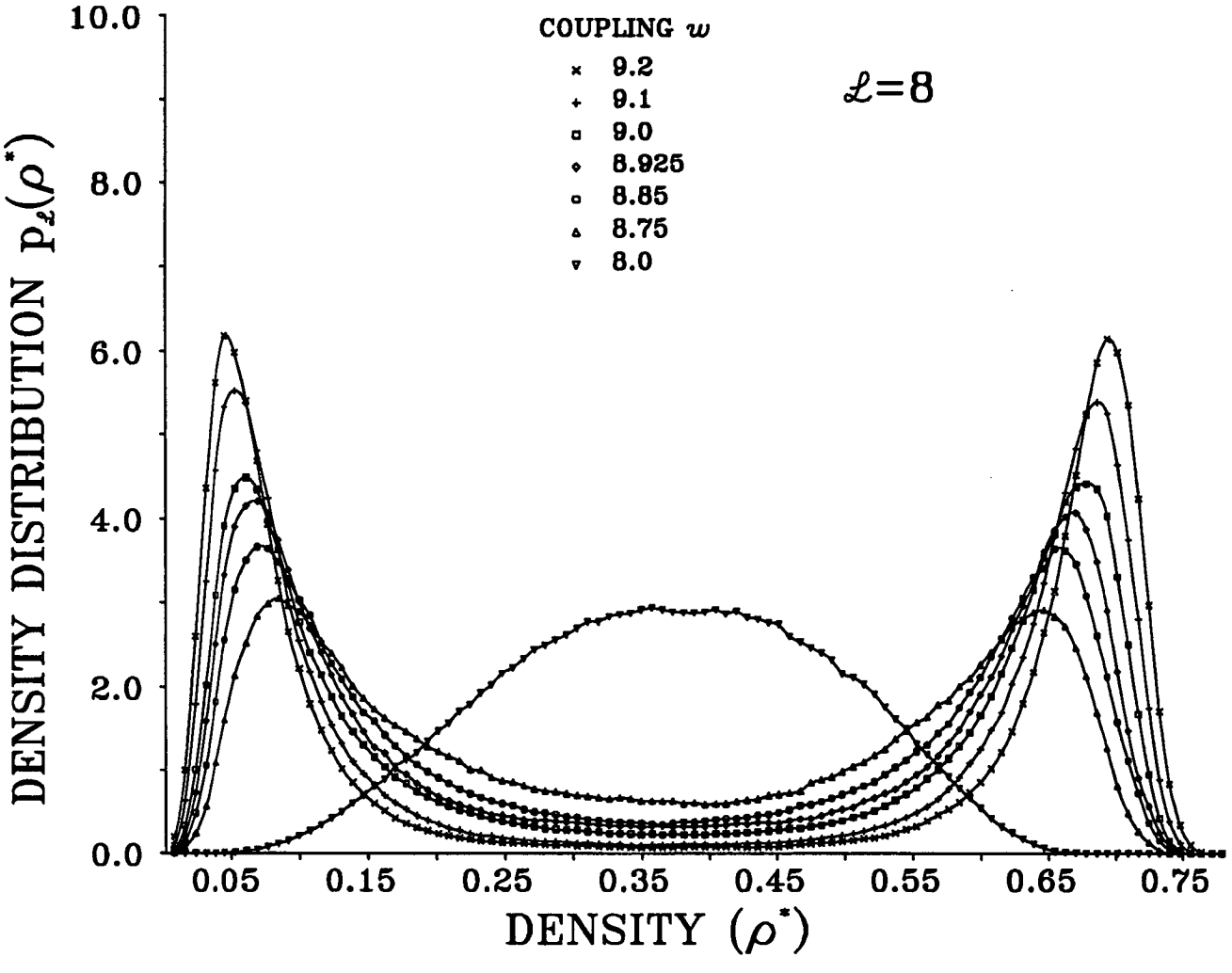

Figure 3.6: The fluid density distributions in a system of size $\mathcal{L} = 8$ for a variety of couplings w along the line of pseudo-coexistence, identified in figure 3.2. The statistical uncertainties are smaller than the symbol sizes; the lines are simply guides to the eye.

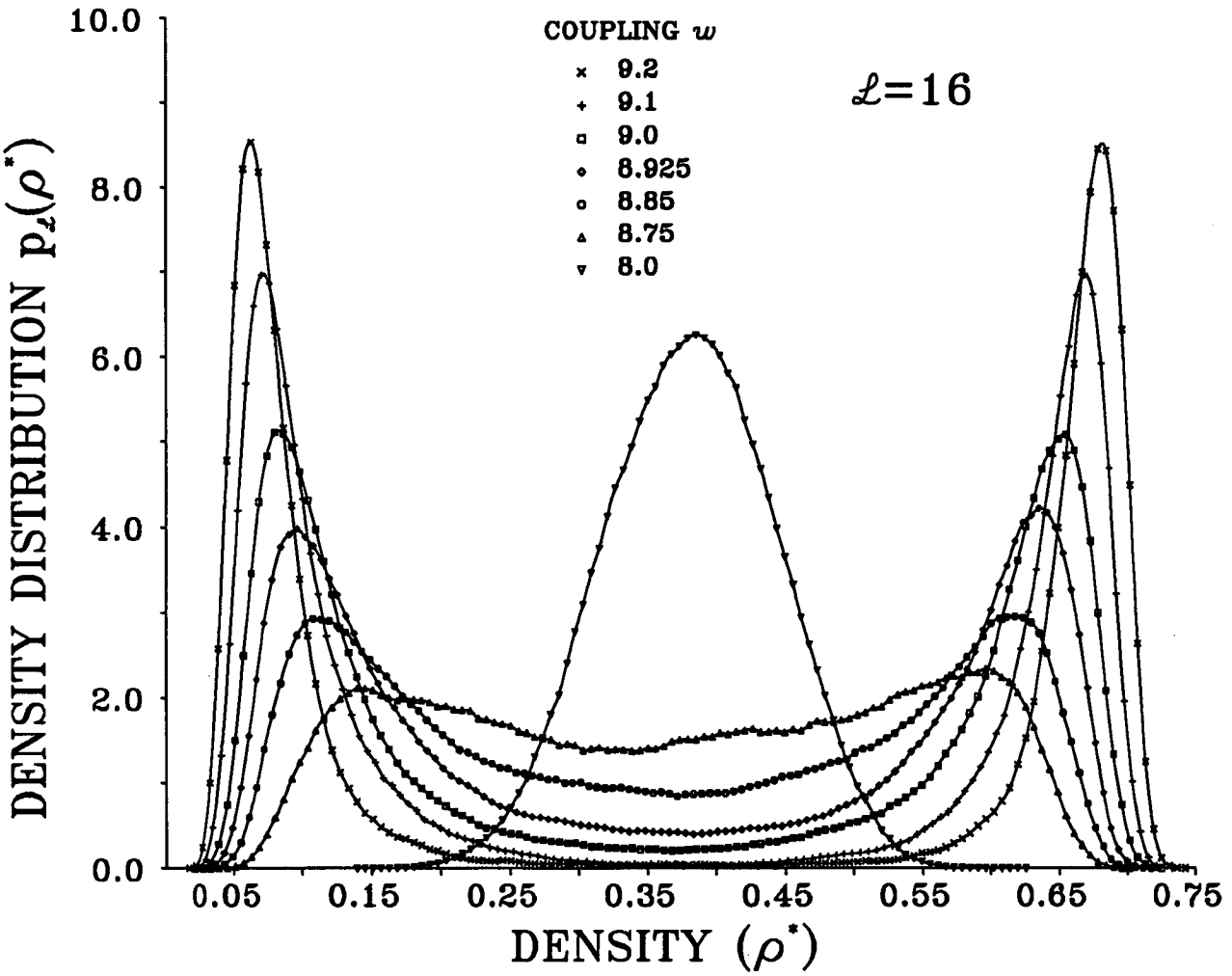

Figure 3.7: The fluid density distributions in a system of size $\mathcal{L} = 16$ for a variety of couplings w along the line of pseudo-coexistence, identified in figure 3.2. The statistical uncertainties are smaller than the symbol sizes; the lines are simply guides to the eye.

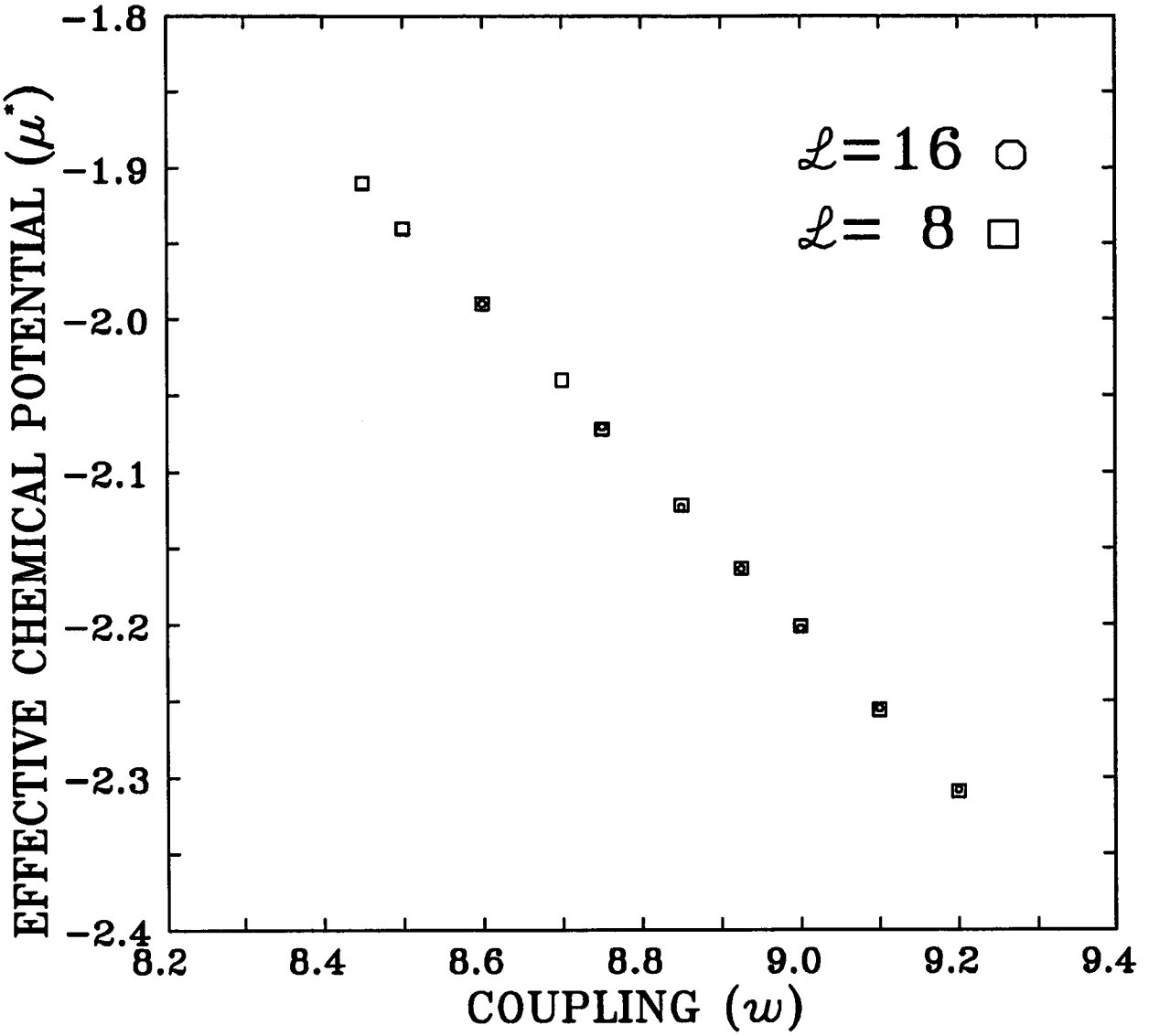

Figure 3.8: The measured line of pseudo-coexistence defined by the set of points in $\mu^* - w$ space for which the density distribution, measured for $\mathcal{L} = 8$ and $\mathcal{L} = 16$, has two peaks of equal height. The uncertainties in the assignments of μ^* for a given w are substantially smaller than the symbol sizes.

In strict terms, the liquid-vapour coexistence curve is defined only as far as the critical point. No distinction between the liquid and vapour phases exists beyond that point. Nevertheless, the critical point does not itself mark the entry to a totally disordered regime. Local order persists beyond the critical point, and for a finite block-size, this fact is reflected in the block distribution function, which retains its dual-peaked character. For convenience the analytic extension of the coexistence curve beyond the critical point (for which the distribution function has two equally weighted peaks) will be referred to as the continuation curve.

The distributions displayed in figures 3.6 and 3.7 exhibit two distinct types of cross-over behaviour which furnish insight into the degree of order in the system and provide an initial estimate of the location of the critical point. From the figures, it is clear that for strong enough couplings the change from $\mathcal{L} = 8$ to $\mathcal{L} = 16$ is accompanied by a sharpening of the double-peaked character of the distribution. This indicates that the system resides in the two-phase region, where the distribution function should asymptotically (for large enough system size $\mathcal{L}$) show two gaussians centred on the densities of the two coexisting phases [60]. On the other hand, for weaker couplings, the change from $\mathcal{L} = 8$ to $\mathcal{L} = 16$ is accompanied by a broadening of the two peaks, and a transfer of weight into the central portion of the distribution. This indicates that the degree of correlated local order (as measured by the bulk correlation length) is small on the scale of the block-size. In this regime, the limiting distribution is a single gaussian.

The critical point is defined formally as the point on this 'pseudo'-coexistence curve, for which the distribution function is scale-invariant. This point must therefore separate the two forms of crossover behaviour identified above. On this basis, an inspection of figures 3.6 and 3.7 shows that couplings w of 8.925 or below are subcritical while those of 9.1 or above are supercritical. Thus the majority of the points shown in figure 3.8 lie not on the coexistence curve itself, but on the continuation curve that persists in finite size systems.

3.4.4 The Critical Limit: The Function $\tilde{p}^*$

As an expediency for locating more precisely the critical point, the known form of the Ising critical universal function $\tilde{p}^*_{\mathcal{M}}$ was employed to refine the initial estimates of the critical parameters stated above. The refinement procedure anticipates fluid-magnet universality by presuming that the fixed-point distribution function of fluid matches that of the Ising model. However, the validity of this assumption can be verified *a-postiori* from consistency checks on the critical fluid critical exponents, once accurate values for the critical parameters have been determined.

In order to refine the previous estimate of the critical parameters, the following dimensionless combination of moments of the block PDF was employed [19]

$$G_L \equiv [3(< (\Delta\rho)^2 >_L)^2 - < (\Delta\rho)^4 >_L]/2(< (\Delta\rho)^2 >_L)^2, \qquad (3.35)$$

which provides a convenient numerical measure of the character of a probability distribution. Previous studies of the 2d spin-$\frac{1}{2}$ Ising model, have established that the moment ratio for $\tilde{p}^*_{\mathcal{M}}$ takes the value $G^* = 0.9145(6)$ [22]. Using this value as a target, the $\mathcal{L} = 16$ distribution functions at couplings of $w = 9.1$ and $w = 8.925$ were used in conjunction with the derivative functions (equations 3.22a and 3.22b) to predict the well-depth appropriate to the universal Ising form of the distribution function. This procedure gave an estimated critical well-depth of $w = 9.0$. When the block distribution function was duly measured at $w = 9.00$, $\mu = -2.2025$, it was found, somewhat fortuitously, to have a G_L value of 0.9147, extremely close to the universal Ising value. These parameters were therefore adopted as close estimates for the location of the critical point.

Figure 3.9 demonstrates the data collapse of the block distribution function for both the $\mathcal{L} = 16$ and $\mathcal{L} = 8$ systems onto the corresponding distribution obtained from studies of the 2d spin-$\frac{1}{2}$ Ising model at its exact critical point [22]. In both cases, the variance of the distributions have been brought into coincidence with the Ising data by a single scaling of the ordering variable. In the case of the $\mathcal{L} = 16$ system, the level of accord with the Ising model data is strikingly good although

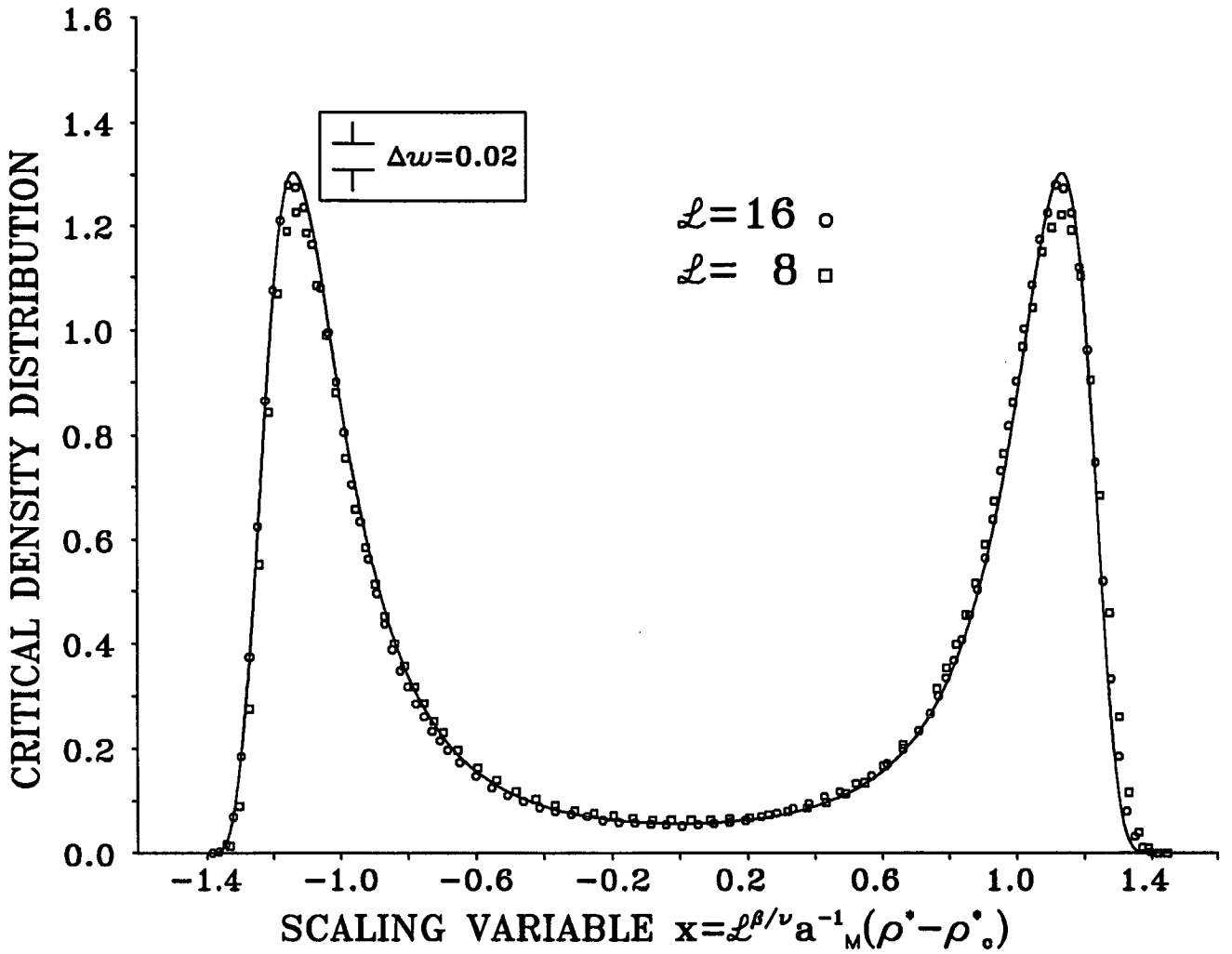

Figure 3.9: The fluid density distributions for $\mathcal{L} = 8$ and $\mathcal{L} = 16$ at criticality ($\mu_c^\star = -2.202$, $w_c = 9.00$) expressed as functions of the scaling variable $x \equiv \mathrm{L}^{\beta/\nu} a_{\mathcal{M}}{}^{-1}[\rho^\star - \rho_c^\star]$ The solid line is the fixed point function $\tilde{p}_M^\star(x)$ appropriate for the Ising universality class [22]. The non-universal scale factor $a_{\mathcal{M}}$ is chosen so that, for $\mathcal{L} = 16$, the scaling variable x has unit variance, consistent with the conventions implicit in the definition of $\tilde{p}_M^\star(x)$. The value of β/ν implicit in the horizontal scale is $\beta/\nu = 0.125$[1]. The inset shows the size of the change in height of the $\mathcal{L} = 16$ distribution peaks resulting from a change $\delta w = 0.02$ along the line of pseudo-coexistence.

this is not altogether unexpected, given that the extent of the agreement is a *motivation* for the choice of the critical coupling, rather than further corroboration. Nevertheless, the fact that it is possible at all, provides clear evidence in support of fluid-magnet universality. In the $\mathcal{L} = 8$ system, the agreement is also substantial, although not quite as impressive as for the larger system. In view of the rather small system size, it seems reasonable to attribute the discrepancy in the $\mathcal{L} = 8$ system to corrections to scaling, implying that this block-size does not quite afford full access to the universal regime. Indeed, the form of the discrepancy is remarkably similar to that which has been shown to arise from corrections to scaling in another member of the Ising universality class, the 2d ϕ^4 model [22]. It will be seen however, that the distributions also contain further structure of a much more significant form.

The consistency of this picture is further supported by the measured values of the exponent ratios β/ν, γ/ν and $1/\nu$, which feature in equations (3.20), (3.32) and (3.26) respectively. The determination of β/ν and γ/ν is described below. The ratio $1/\nu$ is addressed in the next subsection.

The exponent ratio β/ν relates to the rate at which the block-variable scale is eroded with increasing block size. Inspection of equation (3.20) reveals that the block-variable must be rescaled by a factor $a_{\mathcal{M}}{}^{-1}L^{\beta/\nu}$ in order to map the critical fluid density distribution onto the critical Ising magnetisation distribution. The relative rescaling for the two system sizes $\mathcal{L} = 8$ and $\mathcal{L} = 16$ is therefore $0.5^{\beta/\nu}$. A comparison of the scale factors required to bring the variance of both the $\mathcal{L} = 8$ and $\mathcal{L} = 16$ distributions into coincidence with that of the Ising distribution (figure 3.9) therefore provides a measure of the ratio β/ν. The measured scale-factor ratio required to effect the mapping is 0.9171, which in turn implies β/ν=0.125(1). Despite the discrepancies between the $\mathcal{L} = 8$ distribution and the universal Ising form, this value is in extremely close accord with the exact result $\beta/\nu = 1/8$ for the 2d Ising model.

The exponent ratio γ/ν relates to the finite-size scaling properties of the compressibility at the critical point. Figure 3.10 shows the compressibility measurements

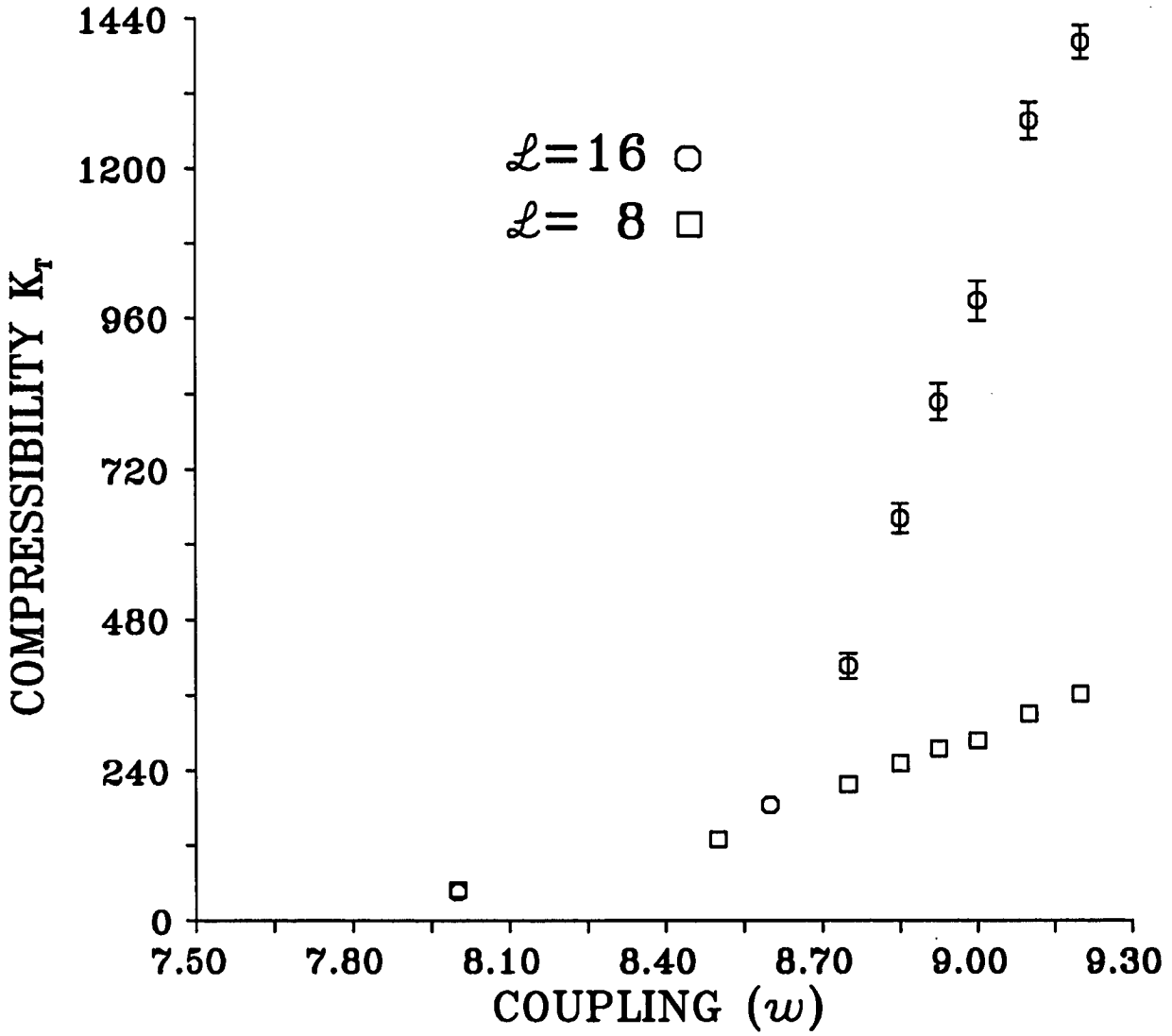

Figure 3.10: Measurements of the compressibility K_T for values of the coupling parameter w along the line of pseudo-coexistence, i.e. with μ tuned to satisfy the equal heights criterion. The compressibilities were calculated from the density fluctuations according to equation 3.32.

(c.f. equation 3.30) as a function of the well-depth, for points along the coexistence curve and its finite-size continuation. The error bars associated with these measurements are quite large because the compressibility is highly sensitivity to small departures from coexistence. The main qualitative feature of the two data sets is the strong influence of finite size effects. As the critical point is approached along the continuation curve, the compressibility of the larger system rises very much more rapidly and attains a considerably greater maximum value than in the smaller system. This observation (which is in accordance with equation 3.32) reflects the fact that a larger system can accommodate correspondingly larger fluctuations than a smaller system. The singularity pertaining to the thermodynamic limit is therefore smeared out substantially less in the larger system.

The compressibility measurements at the assigned values of the critical parameters were used to calculate the exponent ratio γ/ν. From equation (3.32) one finds that at criticality $K(\mathcal{L}=8)/K(\mathcal{L}=16) = 0.5^{\gamma/\nu}$. The measured critical compressibilities imply a value of $\gamma/\nu = 1.77(4)$ which compares favourably with the exact result of $\gamma/\nu = 1.75$ for the 2d Ising model.

To conclude this subsection, the assignments of the critical parameters are summarised together with their error bounds. In accordance with established convention, the critical temperature $T_c^\star$ has been quoted, where $T_c^\star \equiv 4/w_c$. The reduced chemical potential was defined in equation (3.33). The quoted value of $\rho_c^\star$ (defined in equation 3.34) represents both the mean and median of the critical density distribution.

$$T_c^\star = 0.44 \pm 0.005 \qquad \mu_c^\star = -2.20 \pm 0.04 \qquad \rho_c^\star = 0.368 \pm 0.003 \tag{3.36}$$

A discussion of these values (and their errors) features in the concluding section.

3.4.5 Deviations from Criticality

As previously noted, the form of the block distribution function in the near-critical region is controlled by the derivatives of the *critical* distribution function with respect to the model parameters w and μ. For large block-size $\mathcal{L}$ and large correlation length, the combination of derivative functions described by the scaling relation (equation 3.26) is expected to be universal. To expose the properties of this relation it is useful to consider the symmetries of the individual constituent terms appearing therein.

The right hand side of equation (3.26) consists of two terms, each having distinct symmetries: the asymptotically dominant function $\mathrm{r}[\rho - \rho_c]$ is trivially *odd* in the scaling variable, while a consideration of the Ising case shows that the universal function $\tilde{p}_{\mathcal{M}}^{(0,1)}$ is *even* in the scaling variable [22]. The form of the measured energy function $< u(\rho) > - < u >$ which appears on the left hand side of equation (3.26) is shown in figure 3.11 for both the $\mathcal{L} = 8$ and $\mathcal{L} = 16$ systems; its symmetry is neither odd nor even.

The symmetries of the respective terms appearing in equation (3.26) can be exploited to permit a calculation of the mixing parameter r and to expose the anticipated universality. The value of r, can be determined by ***antisymmetrising*** the function $< u(\rho) > - < u >$ about $\rho = \rho_c$. From this procedure, one finds $r = -0.529(2)$, which agrees extremely well with the measured slope of the coexistence curve. In a similar vein, the claim regarding the universality of equation (3.26) can be tested by ***symmetrising*** the function $< u(\rho) > - < u >$. The results for the even (sub-dominant) component of the energy function are expressed in figure 3.12 for both system sizes. The smooth curve represents the measured function $\tilde{p}_{\mathcal{M}}^{(0,1)}$ established in earlier studies of the 2d spin-$\frac{1}{2}$ Ising model [22]. The data points correspond to the symmetrised energy function u^s defined by

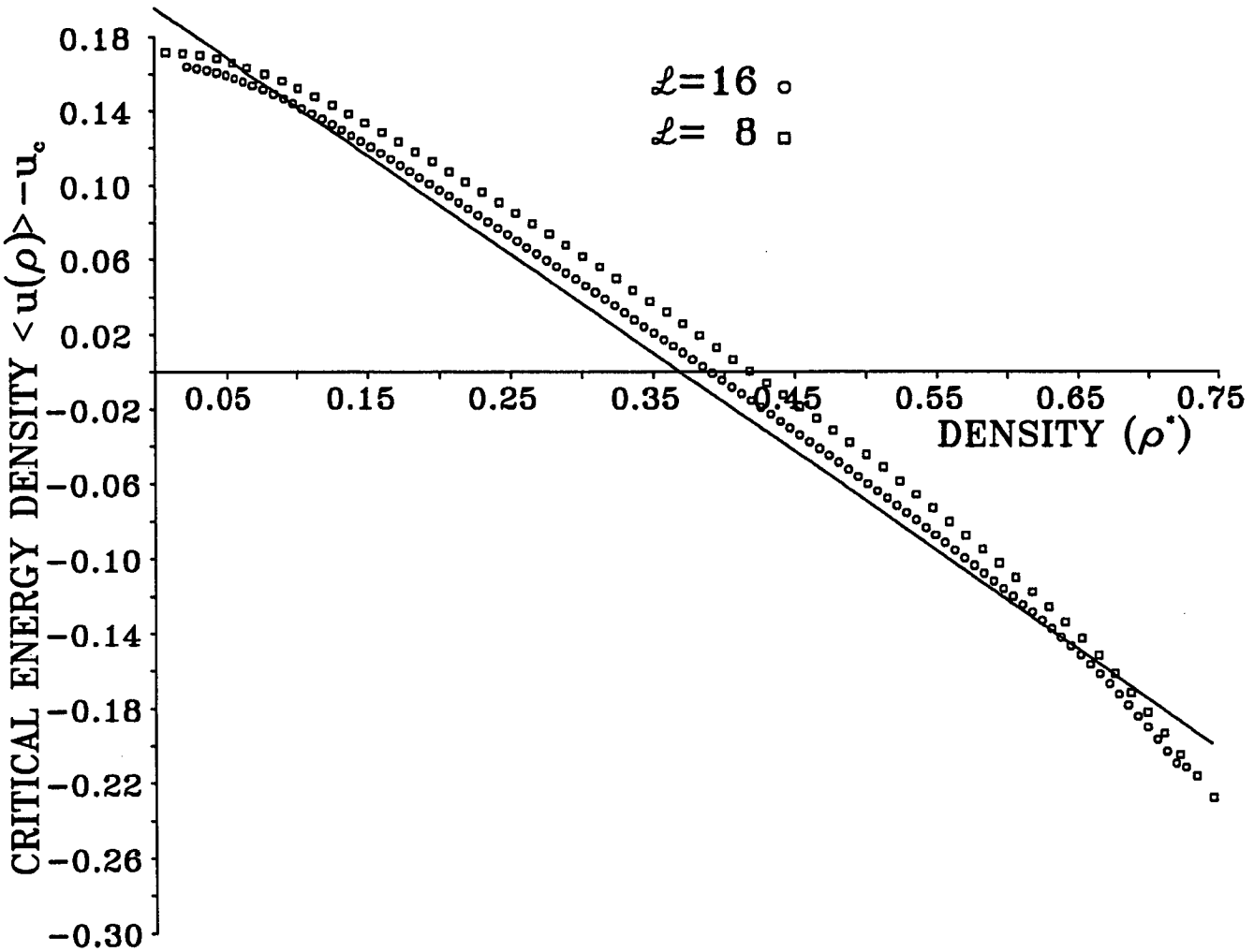

Figure 3.11: The fluid energy density for $\mathcal{L} = 8$ and $\mathcal{L} = 16$ at criticality. The solid line (cf equation 3.26) is of the form $-r[\rho^* - \rho_c^*]$ where, from the measured slope of the pseudo-coexistence curve (figure 3.2) $r = -0.529$[2]

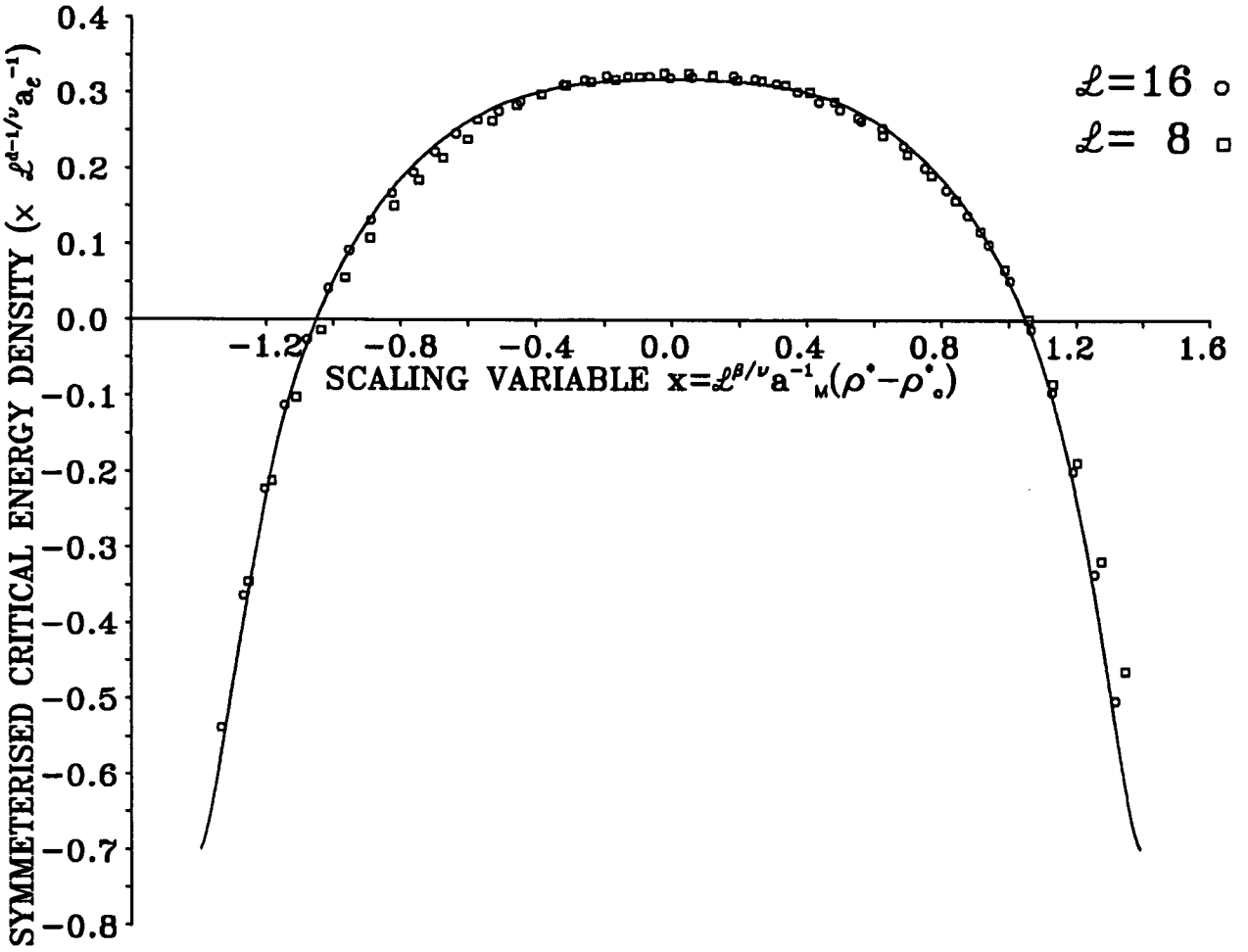

Figure 3.12: The critical fluid energy density for $\mathcal{L} = 8$ and $\mathcal{L} = 16$, symmeterised about $\rho_c^\star$ to expose the contribution *even* in $\rho^\star - \rho_c^\star$, and multiplied by a scale factor $\mathcal{L}^{d-1/\nu}a_\mathcal{E}{}^{-1}$ (cf equation 3.26) to effect comparison with the function $\tilde{p}_\mathcal{M}^{(0,1)}$ appropriate to the Ising universality class [22]. The latter is shown as the solid line. The horizontal scale is identical to that featuring in figure 3.9. The non-universal scale factor $a_\mathcal{E}$ has been chosen so that the $\mathcal{L} = 16$ data and the Ising form match at $x = 0$. The value of $1/\nu$ implicit in the vertical scale is $1/\nu = 1.03[3]$

$$u^s(<\rho>\pm\Delta\rho) = (2a_\varepsilon)^{-1}\mathcal{L}^{d-1/\nu} < \{u(<\rho>+\Delta\rho)+u(<\rho>-\Delta\rho)-2u(\rho)\} > \quad (3.37)$$

which represents the 'even' part of the left hand side of equation 3.26, with u_c and ρ_c replaced by their finite-size equivalent forms. This is one way of coping with 'corrections' to equation (3.26); it has the merit that, in this amended form, equation (3.26) satisfies the sum rule that follows with integration on ρ.

Clearly the data collapse (figure 3.12) onto the Ising curve is substantial for both system sizes, especially the larger. Moreover, the data can be used to calculate the exponent $1/\nu$. From equation (3.26), the relative amplitude of the symmeterised fluid energy function in both system sizes is $0.5^{1/\nu}$. The optimal data collapse of the symmeterised fluid energy functions onto the Ising data was obtained with an amplitude ratio of 0.49(2) implying $1/\nu$=1.03(3), compared with the exact Ising result $\nu = 1$. While the agreement as regards the exponent is satisfactory (although no allowances were made for corrections to scaling), the level of correspondence of the *scaling function* (as in figure 3.9) provides substantially more compelling evidence in favour of fluid-magnet universality.

3.4.6 Antisymmetric Corrections to the Limiting Form

In section 3.3 it was proposed that the mixed character of the scaling fields (specifically the presence of the chemical potential in the thermal scaling field τ (equation 3.7)) manifests itself as an antisymmetric correction to the limiting scale-invariant form of the critical density distribution. Moreover it was predicted that the form of this correction is prescribed by independently determined functions characteristic of the Ising universality class.

The correction, should it exist, must manifest itself in the differences between the measured density distributions and the limiting Ising form (c.f. figure 3.9). In fact there are no less than four sources for such discrepancies. Small differences

between the assigned and true values of w_c and μ_c, account for two of these, giving rise to two relevant corrections, associated with small values of h and τ . The third source of discrepancies is the leading correction to scaling associated with the irrelevant eigenvector of the Ising fixed point. Lastly, there is the correction arising from scaling-field-mixing itself, identified in equation (3.29). Although an identification of the field-mixing component amidst the other corrections might seem an unlikely proposition, there are a number of reasons why it does actually prove possible.

The first reason is the *symmetry* of the correction (3.29), which is *odd* in $\rho - \rho_c$. The odd contributions to the measured density distribution can thus be isolated by antisymmeterising the distribution about its median point. This procedure eliminates the corrections associated with the leading irrelevant correction to scaling and the contribution $\tilde{p}_{\mathcal{M}}^{(0,1)}$associated with the thermal scaling field τ , both of which are even functions.

The second reason is that the functional forms of the two antisymmetric corrections are independently known. The correction due to a non-zero h is specified by the function $\tilde{p}_{\mathcal{M}}^{(1,0)}$ (equation 3.24a), while that due to field-mixing is prescribed in equation (3.29). The functions, both of which have been determined from studies of the 2d Ising model [22], are shown in figure 3.13; their forms are clearly quite distinct. Now, consideration of these functions shows that the measured distribution must have contributions from both of these sources since mutual cancel must occur in order to satisfy the equal-peak-height criterion which was used to locate the coexistence curve and criticality. To isolate the field-mixing component, it is therefore necessary to identify the antisymmetric contribution to the measured distribution, and then remove from it the contribution due a small deviation from coexistence. The results of applying this procedure to the measured density distributions (figure 3.9) are shown in figure 3.14 for the $\mathcal{L} = 16$ systems. The correction made to account for departures from coexistence corresponds to a shift in the assigned μ_c by an amount -0.00013. This shift is small compared with the uncertainties (described below) associated with the location of the critical point *along* the coexistence curve. The agreement with the predicted form is excellent,

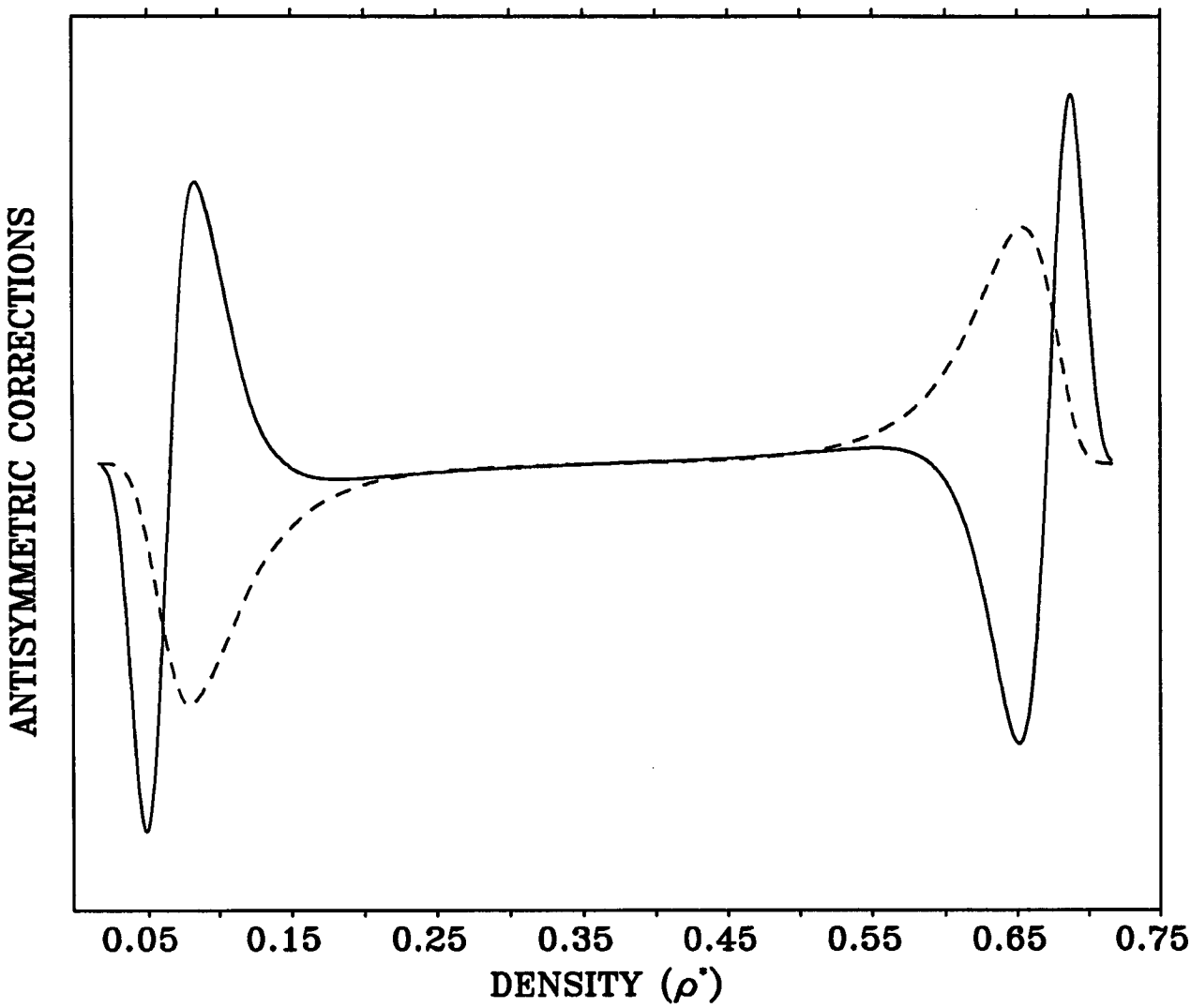

Figure 3.13: The structure of the two antisymmetric corrections to the near-critical density distribution. The solid line shows the form arising from the field-mixing (equation 3.29). The dashed line shows the form associated with a small non-zero ordering field h (equation 3.24a).

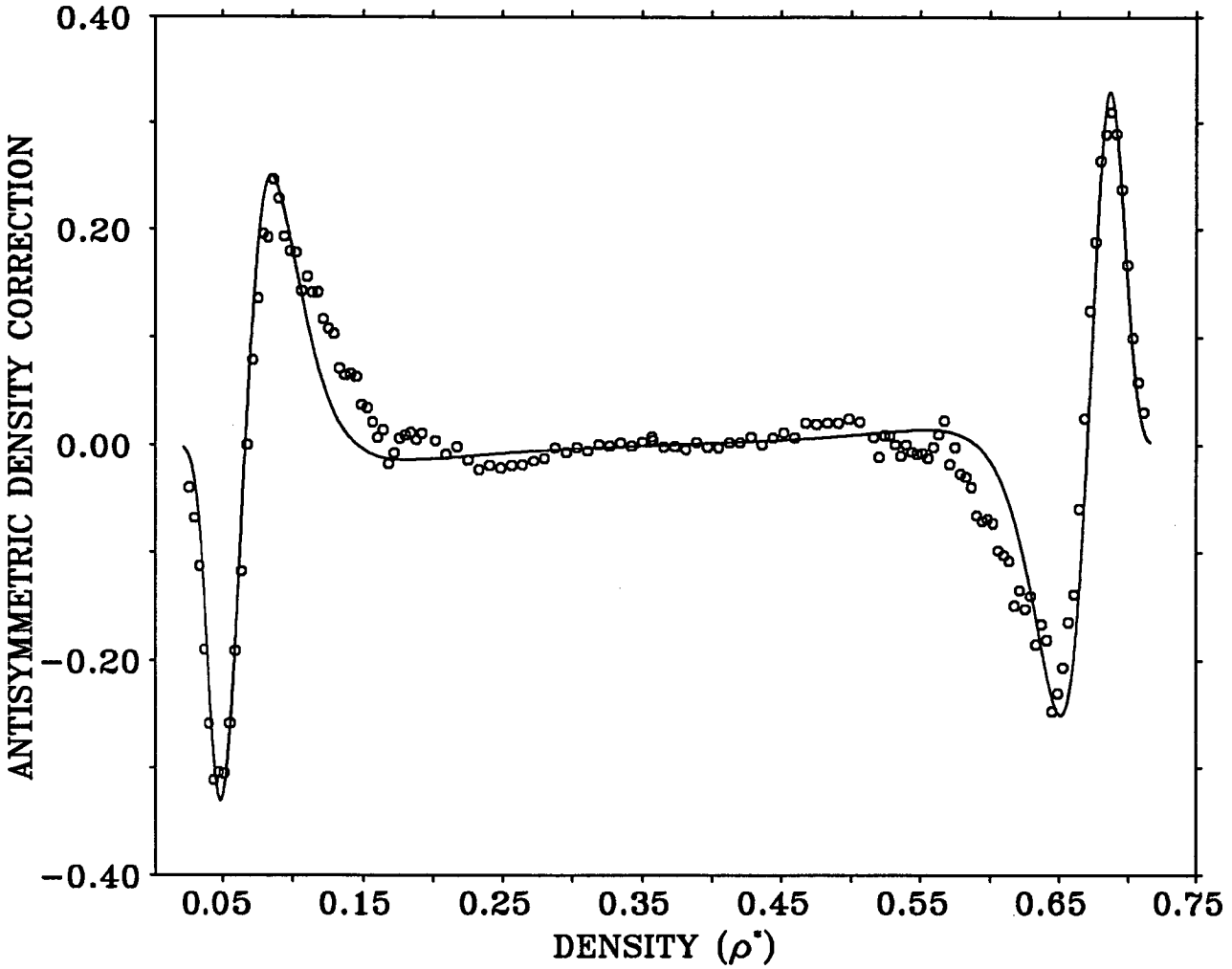

Figure 3.14: The measured antisymmetric correction to the $\mathcal{L} = 16$ distribution (figure 3.9), itself corrected for a small off-coexistence contribution, as described in the text, and shown as the data points; the solid curve represents the prediction following from equation 3.29, utilising predetermined Ising forms [22].

providing substantial corroboration of the mixed-scaling-field theory. The scale factor required to effect this mapping implies a value $s = -0.24(3)$ for the parameter describing the degree to which the chemical potential features in the thermal field τ.

3.5 Conclusions

The work described in this chapter was motivated by the need to fill two substantial gaps in the understanding of critical behaviour in simple fluids. Firstly it was perceived that there is an inadequate appreciation of the sense and depth in which the critical fluid resembles the critical magnet. This issue was addressed via a study of the probability distribution of the coarse grained density variable. The results (expressed in figure 3.9) convincingly demonstrate the configurational correspondence between the density fluctuations of the critical fluid and the magnetisation fluctuations in the Ising model. This correspondence represents possibly the single most exacting test of the universality hypothesis and provides corroboration of fluid-magnet universality that transcends critical exponent values.

Secondly, it appears that heretofore, relatively little attention has been paid to the physical nature of the relevant scaling fields in fluids, the form of which represents one (non-universal) respect in which the critical fluid differs from the critical magnet. Although it has long been appreciated that these scaling fields should comprise mixtures of the simple scaling fields featuring in systems of the Ising symmetry, the generalised finite-size scaling theory advanced in this work, shows that this mixing is manifest in the interplay of the energy and density fluctuations near criticality. The results presented in figure 3.12, bear out one aspect of this theory, namely the manner in which the temperature features in the ordering scaling field h . The other, more significant aspect of field mixing (the fact that the chemical potential features in the thermal field τ), is predicted by the scaling theory to contribute an antisymmetric (odd) energy-like correction to the limiting form of the critical density distribution. The existence of this form of mixing is

strikingly demonstrated in the results of figure 3.14. Experiments have found it difficult to demonstrate this mixing through the weak non-analytic behaviour of the rectilinear diameter. Computer simulation therefore provides an alternative and potentially much more powerful method for studying field mixing in critical fluids.

Turning now to the computational aspects of simulating near-critical fluids, it has been demonstrated that the finite-size-scaling methods that were employed so successfully for studies of criticality in magnets, can (albeit with vastly greater computational effort), be generalised to permit detailed study of critical phenomena in fluid systems. The successes of this investigation attest to the power of finite-size scaling techniques when coupled with large-scale computing resources. Indeed, the present work has proved materially much more successful than its predecessors. This is evident from a consideration of the errors associated with assignments of critical point parameters: the uncertainties assigned in equation (3.36) represent a significant improvement on the error bounds cited by previous workers (at least, those who cite *any*!). Moreover, the uncertainties quoted in equation (3.36) are rather conservative. Their range extends to the two coupling values ($u = 9.1$ and $u = 8.925$) on either side of the designated critical value (cf figures 3.6 and 3.7) which are certainly sub- and super-critical respectively. If it were to be *assumed* that finite-size corrections die out with $\mathcal{L}$ at the rate suggested by comparison of the $\mathcal{L} = 8$ and $\mathcal{L} = 16$ 'critical' data, the requirement that the $\mathcal{L} = 16$ distribution should match the Ising form provides substantially tighter bounds on the critical parameters. This point is conveyed by the inset in figure 3.9 which shows the sensitivity of the peak-height of the measured $\mathcal{L} = 16$ distribution to a change in the coupling w of $\mid \Delta w \mid = 0.02$ corresponding (cf the units introduced in equation 3.36) to a change of only $\Delta T = 0.001$ along the line of pseudo-coexistence (ie with $\mu^\star$ also changed so as to maintain the equal-height criterion).

Most previous computer studies of the critical region seem not to have appreciated the scale and character of finite-size effects which are demonstrated so graphically in the present work. In general, previous workers have obtained estimates of the critical temperature and exponents by extrapolating power-laws for the order pa-

rameter and correlation length. However, in a simulation, these quantities are necessarily finite-size limited and represent only a fragment of the data potentially available. Only rough estimates of the critical parameters can therefore be obtained in this manner. This point is illustrated in figures 3.6 and 3.7 which demonstrate that the point at which the coexisting phases coalesce in a finite-size system can represents a serious *over-estimate* of the critical temperature, especially in 2-dimensions. This observation has also been made recently by Mon and Binder [65] in a critique of Monte Carlo studies of phase coexistence using the Gibbs ensemble.

In view of the foregoing remarks, is not too surprising that comparisons among the previous computer studies of the 2d Lennard-Jones system, reveal large disparities regarding the assignments of the critical temperature. Thus, for example, using the same units as those employed in equation (3.36), Tsien and Valleau [66] suggest $T_c^\star$ between 0.625 and 0.7, Henderson [67] gives $T_c^\star = 0.56$, Barker et al [56] quote $T_c^\star = 0.52$, Rovere et al [60] suggest $T_c^\star = 0.50 \pm 0.02$ while Singh et al [68] quote $T_c^\star = 0.472$. Comparisons amongst these assignments, and with the estimate of this work (equation 3.36) are complicated by differences in the value assigned to the Lennard-Jones cutoff. The extent of the consequences of the different cutoff assignments has been estimated by utilising the values of the 2nd Virial coefficient to give the associated van der Waals transition temperature. Making the approximation that the fractional change in the true critical temperature (arising from a change in the cutoff) matches the fractional change in the van der Waals transition temperature, it transpires, for example, that the difference between the cutoff ($r_c = 2.5\sigma$) employed by Rovere et al [60] and that of the present work ($r_c = 2\sigma$), accounts for approximately $\frac{1}{3}$ of the difference between the assignments the critical temperature. Thus it would seem that virtually all previous studies have significantly overestimated the critical temperature, presumably because (as discussed above) it is all too easy to mistake the finite-size continuation of the coexistence curve for the real thing.

Finally, with regard to the prospects for refining and extending the work described here, it should be noted that the largest system size studied (containing of order

400 particles), approaches the limits of what is feasible using modern computer technology. In fact the present study consumed well over 5×10^3 hours computer time, even with state-of-the-art parallel computers. One difficulty encountered was that the acceptance rate for particle insertions and deletions in the grand canonical ensemble decreases rapidly as a function of increasing density. This problem was found to be particularly acute in the two-phase region. Close to criticality, however, the low acceptance rate was compounded by critical slowing down, which dictated enormously long equilibration and sampling times. Although growing computational power will go some way to alleviating these problems, it is clear that algorithmic acceleration techniques are desirable and necessary if significantly larger and more complex systems are to be studied. One method for improving the acceptance rate of dense systems in the grand canonical ensemble has been suggested [69], although it appears to satisfy detailed balance only approximately.

In response to the difficulties encountered, alternative algorithms for studying near-critical fluid have been sought. Recently developed collective (cluster) updating schemes have dramatically improved the problem of critical-slowing-down in lattice-based spin systems. However, no generalisation of lattice-based cluster updating methods to off-lattice problems has yet been reported. The feasibility of applying cluster updating ideas to fluids has therefore been considered. This study and its conclusions form the subject of the following addendum to this chapter.

3.6 Addendum: Collective Coordinate Updating

3.6.1 Background

The most serious problem hindering traditional Monte Carlo studies of criticality, is the phenomenon of critical-slowing-down (CSD). This phenomenon occurs principally when implementing 'local' updating schemes where the constituents of a system (spins or particles) are updated individually. The origin of CSD can be traced to the critical divergence of the correlation length. Intuitively it is clear that in a single step of a local algorithm, information about the state of a spin propagates only as far as its nearest neighbours. Now, in order to attain a truly independent configuration, this information must propagate a distance of order the correlation length ξ. However, due to the stochastic nature of the local update scheme, the information executes a random walk through the system. Consequently, one expects that the auto-correlation time should behave like $\tau \sim \xi^2$. More generally, one finds $\tau \sim \xi^z$ where z is known as a dynamic critical exponent. Computer simulations measure $z \approx 2.125$ for Ising models using local updating schemes.

Although the correlation time τ is necessarily bounded for a finite system, it can become very large for large simulations ($\tau \sim L^z$). As a result, the rate of phase space exploration can become extremely slow, necessitating considerable computational effort to generate independent configurations. For many years, CSD represented the limiting factor governing the size of simulations of the critical region. A welcome improvement to this state of affairs (at least in the context of spin systems) came with the introduction by Swendsen and Wang of cluster updating (CU) methods [70]. These methods greatly reduce or even eliminate CSD by adopting a *global* rather than a local updating scheme [71]. This is achieved by identifying clusters of connected spins (of the same spin value) which can be updated as a *whole*. Since clusters range in size up to the correlation length,

the CU method has the potential to generate radically different configurations in a single step.

The primary requisite when defining a cluster, is that the constituent spins should be strongly coupled to each other, but only weakly coupled to the cluster environment. In other words, the boundary of the cluster should be an energetically favourable energy surface, thereby ensuring an acceptably large cluster flip probability. In this sense therefore, the structure of clusters realised by the algorithm should conform to the intuitive perception of a cluster as being a physically well-connected collection of like spins.

The first CU method was formulated in terms of the q-state Pott model [70], but similar techniques were soon developed to deal with other more complex spin systems such as O(n) models [72]. Although various specific realisations of CU schemes exist, the strategy most frequently employed for spin models is a two-step process that can be summarised as follows:

1. Beginning with an arbitrary configuration of spin states, one attempts to create 'satisfied bonds' between all pairs of interacting sites i and j having the same spin type. Satisfied bonds are assigned according to some probability q_{ij}. No bonds are formed between unlike spins. At the end of the procedure, all spins connected by some path of satisfied bonds are deemed to be members of the same cluster.

2. A new value is assigned to the spins comprising each cluster according to some probability $\mathrm{p}(V_c)$, where V_c is the cluster 'potential'. The *same* new spin value is assigned to *all* the spins in the cluster.

In general, the cluster potential V_c, determining the update probability, will depend on the interactions between the spins comprising a given cluster and those bordering on it. The strength of the coupling between the cluster and its environment is crucial in determining the ease with which clusters can be updated. This coupling is mediated by the choice of the bond-assignment probability q_{ij}. For

certain types of spin interactions it is possible to choose q_{ij} such that the clusters effectively decouple from one another. This is the situation realised by the SW algorithm for the Potts model, whose choice of $q_{ij} = 1 - \exp(-J)$ implies that no inter-cluster interactions appear in the detailed balance calculations. Under such conditions *all* clusters can be updated simultaneously. Using the SW method the dynamical exponent is found to be $z = 0.35$, a significant improvement on the value of $z = 2.125$ appropriate to conventional single-site updating.

In general, clusters do interact with one another and must therefore be updated sequentially, taking due account of their interactions with other clusters [73]. In fact there are often advantages in updating clusters singly even when it is possible to produce a decoupled cluster configuration. This was shown by Wolff in the context of O(n) models [72]. His technique seeks to locate the cluster associated with a randomly chosen site on the lattice. Since this site has the highest probability of belonging to the largest cluster, the method directs the computational effort at that cluster which (when flipped), produces the most radically different configuration. Compared to the SW algorithm, the Wolff method expends proportionally much less computational effort on smaller clusters. When applied to the Ising model, the Wolff algorithm actually appears to suffer less from CSD than does the original SW algorithm.

In more recent developments, CU methods have been successfully extended to deal with the ϕ^4 model [74]. The technique in this case involves the decomposition of the ϕ^4 spin ordering variable into a combination of an Ising-like variable and a displacement variable. The Ising-like spins are updated according to the method outlined above while a separate single-site method is used to update the displacement terms.

In view of the seemingly disparate nature of the various CU scheme, some attempts have been made to unify existing CU techniques within a single framework. While some success has been had in the context of lattice-based spin systems [75], the generalisations do not yet extend to systems displaying particle-hole asymmetry. In the remainder of this section, an outline is given of the specific difficulties

associated with the application of existing CU techniques to the fluid problem.

3.6.2 Cluster Updating and Fluids

From the point of view of cluster formation, the most obvious drawback of fluids is the lack of symmetry of the Hamiltonian with respect to positive and negative values of the (reduced) ordering field. This lack of particle-hole symmetry means that unlike, for instance, the Ising model which has two types of correlated order, corresponding to clusters of 'up' and 'down' spins, the fluid possesses only particle clusters. Thus while one may obviously 'flip' the occupancy of clusters of particles causing them to be removed from the system, it is not immediately obvious that one can perform a complementary operation by creating clusters of real particles from the void. This is the first obstacle which must be overcome when devising a cluster updating algorithm for fluids.

One solution to the problem posed by particle-hole asymmetry is to populate with 'ghost' particles, those regions of the system that contain no real particles. These ghost particles have no interactions either with other ghost particles or with real particles; they are merely artifacts designed to restore a measure of symmetry to the system. The aim is then to try to form clusters from the ghost-particles, and to transform them into clusters of real particles. Of course, clusters of ghost particles should be chosen such that they yield an energetically favourable cluster of real (interacting!) particles once flipped. When seeking to identify ghost clusters, one therefore assumes an interaction potential between the ghost particles (and between ghost particles and real particles) of the same form as that existing between real particles. It should be emphasised however, that this interaction is solely for the purpose of identifying clusters; ghost particles have no physical interactions.

When studying a system comprising both real and ghost particles, it is necessary that the number of ghost particles be sufficiently large to ensure ergodicity. In other words, there must be sufficient ghost particles such that if all were trans-

formed into real particles, the particle density would be as large as one might ever reasonably expect to realise for given values of the model parameters. In the case of the Lennard-Jones fluid, this can be achieved by partitioning the system into square cells, the linear extent of which is of order the hard-core radius (c.f. figure 3.1). Each cell is permitted to contain one ghost particle or one real particle.

The most common method for forming clusters in spin systems is the 'bond' method. At first sight, this method can be straightforwardly applied to the fluid system with ghost particles. Pairs of particles of the same occupancy type (real or ghost) are considered in turn and a satisfied bond is formed between them according to some probability q_{ij} which depends on their interaction energy. When all interactions have been considered, particles that are connected to other particles by some path of satisfied bonds, are deemed to be members of the same cluster. Although the bond method works perfectly satisfactorily for spin systems, it will be shown that when applied to the fluid problem, it fails to produce energetically favourable clusters.

For the truncated LJ potential, a reasonable choice of the bond-assignment probability is

$$q_{ij} = 1 - \exp\left(\frac{1}{2}\phi_{ij}\Theta(-\phi_{ij})\right), \tag{3.38}$$

where ϕ_{ij} is the LJ interaction potential and $\Theta(-\phi_{ij})$ is a unit step function inserted to ensure that probabilities never exceed unity. For this choice of q_{ij}, one can show that detailed balance is satisfied if the cluster update probabilities are drawn from the distribution:

$$p(n) = Z^{-1}\exp(-V_c(n)) \tag{3.39}$$

where

$$Z = \sum_n \exp(-V_c(n)), \qquad n = 0, 1 \tag{3.40}$$

and

$$V_c = -n\{N_c\mu - \frac{1}{2}\sum_{i\in c}\sum_{j}\phi_{ij} + \frac{1}{2}\sum_{i\in c}\sum_{j\ni c}\phi_{ij}(\Theta(-\phi_{ij}) - 1)(\delta_{n_j1} - \delta_{n_j0})\} \quad (3.41)$$

Here N_c is the number of particles in a given cluster, μ is the chemical potential, and the occupancy variable takes the value $n = 1$ for real particles and $n = 0$ for ghost particles.

Now, under typical conditions of temperature and chemical potential, real particles are separated by distances of order the well-minimum position ($\sim 1.13\sigma$). However, to ensure ergodicity, the cell size must be of order the hard-core radius ($\sim 0.8\sigma$). Clearly therefore, for moderate (real) particle densities, many more cells will contain ghost particles than contain real particles and consequently many ghost particles will occupy positions very close to their neighbours. From the point of view of the bond assignment probability, no satisfied bonds can ever be formed between such close-lying ghost particles, because their interaction energy is large and positive. However, because of the high density of ghost particles overall, and the long-distance nature of the interaction potential, it is still possible (and indeed as will be seen, highly likely) that these close-lying ghost particles will be members of the *same* cluster. The simplest example of this situation is depicted in figure 3.15. In this figure, ghost particles A, B and C are members of the same cluster because satisfied bonds link particle A to both B and C. However, ghost particles B and C lie very close to one another. Hence it is energetically extremely unfavourable to flip this cluster because the interaction energy between real particles placed at positions B and C would be large and positive.

The manner in which this problem translates to the wider context of the system as a whole is illustrated in figure 3.16. Although perfectly acceptable clusters of real particles are formed, all the ghost-particles are seen to be members of a single percolating cluster. This latter cluster can never be flipped because the energy of the resulting real-particle cluster would be extremely high. Even if it could be flipped, the move would be trivial in terms of phase-space exploration. Thus it is clear that when applied to systems that lack particle-hole symmetry, cluster formation by the bond method fails in its basic aim: ghost clusters are formed

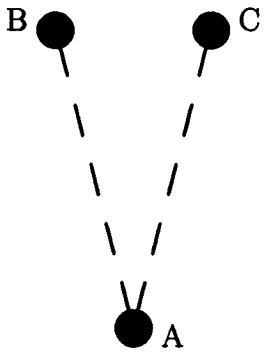

Figure 3.15: A cluster of ghost particles generated using the bond method. Ghost particle A is linked to B and C by satisfied bonds. No bond exists between particles B and C.

that cannot be transformed into real particles without a large energy cost.

At first sight, it would seem that the best method for circumventing these problems is to discard the bond method in favour of a cluster formation technique that *does* produce clusters having an energetically favourable energy surface. Unfortunately, this approach also appears to break down because of a failure to treat real and ghost particles on an equal footing. To illustrate this, consider the following revised cluster formation scheme.

The revised scheme entails visiting (in turn) connected particles of a given occupancy type and assigning them to the current cluster with a probability

$$q_i(n_i) = \exp(-V_i(n_i)) \tag{3.42}$$

with

$$V_i(n_i) = \sum_j \tilde{\phi}_{ij}\delta_{n_j 1}\delta_{n_i 1} + \sum_j \tilde{\phi}_{ij}\delta_{n_i 0} \tag{3.43}$$

where $\tilde{\phi} = \phi - \phi_w$ and ϕ_w is the well depth.

The chosen form of the potential V_i takes account of *all* the interactions of a given particle, not just individual pair-wise terms. It therefore ensures that the problem illustrated in figure 3.15 cannot arise. However, to achieve this, the potential treats the two types of particle differently. When forming real clusters, only interactions between real particles are considered. In contrast, when forming ghost clusters, both ghost-ghost and ghost-real interactions are considered, thereby ensuring that no ghost clusters are formed in the immediate vicinity of real clusters.

Although the revised method does indeed allow the formation of energetically favourable clusters, a large penalty must be paid for distinguishing between the two types of particle. One finds that in order to satisfy detailed balance, the cluster potential V_c appearing in the update probability $p(n)$ (equation 3.39) must contain an additional term of the form $\sum_{i \in c,j} \phi_{ij}(1 - \delta_{n_j 1})$. This term acts as an effective interaction between real-clusters and ghost particles which unfortunately prevents the flipping of most real-particle clusters.

Thus in summary, it seems that there is no straightforward generalisation to fluids of the cluster updating methods deployed so successfully for lattice models. Existing CU schemes seem to rely implicitly on particle-hole symmetry and, as demonstrated above, cannot be simply grafted onto a model fluid. Similarly, attempts to camouflage the lack of particle-hole symmetry in order to produce energetically favourable fluid clusters, must necessarily involves a method that distinguishes between the two types of particle at the cluster-formation stage. This failure to treat both real and ghost particles on an equal footing also leads to a highly inefficient CU scheme. In view of this prognosis, it must be concluded that the immediate prospects for radically reducing critical-slowing-down in fluids are not favourable.

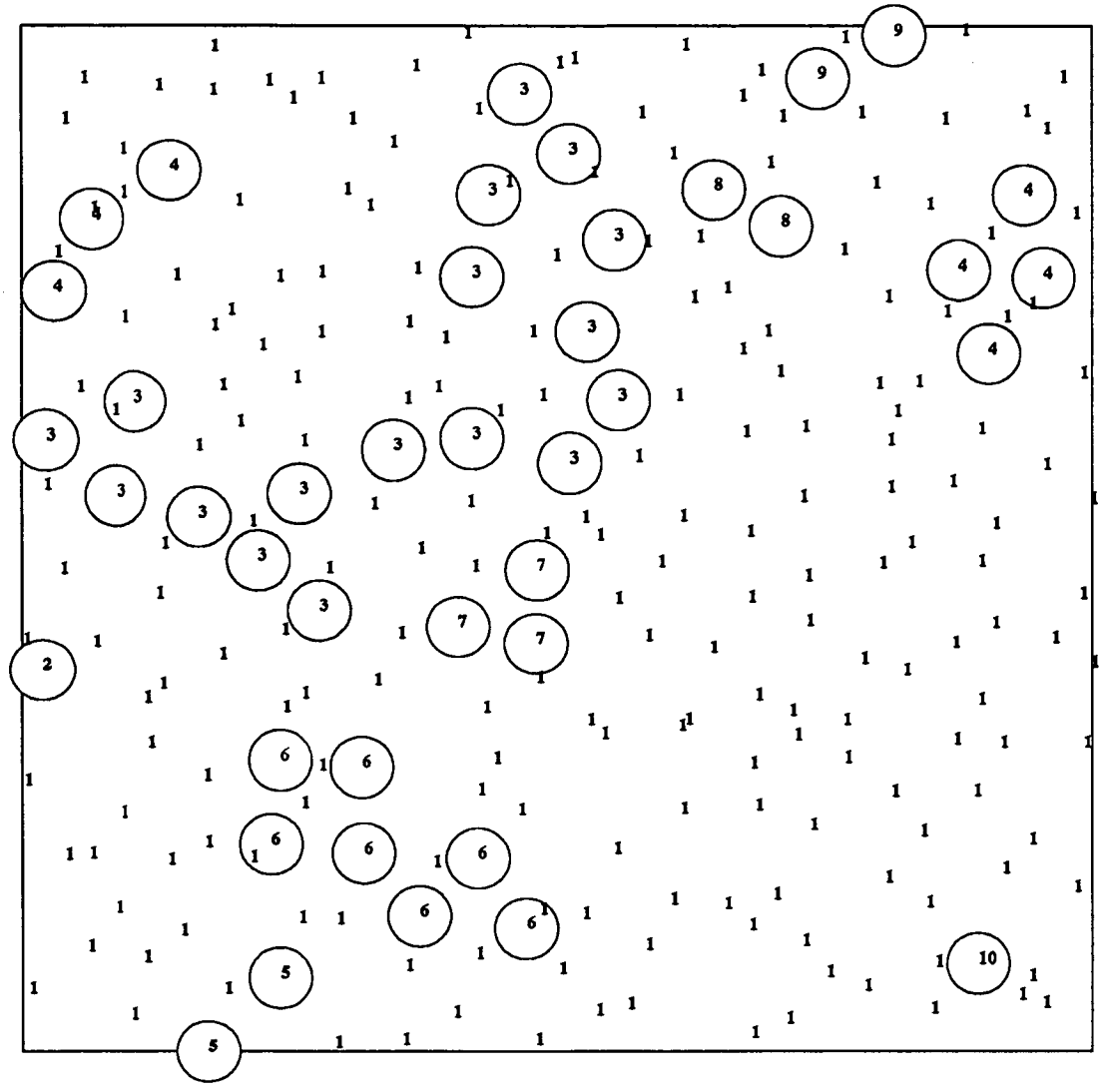

Figure 3.16: A cluster configuration generated using the 'bond' method. The circles represent real particles. The number inside each circle represents the cluster label for that particle. All particles having the same cluster label are members of the same cluster. Numbers not associated with particles represent the cluster labels of ghost particles which, in the present case, form a single percolating cluster. It can also be seen that ghost particles approach real particles arbitrarily closely.

Chapter 4

The Crystal Structures of Cyclohexane–d_{12}

4.1 Introduction

It is a feature of many organic molecular crystals that they exhibit a rich variety of phase structure in quite modest ranges of temperature and pressure. The particular structure adopted by a molecular crystal is thought to owe much to the rules of compact packing: the 'protuberances' of one molecule should fit into the 'hollows' of another. In many instances, however, the 'globular' shape of organic molecules implies that there exist several different packing arrangements for which the lattice energy is similar in magnitude. Additional factors such as dynamic disorder, molecular distortion, sample history, and isotopic substitution [76] must then be invoked to explain which of the favourable structures is actually adopted in practice. The complex interplay between these factors is believed to be responsible for the high degree of structural polymorphism exhibited by many organic molecular systems [77]. Unfortunately, the extent and manner of their influence in determining the observed structures is far from being satisfactorily understood [78].

Extreme examples of the influence of dynamic effects in determining crystallographic structure are to be found among the ranks of so-called 'plastic' crystals whose molecules enjoy a high degree of orientational freedom. For these systems,

the molecular centres lie on high-symmetry positions but the molecules undergoes rapid reorientations. Each molecule may therefore be regarded in terms of a spherical 'pseudo-molecule' the radius of which corresponds to the mean sphere of revolution of the real molecule. Accordingly, and almost without exception, the crystal structures of plastic crystals are found to be F.C.C. or B.C.C. cubic, these providing high packing densities for hard spheres.

Examples of the role played by molecular distortion and preferred bonding directions are given by materials such as cyclopentene and succinonitrile in which the molecules undergo conformational (geometric) changes and distortions at phase transitions [79, 80]. For such systems the crystal structure is determined by the result of competition between the conformation associated with the lowest *intra*-molecular (strain) energy, and that yielding the lowest *inter*-molecular (lattice) energy.

Crystallographic structure is also occasionally dependent on the thermodynamic history of the sample. Although for specified values of the temperature and pressure there can exist only one structural groundstate, it is often the case that the free-energy of other structures is similar to that of the global free-energy minimum. If further, a large energy barrier discourages transitions from these other low-lying states to the global-minimum structure, extremely long-lived metastable states can arise. For specified values of the temperature and pressure, certain thermodynamic paths may provide easier routes to the structure of minimum free-energy than others.

The lack of a thorough understanding of the processes governing the formation of any given phase means that as yet, it is not possible to predict *a priori* which crystallographic structure a given organic molecular system will adopt for prescribed values of the temperature and pressure. A clear elucidation for a simple organic system of the adopted structures, together with the conditions under which they are formed is therefore a vital step towards an understanding of the mechanisms governing structural polymorphism. To this end, a study of the solid phases of cyclohexane has been undertaken. Cyclohexane is a good candidate for such a study

because whilst being a relatively simple and compact molecule, it is also known to exhibit a wealth of phase structure. Since rather comprehensive data already exists for the ambient pressure phases of cyclohexane, the present investigation focuses primarily on the high-pressure phases which have not been previously studied in great detail. This work therefore complements earlier studies of cyclohexane and allows a more complete picture of its phase diagram to be constructed.

4.2 Background

Of the previous structural studies on cyclohexane, most have focussed on the ambient-pressure phases, which have been extensively investigated using a variety of techniques including x-ray diffraction, infra-red spectroscopy and NMR. At ambient pressure two stable solid phases of cyclohexane are known to exist. Phase I, the plastic phase, exists between 186.1 K and the melting point at 279.82 K. It is cubic (a=8.61(2)Å; Z=4; space-group Fm3m) and from NMR studies is known to be characterised by a large degree of dynamic molecular disorder, the molecules undergoing rapid reorientations on the lattice sites [81]. Below 186.1 K a first-order phase transition takes place to an orientationally ordered structure (phase II). Single crystal x-ray diffraction measurements performed by Kahn *et al* [82] have shown that phase II possesses a monoclinic unit cell (a=11.23(2), b=6.44(2), c=8.20(2)Å; β = 108.83(4)°; Z=4 and space group C2/c). In the same work, a determination of the molecular positions and atomic coordinates also revealed that the molecules are in the 'chair' conformation (which is believed to be the geometrical configuration of lowest energy [78]), but exhibit a slight though significant deviation from D_{3d} symmetry.

Cyclohexane also exhibits a metastable phase at ambient pressure. This phase was discovered by Renaud and Fourme in 1963, who found that it could be formed by quenching to approximately 100K from either the liquid or the plastic phase [83]. Their x-ray powder work showed its structure to differ from either of the other ambient pressure phases, though the poor quality of their data precluded

a structural determination. It has been speculated however, that the structure of the metastable phase is the same as that of one of the stable phases normally existing only at high pressures.

In contrast to the ambient-pressure phases, relatively little is known about the structures existing at high pressure and it is only comparatively recently that they have come under scrutiny. Previous high-pressure investigations have been carried out using differential thermal analysis (d.t.a), vibrational spectroscopy and neutron powder diffraction techniques.

D.t.a heat capacity measurements on the hydrogenated system performed by Würflinger [84], point clearly to the presence of a new structure (phase III) at pressures above 0.25 kbar. The temperature range over which this phase is stable was observed to increase with pressure. Similar d.t.a work by the same group on the *deuterated* system also indicated the existence of a further high-pressure structure (phase IV), lying intermediate between phase III and the low temperature structure [85]. Phase IV was not observed below 3 kbar in the hydrogenated system, suggesting that deuteration plays a major role in determining the region of stability of the high-pressure phases. Reproductions of the phase diagrams of Schulte and Würflinger for both C_6H_{12} and C_6D_{12} up to 3 kbar are included in figure 4.1 (a) and (b) respectively.

Ambient temperature vibrational spectroscopy measurements on both C_6H_{12} and C_6D_{12} as a function of pressure have recently been reported by Haines and Gilson [86, 87]. Using Raman and Infra-red techniques, these workers detected two phase transitions in both molecular systems. In the deuterated system, the first transition occurred at 5.3 kbar and the second occurred at 7.4 kbar. In contrast for the hydrogenated system, phase transitions were seen at 5.1 kbar and 9.6 kbar. From an analysis of the vibrational modes of both systems, the phase above the first transition (i.e. at higher pressure), was found to possess orthorhombic D_{2h} site symmetry. A similar analysis for the upper phase suggested that here the molecules possess monoclinic C_{2h} site symmetry, prompting the conclusion that the upper phase is none other than the monoclinic phase II. No clear findings

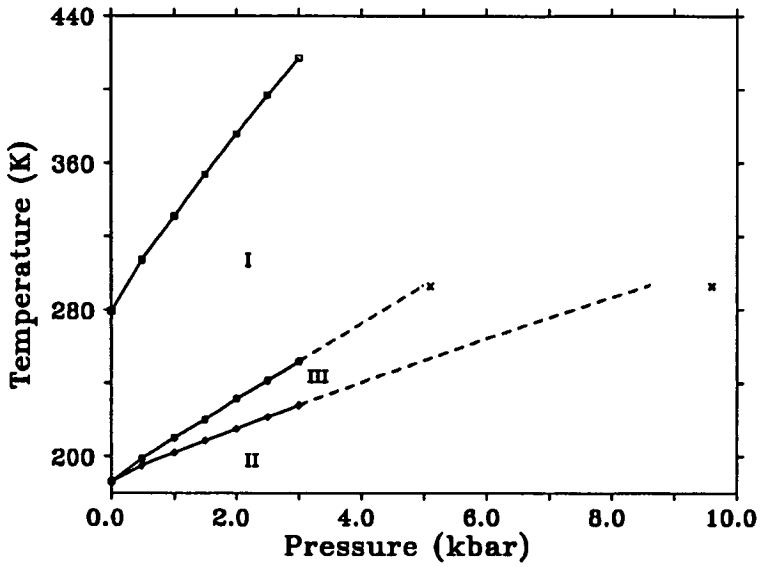

(a)

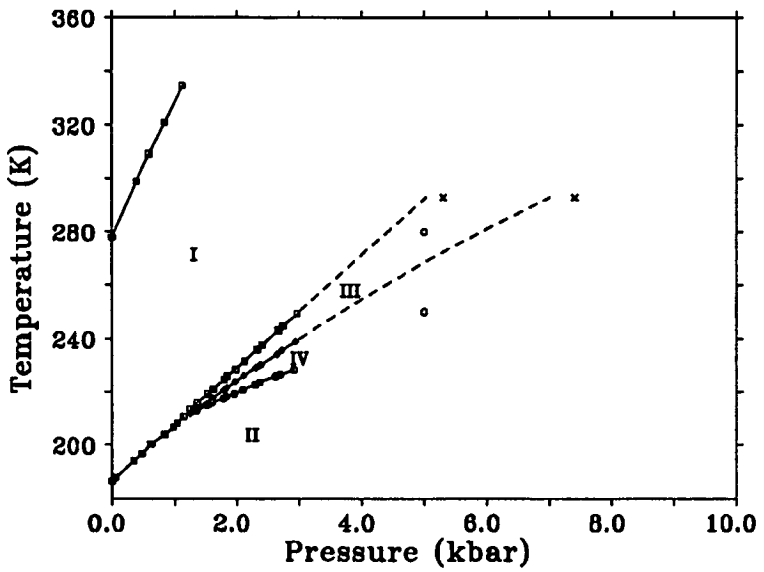

(b)

Figure 4.1: The phase diagram of Schulte & Würflinger [85] for (a) cyclohexane and (b) cyclohexane-d_{12}. The broken lines represent the extrapolation to room temperature of a polynomial fit to the d.t.a data. The points (×) at 293 K correspond to the boundary of phase III as determined by Haines & Gilson [86, 87]. The points (o) at 5 kbar, 280 K and 5 kbar 250 K correspond to the conditions under which structural determinations were performed in the present study.

relating to a transition above 7.4 kbar have been reported by Haines and Gilson, though recent and as yet unpublished Raman measurements at Edinburgh have revealed a room-temperature transition at approximately 12 kbar in the deuterated system [88]. Such a transition pressure is consistent with an (albeit large) linear extrapolation to room temperature of the phase II to phase IV boundary shown to 3 kbar in figure 4.1(b).

The d.t.a. results for phase III in both C_6D_{12} and C_6H_{12} can be seen to be consistent with those of the vibrational spectroscopy, by means of an extrapolation to 293 K of the phase diagrams of Schulte & Würflinger [85]. Using a polynomial fit based solely on the d.t.a data, the phase lines delineating phase III have been projected to room temperature (figure 4.1, broken lines). For the hydrogenated system this procedure yields transitions at approximately 5.0 kbar and 8.6 kbar, whilst for the deuterated system transitions are found at 5.1 kbar and 7.0 kbar. Evidently these estimates are in reasonable accord with the values measured by Haines & Gilson. There seems little doubt therefore that in both C_6D_{12} and C_6H_{12}, the structure existing at pressures slightly above 5 kbar at 293 K is phase III, as defined in the phase diagrams of figure 4.1.

Neutron powder diffraction studies of C_6D_{12} have been performed very recently by Mayer *et al* [89, 90] for pressures in the range 1 bar to 3.7 kbar and temperatures down to 160 K. This investigation confirmed the presence of the phases observed in the d.t.a. work and showed that the crystal structures of the various phases (I–IV) differ. Moreover, the study revealed that the high-pressure phases can exhibit a surprising degree of metastability, strongly dependent on the thermodynamic history of the sample. Thus for example it was found that phase IV (as defined in the phase diagram of figure 4.1(b)) is obtained only if the sample is first cooled to phase II, followed by the application of pressure, and finally by the raising of the temperature. Other thermodynamic paths such as the application of pressure at room temperature followed by cooling, allowed phase IV to be supercooled (relative to figure 4.1(b)) by several tens of degrees. Owing to low instrumental resolution, the quality of the diffraction data from this study was inadequate to allow a determination of the unknown crystal structures of phases III and IV.

In view of the lack of a full understanding of the effects of pressure and deuteration on the phase diagram of cyclohexane, a determination of the high-pressure structures has been performed by neutron diffraction techniques [91]. Neutron diffraction was preferred to x-ray diffraction for this study because it allows a superior resolution of the positions of Hydrogen atoms. As single crystal work at high-pressure is fraught with difficulties, a high-resolution neutron powder diffraction study was performed. Unfortunately it is not feasible to study hydrogenated cyclohexane by neutron scattering because Hydrogen (in contrast to deuterium), has an extremely large incoherent scattering cross-section for neutrons [92]. This incoherent scattering gives rise to a very high background count in the diffraction pattern which considerably complicates refinement of structural parameters. Thus it was necessary to work with a deuterated sample, C_6D_{12}, for which the incoherent scattering is much smaller.

4.3 Experiment and Structure Determination

Owing to the typically large number of overlapping reflections seen in a powder profile, access to a large-wavelength neutron source and a high-resolution diffractometer were essential to the feasibility of this study [93]. All data were collected using the high-resolution D1A and D2B angle-dispersive neutron diffractometers at the Institut Laue–Langevin (ILL) [94]. These diffractometers play somewhat complementary roles to one another.

The virtue of the D1A diffractometer is its ability to operate with a large incident neutron wavelength of 2.989 Å. This instrument is therefore suitable for unit-cell indexing of unknown phases because the individual Bragg reflections are widely spaced. Unfortunately, the large wavelength is accompanied by a paucity of Bragg peaks within the operating angle of the detectors. Furthermore the neutron flux associated with D1A is rather small and there is present in the beam, a 1% $\lambda/3$ contamination, originating from the Ge monochromator. Thus, whilst D1A is ideal for solving unit-cell parameters, the data it provides is inadequate for accurate

structural refinement.

In contrast, the D2B instrument has seven times the neutron flux of D1A and can be used in conjunction with a neutron wavelength of 1.595 Å to obtain a large number of Bragg peaks and data of high statistical quality. Data from this instrument *is* suitable for accurate structural refinement, once the basic structure has been determined using the data provided by D1A. No significant harmonic contamination is present at this smaller wavelength.

For high-pressure measurements at low temperatures, a 6 kbar helium pressure cell was employed in conjunction with a standard orange cryostat. The pressure as indicated by the calibration of the pumping apparatus was independently corroborated by a strain gauge instrument accurate to better than 0.1 kbar. Structure determination at high-pressure is unfortunately complicated by scattering from the aluminium housing of the pressure cell. At a wavelength of 2.989 Å, this gave rise to a main aluminium diffraction peak (200), centred at 94° of 2θ. The corresponding $\lambda/3$ contamination was identified at 28.5°, with further peaks at 40.8° and 79.5°. Those reflections lying in the immediate vicinity of these reflections were excluded from the set used for the unit cell indexing procedure.

A commercially available sample of C_6D_{12} with a stated deuterium purity of 99.5% was obtained from the Aldrich chemical company. The sample was introduced in liquid form to the sample holder, a 12mm diameter vanadium can. In order to ensure homogeneity of the powder, the sample can was packed with silica wool prior to introduction of the sample. In this way, no single crystals of significant size can be formed on cooling. The effect of the silica wool on the powder patterns is known to be negligible, adding uniformly to the background [95].

At a pressure of 5 kbar, scans were collected at temperatures of 280 K, 250 K and 175 K. The temperature was then fixed at 175 K, while the pressure was reduced in successive steps to 3 kbar, 2 kbar, 1 kbar and finally to 1 bar. The constant pressure powder patterns are presented in figure 4.2, while those at constant temperature are given in figure 4.3. In the interests of clarity these patterns have

been truncated to show only the portions between 30° and 90° of 2θ.

4.3.1 Phase III : The Orthorhombic Phase.

Initially a short run was performed at 5 kbar, 300 K, yielding a rather featureless powder pattern of few peaks, consistent with the high symmetry of the cubic structure and dynamic orientational disorder. The temperature was then reduced to 280 K whereupon it became evident that a phase transition had occurred. A data set of substantial duration (12 hours) was then collected at this temperature yielding data in the 2θ range 10–130 ° for a 2θ step size of 0.05 °. A portion of the resulting profile is presented in figure 4.2(a). In the light of the d.t.a. and spectroscopic results discussed above, it was assumed that the 280 K pattern corresponds to phase III, and an attempt was made to determine its structure.

Automatic indexing of the 280 K pattern was carried out using KOHL, an adaptation [96] of a program by Kohlbeck and Hörl [97] which uses semi-exhaustive, index-trial methods for the *ab initio* determination of unit cell parameters from powder patterns of single solid phases. Trial indices are assigned to the lowest angle reflections to yield trial unit cells which are checked against volume constraints and then used to attempt to index the remaining lines. In common with most indexing programs, KOHL requires 20 preferably low-angle reflections for its operation. A figure of merit is attached to each solution and this assessment criterion and its reliability have been discussed by de Woolf [98].

Table 4.1 includes a list of all the observed sample reflections and their intensities for the 280K pattern as a function of 2θ. Using as input the 20 lowest-angle reflections of reasonable intensity, the program produced a number of candidate solutions only one of which successfully indexed all 20 lines. The second and subsequent candidate lattices matched 15 or fewer lines and were clearly inconsistent with many of the observed reflections. They were thus duly discarded as incorrect. The accepted solution, to which the program assigned a high figure of merit (25.3), gave an orthorhombic unit cell with parameters a=6.580, b=7.839

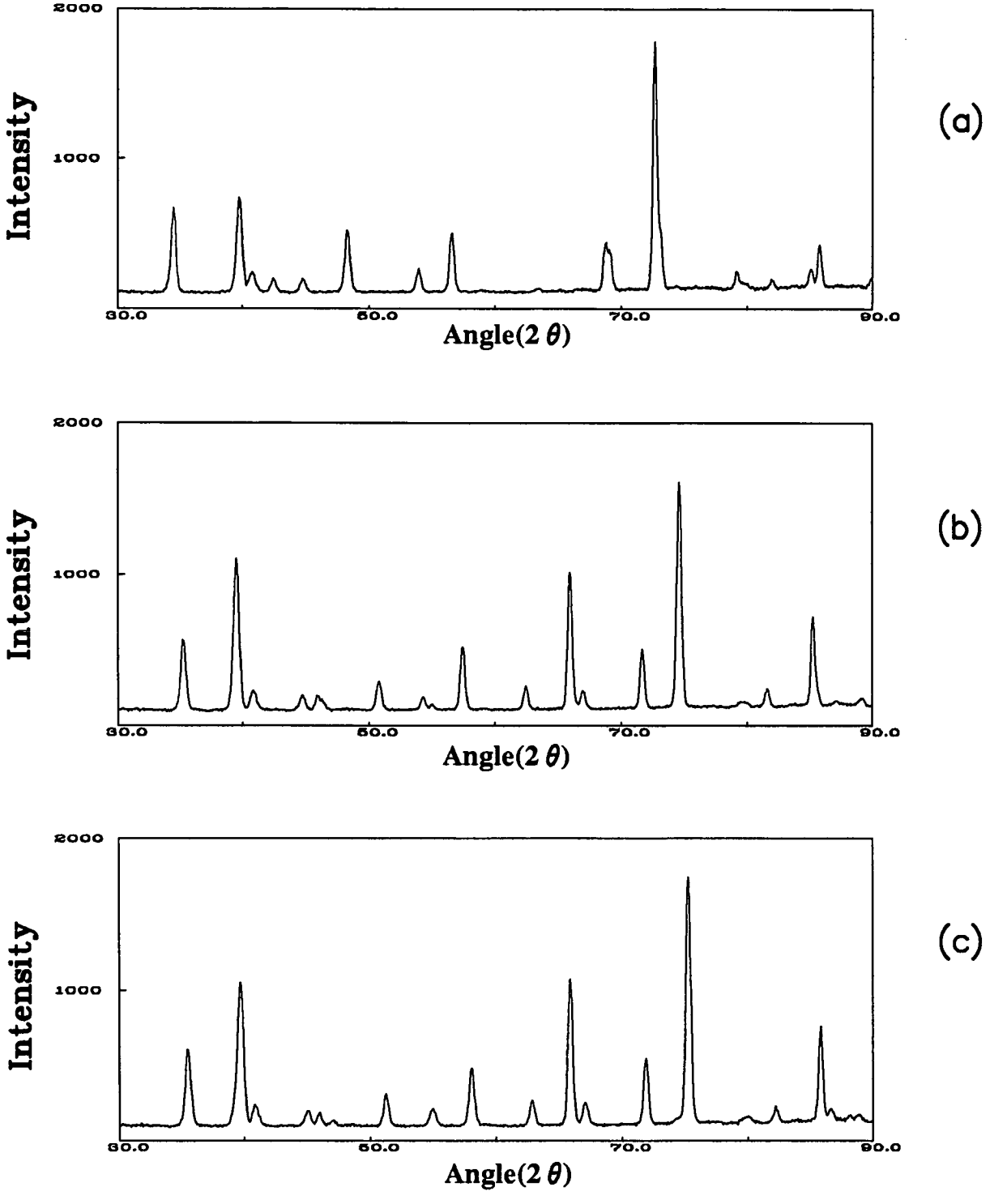

Figure 4.2: 5 kbar diffraction patterns (a) 280 K (b) 250 K (c) 175 K.

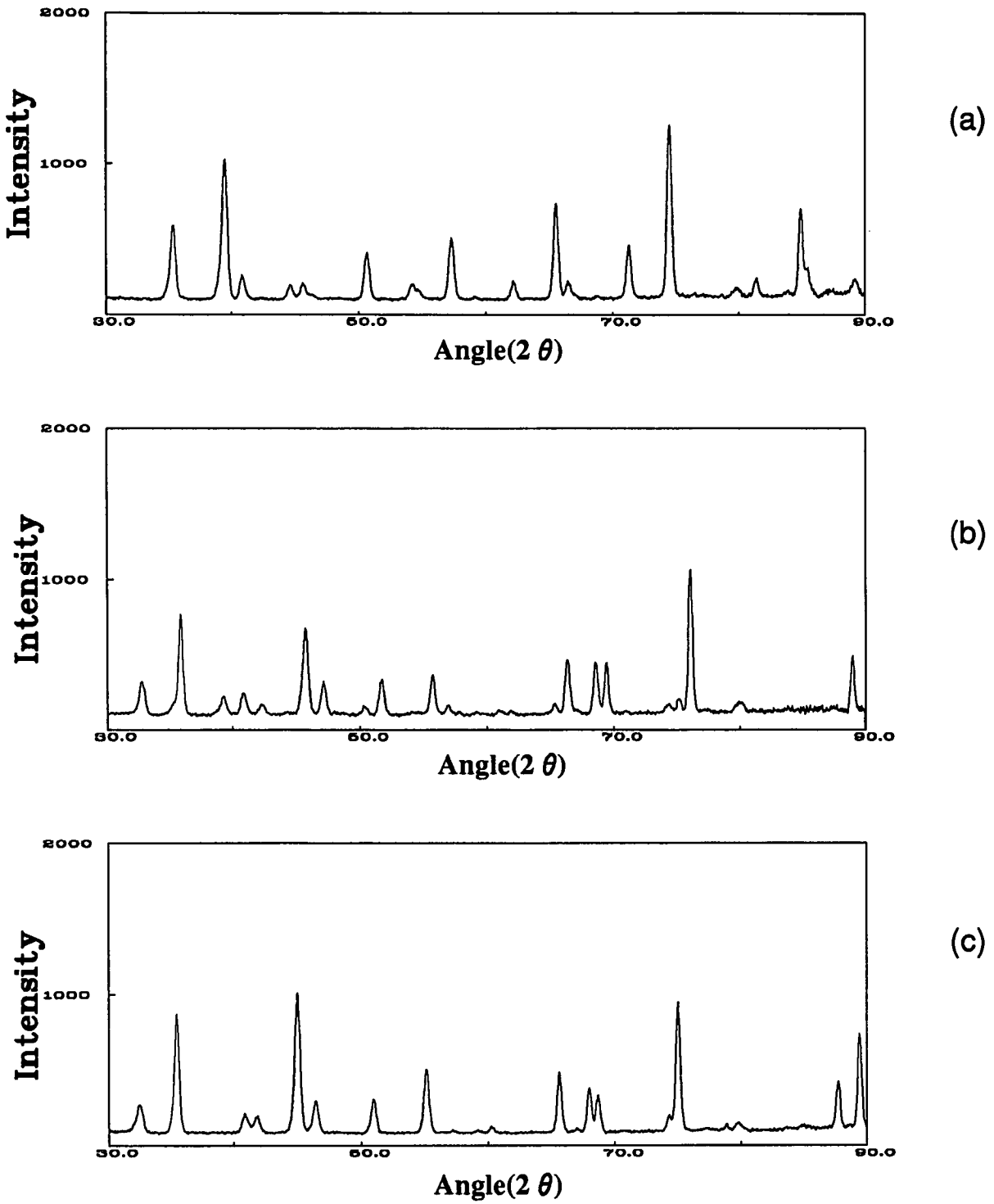

Figure 4.3: 175 K diffraction patterns. (a) 3 kbar (b) 2 kbar (c) 1 bar.

c=5.289 Å and a primitive lattice. Clearly the volume for this unit cell (V=273 $Å^3$) is approximately half that of the phase II unit-cell at ambient pressure (V=561). Accordingly it is reasonable to postulate that Z=2 for phase III.

With the unit cell from KOHL, it was possible, by noting the systematic absences in the reflection list, to deduce the reflection conditions given in table 4.2. These reflections are consistent with either the centro-symmetric spacegroup Pmnn or non-centrosymmetric P2nn (Nos. 58 and 34 respectively). For expediency, the higher symmetry spacegroup, Pmnn, will be assumed provisionally. This choice will be justified *a postiori*.

The symmetry operators of the Pmnn spacegroup dictate that, given two compact molecules in the unit cell, the centre of one molecule must coincide with a lattice site at the cell corner whilst the other must occupy the body centre. The spacegroup also has a centre of symmetry and a mirror plane at x=0, which place restrictions on the atomic positions. Using the Pmnn spacegroup, the deduced lattice parameters were refined in conjunction with the profile data, using the ALLHKL program of Pawley [99]. Refined values for the cell parameters are to be found in table 4.3. These parameters were used to generate the calculated reflection angles, also listed in table 4.1.

The approximate molecular orientation for phase III was determined using a combination of lattice energy minimisation and constrained Rietveld refinement as follows. Initially, an idealised rigid 'chair-shaped' cyclohexane molecule was assumed having tetrahedral bond angles and D_{3d} symmetry. The coordinates of this molecule, which are identical to those used for the molecular dynamics simulations of Trew *et al.* [100] are given in table 4.4, and the molecule is represented pictorially in figure 4.4. The bond-lengths are those appropriate to a deuterated system, having a C-D distance slightly shorter than the usual C-H bond-length by 0.007 Å . By virtue of the mirror plane at x=0, the one two-fold rotation axis of the molecule is preserved and is constrained to coincide with the x-axis, permitting the rigid molecule only a single degree of freedom, namely a rotation about the x-axis.

h	k	l	2θ(Obs)	Count	2θ(Zero)	2θ(Calc)	$\Delta(2\theta)$
1	1	0	34.426	670	34.478	34.476	0.002
0	1	1	39.774	737	39.826	39.828	-0.002
1	0	1	42.411	198	42.462	42.473	-0.011
0	2	0	44.711	196	44.762	44.809	-0.047
1	1	1	48.269	519	48.320	48.320	0.000
2	0	0	53.923	270	53.975	53.985	-0.010
0	2	1	56.568	504	56.620	56.629	-0.009
1	2	1	63.468	137	63.520	63.445	0.075
0	0	2	68.759	441	68.810	68.752	0.058
2	1	1	69.046	392	69.098	69.148	-0.050
2	2	0	72.658	1784	72.710	72.695	0.015
0	1	2	*			73.10	
1	3	0				75.87	
1	1	2	*			79.18	
0	3	1	79.184	249	79.236	79.229	0.007
2	2	1	82.031	200	82.083	82.065	0.018
1	3	1	85.136	263	85.188	85.188	0.000
0	2	2	85.797	413	85.849	85.879	-0.030
3	1	0	89.940	207	89.991	89.980	0.011
1	2	2				91.73	
2	0	2	92.803	312	92.855	92.843	0.012
3	0	1	94.842		94.894	94.910	-0.016
2	1	2	96.961	248	97.013	97.021	-0.008
3	1	1	99.083	885	99.134	99.152	-0.018
0	4	0	*			99.28	
2	3	1				102.96	
0	3	2	106.848	533	106.900	106.936	-0.036
0	4	1	108.717	194	108.769	108.757	0.012
2	2	2	109.838	206	109.890	109.885	0.005

Table 4.1: Observed and calculated reflections of cyclohexane-d_{12} at 5 kbar, 280 K in the Pmnn spacegroup. The calculated reflections were generated using the refined cell parameters and zero error given in table 4.3. Those reflections that may not have been resolved are marked by an asterix (*). The 301 reflection has not been assigned an intensity as it lies very close to the 200 Al line.

h	0	l	h + l = 2n
h	k	0	h + k = 2n
h	0	0	h = 2n
0	k	0	k = 2n
0	0	l	l = 2n

Table 4.2: Reflection conditions deduced from the 5 kbar, 280 K diffraction profile.

Parameter	T=280 K	T=250 K	T=175K
a(Å)	6.587(3)	6.526(4)	6.518(5)
b(Å)	7.844(7)	7.597(6)	7.496(7)
c(Å)	5.295(3)	5.463(5)	5.460(4)
β(°)	90	97.108(4)	97.725(3)
Volume (Å^3)	273.64(4)	268.71(3)	264.42(4)

Table 4.3: Lattice parameters of cyclohexane-d_{12} at 5 kbar for T= 280 K, 250 K and 175 K.

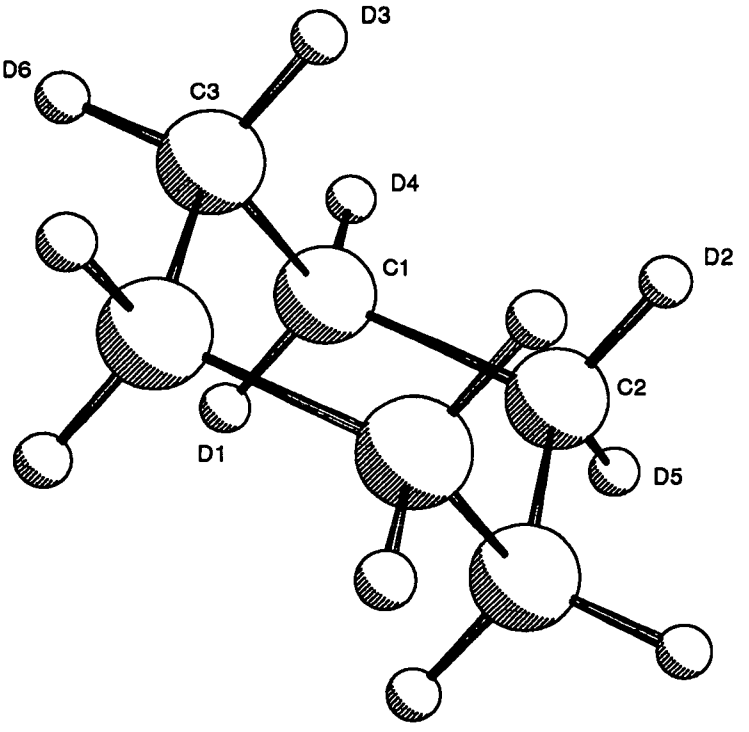

Figure 4.4: The ideal cyclohexane molecule in the 'chair' conformation. The molecule has D_{3d} symmetry and tetrahedral bond angles.

Parameter	x(Å)	y(Å)	z(Å)
C1	1.2664	0.7311	-0.2585
C2	1.2664	-0.7311	0.2585
C3	0.0000	-1.4623	-0.2585
D1	1.2664	0.7311	-1.3415
D2	1.2664	-0.7311	1.3415
D3	0.0000	-1.4623	-1.3415
D4	2.1506	1.2416	0.1024
D5	2.1506	-1.2416	-0.1024
D6	0.0000	-2.4833	0.1024

Table 4.4: Atomic coordinates of the idealised molecule used for energy minimisation calculations. Only half the atoms of the molecule are given, the remainder follow from an inversion through the origin.

Using the deduced unit cell parameters and idealised molecular dimensions, energy minimisation was performed for a cluster of approximately 100 computer-generated, rigid molecules. The intermolecular potential employed was of the Buckingham form (6-exp) with the parameters of Williams [101]. These parameters are those appropriate to hydrogenated systems as non could be found in the literature for deuterated systems. No intra-molecular (strain) energies were included in these calculations.

Whilst maintaining the symmetry constraints associated with the Pmnn space-group, the lattice energy was monitored as a function of the molecular rotation angle, for a rotation of 90° about the x-axis. This procedure yielded a global energy minimum when the vector from the origin to the C3 atom was inclined at 38.48 ° degrees to the y axis. The molecular orientation corresponding to this energy minimum was used as the starting point for a Rietveld refinement of the powder diffraction profile of phase III.

Rietveld refinement was carried out using data collected at 5 kbar, 280 K from

the D2B diffractometer. As previously described, the smaller neutron wavelength (1.595 Å) associated with this diffractometer permits a greater number of Bragg-peaks to be collected (compared to the larger wavelength employed on D1A), thereby increasing the information content of the data. The Rietveld method involves a least-squares refinement of structural and thermal parameters from powder diffraction patterns and is discussed in detail in reference [102]. The refinements were carried out using the PROFIL neutron powder refinement program available at ILL [103]. Initially 8 parameters were refined (cell parameters, scale, zero error and U,V,W) with no adjustment of atomic coordinates. The background was treated by a polynomial fit to 150 visually estimated points and a pseudo-Voigt peak shape was employed to model the observed peaks. Isotropic thermal parameters were not refined and were set to be 5.53 for D atoms and 1.11 for C atoms. The refinement converged quickly with a final intensity R-factor of 8 %, where

$$R_I \equiv \frac{\Sigma_i |Y_i^{obs} - Y_i^{calc}|}{\Sigma_i Y_i^{calc}}$$

Chemical or 'slack' constraints were then placed on the bond lengths and angles in order that they should favour the geometry of the idealised molecule. This brought the number of refinable parameters to 19. The size of the maximum permitted deviation of the bond parameters from the idealised structure was limited (somewhat arbitrarily) to be consistent with the deviation from the ideal geometry observed by Kahn *et al* [82] for phase II. Of course, the constraints imposed by the spacegroup symmetry were not relaxed.

Allowing refinement within these constraints, the intensity R-factor improved markedly to 4%. The refined profile is presented in figure 4.5 with the corresponding atomic coordinates, principal bond parameters and refinement parameters appearing in tables 4.5, 4.6 and 4.7 respectively. The refined bond parameters suggest that the cyclohexane molecule in phase III deviates only slightly from tetrahedral symmetry, for which bond angles assume the value 109.6°. The measured bond lengths also agree well with values encountered in the literature i.e.

Parameter	x/a	y/b	z/c
C1	0.19041	0.03837	-0.13348
C2	0.19041	-0.03837	0.13348
C3	0.00000	-0.14136	0.17404
D1	0.19041	-0.06616	-0.26537
D2	0.19041	0.06616	0.26537
D3	0.00000	-0.25253	0.06142
D4	0.31114	0.12485	-0.14824
D5	0.31114	-0.12485	0.14824
D6	0.00000	-0.19821	0.36632

Table 4.5: Refined atomic coordinates of cyclohexane-d_{12} at 5 kbar and 280 K.

C1–C3(Å)	1.509(8)	C3–D3(Å)	1.06(7)
C1–C2(Å)	1.538(6)	C3–D6(Å)	1.11(9)
C1–D1(Å)	1.07(6)	C2–C1–C3(°)	109.9(7)
C1–D4(Å)	1.05(5)	C1–C3–C1[1](°)	112.6(4)

Table 4.6: Estimates of the independent bond-lengths and principle bond-angles obtained from the refinement of D2B data for phase III at 5 kbar 280 K.

Parameter	Value
Refined parameters	19
u(°)	0.228
v(°)	−0.321
w(°)	0.265
scale factor	2.7345(3)
zero angle(°)	−0.050(3)
Asymmetry parameter	0.292
2θ refinement range	15°–80°
2θ step size	0.05°
Observed data points	2100
R_I	4.4
R_{wp}	8.6

Table 4.7: Values of the instrumental parameters and R-factors for the refinement of the phase III powder pattern at 5 kbar, 280 K.

C-C 1.536, C-D 1.083 [104]. Furthermore, the success of the refinement demonstrates that the centrosymmetric spacegroup is indeed the appropriate choice for this structure. A carbon skeletal representation of the refined molecular arrangement relative to the unit cell is shown in figure 4.6.

4.3.2 Phase IV : The Monoclinic Phase

A number of short data sets were collected at 5 kbar between 280 K and 260 K in 5 K steps, in order to establish closely the temperature of any further transition. At 265 K a clear change in the powder profile was observed, heralding the entry to a new phase. Another short data set at 260 K revealed a pure phase, showing the 265 K profile to be a mixture of the upper and lower phases. The temperature was subsequently reduced further to 250 K to ensure that the sample was fully in the lower phase at that temperature, and a high quality data set was collected over a period of some 8 hours, yielding data in the 2θ range 10–117°. Again a 2θ step size of 0.05 ° was used. The associated pattern is shown in figure 4.2(b).

The indexing procedure described above for phase III was repeated with the 250 K data, the peak positions of the lowest angle reflections (of reasonable intensity) being input to the KOHL program. Again this program offered a number of solutions. The 'best', indexing all 20 reflections with a figure of merit of 20.4 was a primitive monoclinic cell with parameters a=6.523, b=7.585, c=5.457Å, $\beta = 97.127°$. The next best solution with a figure of merit of just 9.3, failed to index some of the reflections and was rejected. A comparison of the above cell with that derived for phase III shows clearly that they are closely related, the transition being affected by a simple tilting of the c axis of the orthorhombic structure concomitant with a small ($\sim 2\%$) reduction in unit cell volume. In view of the previously mentioned d.t.a. and neutron scattering results, the structure at 5 kbar, 250 K will be assumed to be phase IV.

All the observed sample reflections and their intensities for the 5 kbar, 250 K pattern are presented in table 4.8. From a consideration of the systematic absences

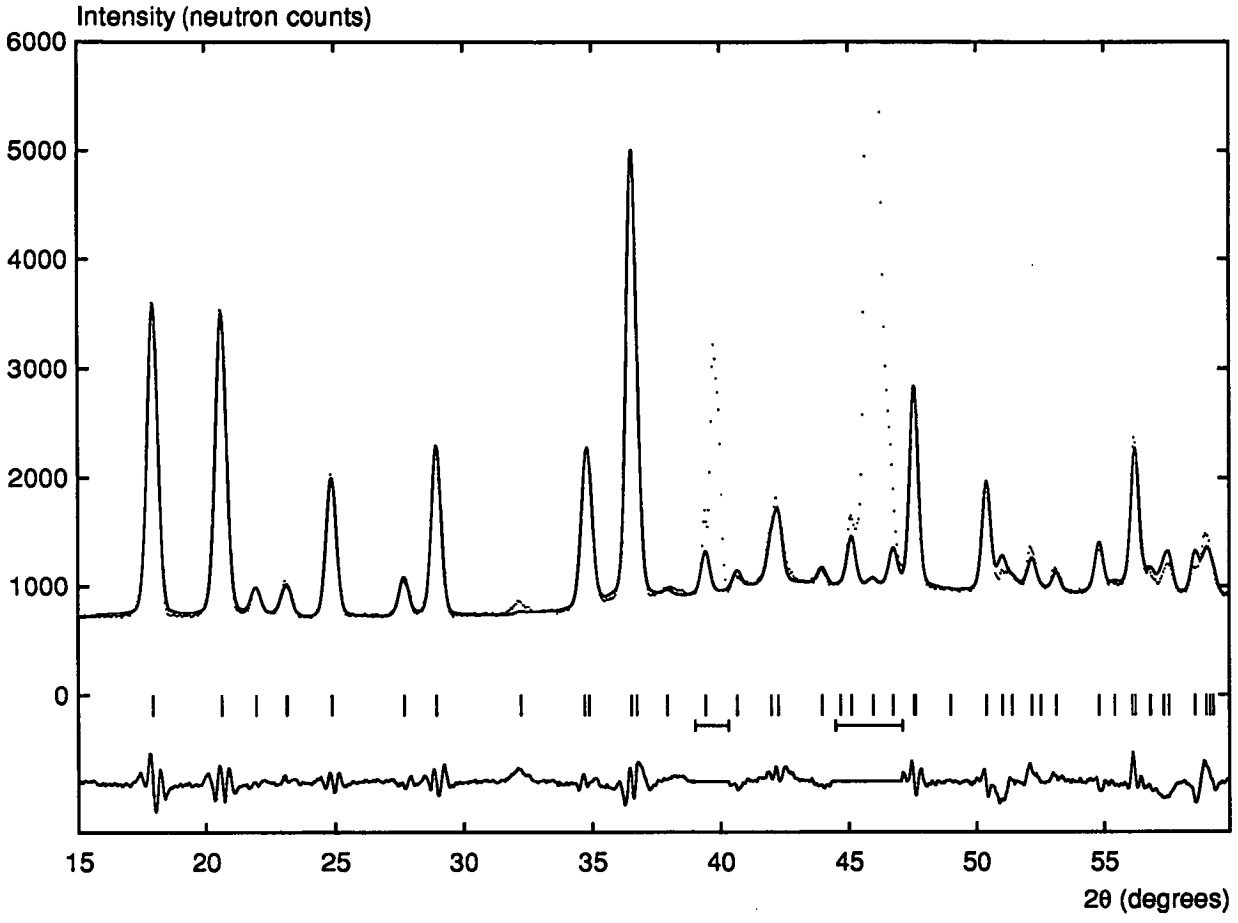

Figure 4.5: A difference plot of the observed and calculated powder diffraction profile of phase III at 5 kbar, 280 K. The measured data points are shown as dots and the calculated profile is shown by the solid line. Vertical bars denote the positions of Bragg reflections. The peaks centred on 39° and 46°, arise from scattering from the aluminium housing of the pressure cell and were excluded from the data used for refinement.

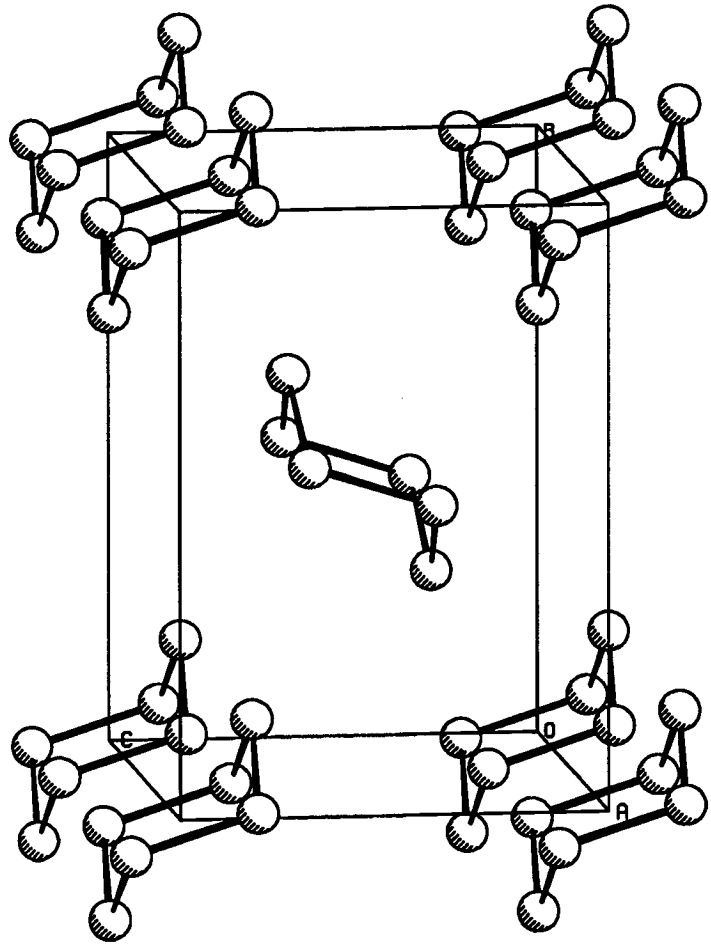

Figure 4.6: The refined structure of phase III relative to the orthorhombic unit cell. Note the 'herring-bone' molecular stacking common to many organic molecular crystals.

h	k	l	2θ(Obs)	Count	2θ(Zero)	2θ(Calc)	$\Delta(2\theta)$
1	1	0	35.314	566	35.318	35.305	0.013
-1	0	1	*			39.38	
0	1	1	39.541	1100	39.545	39.595	-0.050
1	0	1	44.716	202	44.720	44.768	-0.048
-1	1	1	45.904	205	45.908	45.929	-0.021
0	2	0	46.269	172	46.273	46.338	-0.065
1	1	1	50.792	291	50.796	50.761	0.035
1	2	0	54.300	190	54.304	54.276	0.028
2	0	0	55.018	141	55.022	54.975	0.047
0	2	1	57.462	511	57.466	57.427	0.039
2	1	0				60.23	
-1	2	1	62.436	252	62.440	62.397	0.043
-2	1	1	65.968	1016	65.972	65.953	0.019
1	2	1				66.39	
0	0	2	66.974	235	66.978	66.929	0.049
0	1	2	71.661	493	71.665	71.671	-0.006
2	1	1				73.65	
-1	1	2	*			74.28	
2	2	0	74.622	1609	74.626	74.672	-0.046
1	3	0				78.64	
-2	2	1				79.90	
0	3	1	*			81.29	
1	1	2	81.637	242	81.641	81.664	-0.023
-2	0	2				84.73	
0	2	2	85.284	363	85.288	85.280	0.008
-1	3	1	*			85.62	
2	2	1	87.192	164	87.196	87.17	0.026
-1	2	2				87.78	
-2	1	2	89.214	180	89.218	89.176	0.042

Table 4.8: Observed and calculated reflections of cyclohexane-d_{12} at 5 kbar, 250 K in the P12(1)/n1 spacegroup. The calculated reflections were generated using the refined cell parameters and zero error given in table 4.7. The 122 and -311 reflections have not been assigned an intensity as they lie very close to the 200 Al line. Those reflections that may not have been resolved are marked by an asterix (*). The apparently unobserved reflections -131 and 131 are coincident with their neighbours and are visible in the 5 kbar 175 K pattern.

h	0	l	h + l = 2n
h	0	0	h = 2n
0	k	0	k = 2n
0	0	l	l = 2n

Table 4.9: Reflection conditions deduced from the 5kbar, 250K diffraction profile.

from this reflection list, it transpires that the structure satisfies the reflection conditions given in table 4.9.

These reflection conditions are compatible only with the P 1 2 (1)/n 1 space-group (a setting of P 2 (1)/c, b axis unique, cell choice 2, No.14) spacegroup. Significantly, this spacegroup is a maximal non-isomorphic subgroup of the Pmnn spacegroup for the phase III structure, corresponding to the removal of half the symmetry elements in the transition from the orthorhombic to the monoclinic structure. This independent deduction therefore lends weight to the validity of the findings for both structures. In particular the non-centrosymmetric orthorhombic spacegroup P2nn is not compatible with the transition to the P 2 (1)/c structure. Moreover, the vast majority of organic homomolecular crystals are centrosymmetric and fall into the P 2 (1) / c spacegroup [105].

The pattern at 5 kbar, 175 K, fig 2(c), was also subjected to the indexing procedure yielding a 'best' cell of a=6.511, b=7.485, c=5.463 Å; β = 97.733°; with a figure of merit of 25.5. Evidently the structure at this temperature is still essentially the same as that observed at 250 K although the temperature is considerably below that where one would expect to find phase IV according to the phase diagram of Schulte and Würflinger (figure 4.1(b)). No evidence of a phase transformation to phase II was observed at 5 kbar 175 K even though the sample was maintained under these conditions for a period in excess of 12 hours. Clearly this finding is in accord with that of Mayer *et al* [90] who observed that the temperature range of stability of phase IV is increased considerably on cooling from phase III compared to heating from phase II.

Both the 250 K and the 175 K cell solutions were refined using the ALLHKL program, yielding the lattice parameters presented in table 3. Differences between the profiles of fig 2(b) and fig 2(c) may be traced to the small difference in the lattice parameters between the two temperatures. The somewhat larger figure of merit of the 175 K indexing compared to that at 250 K arises from the splitting of accidently coincident low-angle peaks which separately receive greater weight in the figure of merit calculation. Those peaks not observed at 250 K (and therefore absent from table 4.8 which are apparent in the 175 K data, are the (-131) and (131) reflections. It is instructive to try to gauge the angular resolution of the diffraction profile from those close lying peaks (e.g. the (002) and the (221) reflections in table 4.1 and figure 4.2(a)) which are only just resolved. From the data it appears that the angular resolution is approximately 0.4°. Thus a number of the reflections apparently absent from tables 4.1 and 4.8 may just not have been resolved. In these cases the table entry for a reflection is marked with an asterix.

In a manner similar to that described for phase III, energy minimisation calculations for the phase IV structure have been performed in an attempt to find a molecular orientation sufficiently close to the real configuration to permit Rietveld refinement of the powder data. Again the molecule coordinates of table 4.4 were used, suitably transformed into the monoclinic basis. However, the task of locating the energy minimum was complicated considerably by the lack in the monoclinic structure of the mirror plane existing in the orthorhombic phase. Consequently, no orientational constraints are imposed on the molecule which thus possesses three degrees of orientational freedom. For a rather compact, spherical molecule such as cyclohexane it is to be expected that a number of spurious local minima exist in the potential energy surface. Indeed this was found to be the case, necessitating an exhaustive search of trial starting orientations, until one lying within the basin of attraction for the global energy minimum was eventually found. A stereoscopic carbon skeletal representation of the molecules in the orientation of minimum energy is given in figure 4.7.

The minimum energy molecular orientation in phase IV is clearly related to that of phase III. The main qualitative difference appears to be a rotation of the molecular

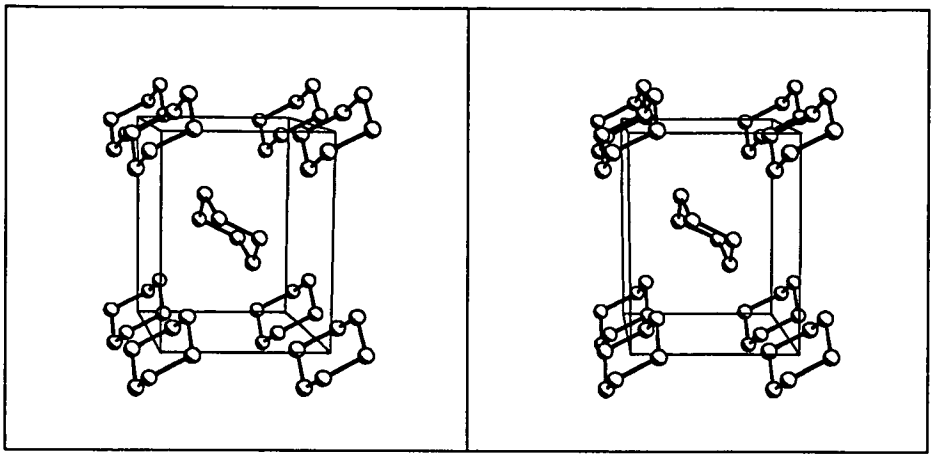

Figure 4.7: A stereoscopic view of the calculated structure of minimum potential energy for phase IV. The structure was obtained using the molecular geometry of Trew *et al* [100] combined with the potential parameters of Williams [101].

orientation in the same sense as the monoclinic tilt. This 'solution' was used as the starting point for a constrained Rietveld refinement of the powder profiles in which the bonding parameters were again constrained to favour the idealised molecule. Unfortunately, the best intensity R-factor which could be obtained by this process was 18% (for 1959 data points and 35 refined parameters), significantly inferior to that obtained in the orthorhombic phase. Discussion of possible reasons for this are deferred to the following section.

4.3.3 The Transition to Phase II

Figure 4.3(a) to (c) shows the result of decreasing the pressure from 3 kbar at a constant temperature of 175 K. At 3 kbar, fig 3(a), the structure is evidently still that of phase IV observed at 5 kbar. However at 2 kbar, (fig 4.3b), a dramatic change occurs in the powder pattern. By comparing the 1 bar pattern of fig 4.3(c) with that at 3 kbar it is evident that the 2 kbar pattern simply comprises a mixture

of the upper and lower pattern, implying phase coexistence. At this temperature, the actual transition pressure is clearly therefore very close to 2 kbar. Moreover, the observation of phase coexistence suggests that this transition has first order character.

In certain circumstances, however, phase IV does not transform to phase II, even when the pressure is reduced to its ambient value [90]. Provided the pressure is released at temperatures below 160 K, phase IV persists (apparently stably) down to ambient pressure. The transformation to phase II can then only be effected by heating to approximately 160 K. This rather interesting finding will be discussed further in the concluding section.

The 1 kbar and atmospheric pressure patterns (the latter shown in figure 4.3(c)) correspond to the known structure of phase II as determined by the single-crystal x-ray study of Kahn *et al* for C_6H_{12}. The latter profile was, however, independently indexed by way of a test of the indexing procedure. For this pattern, the KOHL program yielded a best solution (figure of merit 25.4) with lattice parameters a=11.28, b=6.43, c= 8.24Å; β = 108.84° and a centred cell, in excellent agreement with the x-ray results.

Powder patterns were also collected for phase II, using the D2B diffractometer. Rietveld refinement of this data was performed using as starting conditions, the atomic parameters determined in the single-crystal x-ray study of Kahn *et al* [82]. This refinement proceeded normally and converged with a final R-factor of 5%. The refined positions of the carbon atoms were found to be in good agreement with the results of the x-ray study. However, the deuterium atoms were found to occupy positions much closer to the ideal cyclohexane structure than had been reported previously. Leaving aside the possibility of differences due to isotopic substitution, this disparity can almost certainly be traced to the relative accuracy of x-ray and neutron diffraction for determining the position of hydrogen atoms. Although single-crystal diffraction data is normally much more reliable than powder data, the coherent scattering cross section presented by hydrogen (and deuterium) to x-rays is considerably less than to neutrons. Accordingly, the positions of the

Parameter	x/a	y/b	z/c
C1	0.206(2)	0.469(7)	-0.005(4)
C2	0.345(3)	0.408(3)	0.085(2)
C3	0.382(3)	0.214(3)	0.006(3)
D1	0.190(2)	0.501(7)	-0.127(2)
D2	0.184(1)	0.603(5)	0.048(5)
D3	0.354(3)	0.386(1)	0.216(6)
D4	0.404(4)	0.534(3)	0.080(4)
D5	0.376(2)	0.251(2)	-0.117(5)
D6	0.477(5)	0.189(5)	0.068(4)

Table 4.10: Refined atomic coordinates of cyclohexane-d_{12} in phase II at 1 bar and 175 K. The refined unit cell parameters are a= 11.30(3)$\AA$, b= 6.43(6)$\AA$, $c = 8.23(4)\AA$, $\beta = 108.84(5)°$.

deuterium atoms can be determined considerably more accurately by neutron diffraction than by x-ray diffraction. It would seem likely, therefore, that at least with regard to the positions of the hydrogen atoms, the cyclohexane molecule is rather less distorted than reported by Kahn *et al.* The refined atomic positions for phase II are given in table 4.10. Table 4.11 shows the principal bond lengths and representative bond angles for phase II as determined both by Kahn *et al* and by the present study.

4.4 Discussion and Conclusions

The orthorhombic structure of phase III is clearly consistent with the spectroscopic deduction of D_{2h} site symmetry by Haines & Gilson [86]. Their finding of C_{2h} symmetry for the room-temperature structure existing above 7.4 kbar in C_6D_{12} could, however, correspond either to phase II or to phase IV as both possess this site symmetry. Extrapolations of the phase diagram (figure 4.1(b)) suggest that

Parameter	Reference [82]	This work
C(1)–C(2)	1.528(6)	1.537(12)
C(2)–C(3)	1.52(1)	1.522(7)
C(3)–C(4)	1.51(1)	1.522(8)
C(6)–C(1)–C(2)	110.4(6)	110.7(6)
C(1)–C(2)–C(3)	111.3(4)	111.3(5)
C(2)–C(3)–C(4)	112.3(4)	112.0(7)
C(1)–D(1)	0.88(3)	0.98(3)
C(1)–D(2)	1.14(4)	1.04(3)
C(2)–D(3)	1.05(3)	1.05(4)
C(2)–D(4)	0.93(3)	1.07(2)
C(3)–D(5)	1.10(2)	1.03(3)
C(3)–D(6)	0.94(4)	1.07(4)
C(1)–C(2)–D(1)	106.7(3)	112.6(7)
C(1)–C(2)–D(2)	105.7(5)	109.9(5)
C(2)–C(1)–D(4)	118.2(4)	110.7(3)

Table 4.11: Principal bond lengths and selected bond angles for the cyclohexane molecule in phase II.

phase IV is the best candidate for this phase. Indeed, the recently discovered 12 kbar transition at room temperature [88] also appears to be consistent with an extrapolation to room temperature of the phase IV to phase II boundary.

The failure to obtain a satisfactory Rietveld refinement for phase IV may be partially traced to the fact that energy minimisation is less powerful when trying to orient 'globular' molecules having unconstrained orientational freedom. Under such unfavourable conditions, any shortcomings in the authenticity of the potential parameters [101] can make the correct solution illusive. In fact the potential parameters employed for the energy minimisation calculations were those appropriate to hydrogen, rather than deuterium. Given that the region of stability of phase IV is heavily influenced by isotopic factors (as evidenced by the phase-diagrams of figure 4.1), it is perhaps not too surprising that energy minimisation produced an apparently spurious result. A further possibility is that the cyclohexane molecule is significantly distorted in phase IV. If this is indeed the case, energy minimisation based on a rigid-molecule approximation cannot be expected to succeed.

Notwithstanding the failure to obtain a full structural solution to phase IV, a good deal of confidence is reserved for the results pertaining to the orthorhombic phase III. Here the molecule is tightly constrained by the spacegroup symmetry, and the success of the Rietveld refinement implies that the deduced molecular orientation lies very close to the correct solution.

The finding that phase III is an ordered phase possessing no large-scale dynamic disorder is at variance with recent speculation that phase III is actually a one-dimensional rotator phase [90]. This claim was made on the basis of an observed change in the phonon-mode spectrum at the phase III–phase IV transition. It is nevertheless difficult to see how such a claim can be reconciled with the results of the present study. The refined bond parameters for phase III (table 4.6) indicate that the cyclohexane molecule does not deviate significantly from the ideal structure. Such a result could not have been obtained were the molecule rotating rapidly about one axis. Moreover, previous neutron powder work on 1-d rotator

phases, such as that of n-butane, show that the orientational disorder leads to a large thermal Debye-Waller effect, manifest as a loss of peak intensity at high angle [106, 107]. No obvious diminution of peak intensity was observed in phase III compared to either phase IV or phase II, and no anomalous behaviour of the temperature parameters was encountered in the refinement. In fact, in order to perform successful Rietveld refinement of a uniaxial rotator such as n-butane, it is necessary to employ rather complex models, which explicitly embody the disorder about the rotation axis [106, 107].

The assertion that phase III is characterised by large-scale dynamic disorder would also appear to run contrary to the thermodynamic evidence. Only a small volume change occurs at the phase III-IV transition (table 4.3). If phase III were extensively disordered, one would expect (on the basis of the Clausius-Clapeyron equation), that the gradient of the phase III-IV boundary should be large. The measured gradient (fig 4.1) does not, however, differ significantly from that of the phase II-IV boundary. Thus, while it is possible that the cyclohexane molecule in phase III undergoes occasional symmetry related reorientations, (similar to the phenomenon observed in solid benzene [108]), it is the author's view, that the molecules in phase III spend their time predominantly in the orientation shown in figure 4.6.

Turning finally to the general issues raised in the introduction, it would appear that several factors govern the particular crystalline structure adopted by cyclohexane. In the plastic phase I, the isotropic orientational freedom of the molecules leads to a cubic structure corresponding to the close-packing of hard spheres. At lower temperatures, this orientational freedom freezes out, and the ordered phase II is formed. The packing density in this latter phase is considerably (12%) greater than that of phase I. As there is little evidence to suggest that the cyclohexane molecule is significantly distorted in either phase II or phase I, it would appear that the phase II-phase I transition is essentially entropy driven.

At higher pressures, two further structures (phases III and IV) exist. Phase III is formed by cooling from phase I and further cooling then yields phase IV. Both

phases III and IV appear to be orientationally ordered and their crystallographic structures are closely related. In phase III, the molecule is in the chair conformation and is not significantly distorted. Raman measurements indicate that no large-scale conformation changes occur at the phase III-IV transition although it is possible that the molecule is distorted in phase IV [87, 88]. Given that the decrease in molecular volume ($\sim$ 2%) at the phase III-IV transition is relatively small, both compact packing and molecular distortion may be responsible for driving this transition.

One of the more intriguing features of the phase behaviour of deuterated cyclohexane is the dependence of the locus of the phase II – phase IV boundary on the direction in which it is traversed. The position of this boundary as shown in figure 4.1(b), relates only to the transition *from* phase II *to* phase IV. Once phase IV is formed, decreasing the pressure will regain phase II only if the temperature is maintained above 160K. Otherwise, phase IV will persist (apparently stably), right down to ambient pressure. The source of this pronounced hysteresis may presumably be traced to a large energy barrier separating the two phases. Indeed no obvious structural relationship exists between the unit-cells of phases II and IV, implying that the transition involves large-scale molecular rearrangements, possibly involving an energetically unfavourable intermediate state. The existence of the hysteresis poses the intriguing question as to which phase is the true structure of minimum free energy at ambient pressure and low temperature.

With regard to the effect of deuteration on the phase diagram of cyclohexane, it appears that this matter is still poorly understood. Although the C-D bond length is known to be approximately 0.007 Å shorter than its C-H counterpart, it is doubtful that this alone can account for the presence of phase IV. In fact, a recent Raman study has identified phase IV in the hydrogenated system at considerably higher pressures than observed in the deuterated systems [88]. On this basis, it would seem that the effect of deuteration is to produce an increase in the *chemical* or internal pressure rather than to introduce a completely new phase altogether.

To summarise, the observed phase structure of cyclohexane is mediated by a complex interplay between several factors: dynamic effects, compact packing, molecular distortion, isotopic substitution and thermodynamic history. In general, high-symmetry dynamical disordered phases are favoured at high temperature and lower-symmetry orientationally ordered arrangements are favoured at lower temperatures and higher pressures. This trend is observed across a variety of related organic molecular systems such of cyclohexanone, cyclopentane and cyclohexanol whose phase diagrams are topologically similar to that of cyclohexane [109]. Qualitative features of the structural determinations reported in this work may very well carry over to these related systems.

4.5 Prospects for Further Work

Evidently a full structural solution of phase IV is a prerequisite for a comprehensive understanding of the phase behaviour of cyclohexane. Such a determination might be possible using direct methods, whereby one evaluates the individual structure factors associated with each reflection in the powder diffraction profile. In principal, knowledge of these structure factors permits a full structural determination of atomic positions, although the task is non-trivial and has not been attempted here. Energy minimisation may also yet prove useful for solving phase IV, provided more information is forthcoming regarding the manner and extent of molecular distortion.

A determination of the structure of the ambient-pressure metastable phase observed by Renaud and Fourme [83] would also be worthwhile. Such a solution might convey important insight into the role of pre-transitional molecular ordering in determining the low-temperature structure of phase II. As previously described, this metastable phase is formed by quenching cyclohexane from phase I or the liquid and has recently been studied by Raman spectroscopy at Edinburgh [88]. The Raman study clearly identified lattice modes in the spectra, demonstrating that the metastable phase is ordered and contrary to some reports [111],

not a quenched glass. It was found, however, that the pure metastable phase can only be produced for small quantities of the hydrogenated system. Larger sample volumes and/or a deuterated sample, yielded a mixture of the metastable phase and the low-temperature monoclinic phase II. For these reasons, X-ray powder diffraction rather than neutron diffraction would be the preferred technique for structure solution since the latter requires large-volume deuterated samples.

The advent of new constant-pressure molecular dynamics techniques also provides further scope for study of the high-pressure structures and transitions of cyclohexane [110]. These new techniques allow one to simulate first order structural phase transitions that involve a volume change. Molecular dynamics simulations have already been performed with some success for the ambient pressure phases of cyclohexane [100]. It would be extremely interesting to see if they can also reproduce the high-pressure structures, possible by incorporating flexible molecules. Simulations of this type could provide valuable information on the dynamic reordering processes taking place at the phase-transitions as well as providing indications concerning the accuracy of the existing form of atom-atom potentials.

Appendix A

Derivations of Scaling Results

In this appendix, further details are given of some of the scaling results stated in chapter 1.

A.1 The Form of the Scale Factor $\Lambda(b)$

As stated in chapter 1 of the main text (section 1.7), the basic spin amplitude σ_x must be rescaled by a factor $\Lambda(b)$ in order that the partition function remains invariant under the RG operation (c.f. equation 1.18). The iterable properties of the RG operator further stipulate that $\Lambda(b)$ must be of the general form $\Lambda(b) = b^c$, with c constant.

The explicit form of $\Lambda(b)$ derives from a consideration of the two-point spin correlation function $G(x) =< \sigma_0 \sigma_x >$. At criticality and for large spin separation x, it turns out that [4]

$$G_c(x) \approx D_c x^{-(d-2+\eta)} \tag{A.1}$$

where D_c is a critical amplitude and η is a critical exponent. Now, the operation of the RG transformation on the correlation function may be written

$$G(x,\mathcal{H}) = \Lambda(b)^2 G(x/b,\mathcal{H}') = b^{2c} G(x/b,\mathcal{H}') \tag{A.2}$$

Setting the arbitrary scale factor b equal to x, then immediately yields

$$\Lambda(b) = b^{-(d-2+\eta)/2} = b^{-\beta/\nu} \tag{A.3}$$

where the hyper-scaling relation $\beta = \nu(d-2+\eta)/2$ has been used.

A.2 The Form of the Relevant Scaling Fields μ_1 and μ_2

The form of the relevant scaling fields is simplest for systems having the Ising symmetry, where the Hamiltonian is symmetric with respect to positive and negative values of the ordering field. Explicit forms for the relevant scaling fields are derived below for this special case. The situation for systems with broken symmetry, such as fluids, is discussed in detail in chapter 3.

Given a Hamiltonian $\mathcal{H}$ describing the interaction between an assembly of N spins, the Gibbs free energy per degree of freedom (in units of $k_B T$), may be written as

$$g = -\frac{\ln Z}{N} \tag{A.4}$$

Under the RG operation, the total free energy (like the partition function) remains invariant, although the number of degrees of freedom associated with the description of the system is reduced by a factor b^{-d} to $N' = N/b^d$. Accordingly and to within less singular terms one can write

$$g = b^{-d} g'(\mathbf{K}) \tag{A.5}$$

where $g'(\mathbf{K})$ is the Gibbs free energy per site for the coarse-grained system. In the region of the fixed point, the coupling-space vector $\mathbf{K}$ can be eliminated in favour of the scaling field perturbations $\mu_a(b)$ (equation 1.36), which suggests that the most singular part of the Gibbs free energy per site has the homogeneity property

$$g(t,h) = b^{-d} g(\mu_1(b), \mu_2(b)) = b^{-d} g(b^{\lambda_1} t, b^{\lambda_2} h) \tag{A.6}$$

where the quantities $\mu_1(b) \equiv b^{\lambda_1} t$ and $\mu_2(b) \equiv b^{\lambda_2} h$ are the relevant scaling fields whose system specific pre-factors have been suppressed for clarity. In writing down equation (A.6) it has been assumed that only two relevant scaling fields exist and that the system is sufficiently close to criticality that irrelevant perturbations can be ignored. In fact, equation (A.6) is identical to that written down in chapter 1 (equation 1.5) on the basis of purely phenomenological scaling theory.

On differentiating equation (A.6), one obtains corresponding scaling expressions for the order parameter and the susceptibility.

$$Q(t,h) = b^{\lambda_2 - d} Q(b^{\lambda_1} t, b^{\lambda_2} h) \tag{A.7a}$$

$$\chi(t,h) = b^{2\lambda_2 - d} \chi(b^{\lambda_1} t, b^{\lambda_2} h) \tag{A.7b}$$

Exploiting the homogeneity property, one can choose the arbitrary scale factor b such that

$$b^{\lambda_1} \mid t \mid = 1 \tag{A.8}$$

from which one finds

$$Q(t,h) = \mid t \mid^{(d-\lambda_2)/\lambda_1} Q\left(\pm 1, \frac{h}{\mid t \mid^{\lambda_2/\lambda_1}}\right) \tag{A.9a}$$

$$\equiv \mid t \mid^{(d-\lambda_2)/\lambda_1} \tilde{Q}\left(\frac{h}{\mid t \mid^{\lambda_2/\lambda_1}}\right) \tag{A.9b}$$

similarly,

$$\chi(t,h) = |t|^{-(2\lambda_2-d)/\lambda_1}\,\chi\left(\pm 1, \frac{h}{|t|^{\lambda_2/\lambda_1}}\right) \tag{A.10a}$$

$$\equiv |t|^{-(2\lambda_2-d)/\lambda_1}\,\tilde{\chi}\left(\frac{h}{|t|^{\lambda_2/\lambda_1}}\right) \tag{A.10b}$$

Now, invoking standard results expressed in equations (1.1a) and (1.1c), one finds

$$\beta = \frac{d-\lambda_2}{\lambda_1} \tag{A.11a}$$

$$\gamma = \frac{2\lambda_2-d}{\lambda_1} \tag{A.11b}$$

so that finally the scaling fields can be written explicitly:-

$$\mu_1 = a_1 b^{1/\nu} t \tag{A.12a}$$

$$\mu_2 = a_2 b^{d-\beta/\nu} h \tag{A.12b}$$

where a_1 and a_2 are system-specific constants and the scaling laws $\alpha = 2 - \nu d$ and $\alpha + 2\beta + \gamma = 2$ have been used.

Appendix B

Parallel Computation

B.1 The DAP Architecture and Parallel Mapping Strategy

The DAP is a massively parallel SIMD supercomputer which contains either 32×32 (DAP 500 series) or 64 × 64 (DAP 600) Processing Elements (PEs). It is hosted by a UNIX workstation which provides the operating system and program I/O. From the user's point of view, therefore, operation is very straightforward.

The PEs are arranged as a two-dimensional array, the edges of which may be connected together to form a torus topology. This ability to select the hardware configuration from software enhances the range of application of the machine considerably. The PEs can perform variable precision arithmetic and are connected to their nearest-neighbours by high-speed links which provide a very rapid inter-processor communication rate of 1.1 Gbyte/s, making data broadcast very efficient. In addition, the provision of logical masks, allows individual processors to be effectively switched off from parts of the calculation if required.

Each PE has direct connection to its own local memory, the size of which depends upon the individual machine but, for example, that at Edinburgh has 64 kbit

per PE, giving a total of 32 Mbyte. There is no global memory, though there is a separate code store in direct communication with the Master Control Unit (MCU) which issues commands to the processor array. A schematic diagram showing the structure of the DAP is given in figure B.1. All current DAPs have a 10 MHz clock, however, that at Edinburgh is a somewhat older model and runs at 8 MHz. The performance figures quoted below (table B.1) can therefore be updated for the new hardware.

The PEs are simple bit-serial processors which handle all functions (real and integer multiplication, trigonometric functions etc.) in software. This has the disadvantage of some loss of speed compared to handling by hardware, but does allow for a greater range of variable precision than is found normally. A new DAP with 8-bit coprocessors attached to each PE has also recently been released. This addition greatly enhances its performance for integer and floating-point arithmetic. A fuller description of the DAP hardware may be found in reference [112].

The DAP is programmed in an expanded dialect of Fortran called FORTRAN-PLUS which supports a number of parallel datatypes facilitating simple mapping of problems onto the processor array. Table B.1 gives some impression of the arithmetic speed of the DAP 608 when using FORTRAN-PLUS. The figures illustrate certain unusual features, for example a squaring is much faster than a multiplication.

Operation	Rate	Operation	Rate
Real*4 multiply	22.6	Real*4 add	42.2
Real*4 square	43.0	Integer*1 multiply	117
Real*4 saxpy	86	Logical OR	2500
sin(Real*4)	7.6	log(Real*4)	19.2

Table B.1: Rate of operation on the DAP 608 measured in million operations/s

The suitability of the DAP for logical or short length arithmetic is particularly evident from these figures and this feature is exploited for many problems such

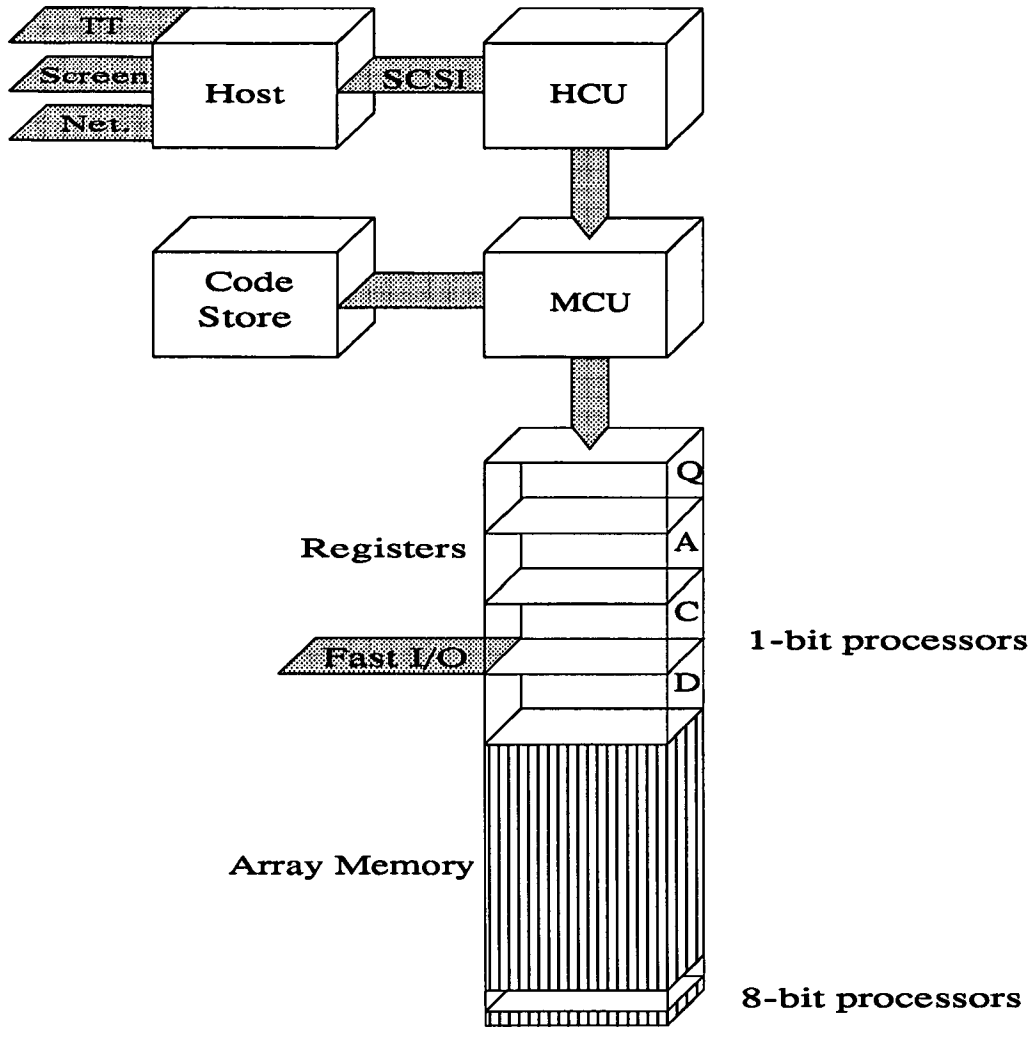

Figure B.1: Schematic diagram of the DAP 610c architecture showing the processor array, its memory and the master control unit. The host computer is also shown.

as Ising model simulations (see below). Nevertheless, even for real arithmetic applications (e.g. the simulations of the Lennard-Jones fluid described in chapter 3), the speed of the DAP 608 is twice as fast as the Cray-1 when both are running an appropriate algorithm.

Data transfer between the host and the DAP is handled by a special purpose SCSI interface which operates at a rate of $1 - 2$ Mbyte/s. A faster data channel for both input and output is also available, this being used predominantly for graphical display. The provision of good graphical visualisation is often essential for the full exploitation of such machines since it can display results in a very direct and immediate fashion.

In common with all parallel computers, a little thought is required prior to writing a DAP program to effect the optimal mapping of a problem onto the machine architecture. In practice, the appropriate mapping almost invariably takes the form of some type of geometrical decomposition in which the total problem is subdivided into a number of subunits, each of which contains one or more interacting subsystems. The programmer then tries to assign one subunit to each processing element such that neighbouring subunits of the problem are mapped onto neighbouring PEs. Such a decomposition ensures that all information transfer between subunits (needed for the calculation of interactions) involves only physically close processors, thereby minimising communications overheads. Once realised, an efficient mapping allows the full exploitation of the SIMD character of the DAP by permitting the simultaneous manipulation of whole matrices of variables.

Whilst the parallel character of the DAP makes it extremely fast for a wide range of problems, it is clear from table B.1 that its performance is most outstanding when dealing with subsystems whose state can be represented by logical variables. This is in contrast to many machines which often wastefully use a byte per logical. In fact, a surprising number of models can be represented in terms of logical variables. The best example is the Ising model, whose spin states take the values $+1$ and -1. In FORTRAN-PLUS, the bit-matrices used to hold these spin states could be easily handled with statements like the following:

```
      logical L(*100,*100)

C
C  Set spins randomly using system-supplied random number generator.
C
      L = RANDOM_SETUP()

      do 10 istep=1, nsteps
        L = FUNC( L, shNc(L), shSc(L), shEc(L), shWc(L) )
   10 continue
```

This declares L to be a two-dimensional (100×100) logical matrix, though the same program structure will hold irrespective of the datatype of L. The '*' in the declaration of L indicates that these dimensions may be operated on in parallel. The interaction function used to calculate the spin flip is expressed by FUNC which operates on the subsystems themselves (stored in L), and their four nearest neighbours each shifted by one lattice spacing in the north, south, east and west directions. These shift functions are part of the FORTRAN-PLUS language, and take only a few machine clock cycles to move a whole matrix. By virtue of the SIMD character of the DAP, all PEs update their elements of L simultaneously.

Since the matrix L is larger than the size of the processor array it is necessary to take into account the mapping of the data structure across the physical array boundaries when performing shift functions etc. In older implementations of the compiler such allowances had to be carried out by the programmer, but in the latest version this is handled by system software and is transparent to the user. Although this has resulted in a considerable increase in ease of use it is still true that the DAP is most efficient when the matrix dimensions are integral multiples of the physical array size.

Despite being a 2-D array of processors, the DAP is nevertheless readily pro-

grammed for 1-D, 3-D and indeed models of any dimensionality. The DAP system software allows a quantity declared as a matrix to be treated as a 1-D array known as a long-vector, with the differences in connectivity handled by the system software at a little loss of speed. Problems involving dimensionality greater than two are handled by using stacks of matrices. In general, programming is simplest if one restricts the parallelism to 2-D with serial looping over higher dimensions. However more sophisticated mapping strategies have been developed [113].

Bibliography

[1] H. E. Stanley, *Introduction to Phase Transitions and Critical Phenomena*, (Oxford : Clarendon 1971).

[2] S-K. Ma, *Modern Theory of Critical Phenomena*, (Benjamin, New York, 1976).

[3] D. J. Wallace and R. K. P. Zia, Rep. Prog. Phys. **41**, 1 (1978).

[4] M. E. Fisher, Rev. Mod. Phys. **46**, 597 (1974).

[5] B. Widom, J. Chem. Phys. **43**, 3892 (1965); J. Chem. Phys. **43**, 3895 (1965);

[6] L. P. Kadanoff, Physics **2**, 263 (1966).

[7] J. M. H. Levelt Sengers, Physica, **73**, 73 (1974).

[8] M. F. Collins, *Magnetic Critical Scattering*, (Oxford U.P., 1989).

[9] B. M. McCoy and T. T. Wu *The Two-dimensional Ising Model* (Harvard University Press, Harvard, 1973).

[10] D. S. Gaunt and A. J. Guttman, in *Phase Transitions and Critical Phenomena*, Vol 3, C. Domb and M. S. Green (eds) (Academic Press : London, 1974).

[11] J. V. Sengers and J. M. H. Levelt-Sengers, in *Progress in Liquid Physics* (Wiley, Chichester, U.K., 1978)

[12] A. D. Bruce and R. A. Cowley, *Structural Phase Transitions*, (London : Taylor and Francis, 1981).

[13] D.P. Belanger and H. Yoshizawa, Phys. Rev. B **35** 10, 4823-4830 (1987).

[14] R. Hocken and M.R. Moldover, Phys. Rev. Lett. **37**, 1, 29-32 (1976).

[15] W. B. Yelon, D. E. Cox, P. J. Kortman and W. B. Daniels, Phys. Rev. **B9**, 4843 (1974).

[16] Als-Nielsen J., Dietrich, O.W. and Passell, L. (1976). Phys. Rev. **B14**, 4908 (1976).

[17] M. E. Fisher, in *Critical Phenomena*, edited by M. S. Green, *Proc. 51st Enrico Fermi Summer School, Varena, Italy* (Academic : New York, 1971).

[18] M. Suzuki, Prog. Theo. Phys. **58**, 1142 (1977).

[19] H. Cramér *Mathematical Methods of Statistics* (Princeton NJ : Princeton University Press 1946)

[20] A. D. Bruce J. Phys. C **14** 3667 (1981).

[21] K. Binder, Z. Phys. B **43** 119 (1981); Ferroelectrics **73**, 43 (1987).

[22] D. Nicolaides and A. D. Bruce, J. Phys. A. **21**, 233 (1988).

[23] M.E. Fisher, Essays in Physics, Vol. 4 (London Academic Press), pp 43–89.

[24] J. F. Currie, J. A. Krumhansl, A. R. Bishop, and S. E. Trullinger, Phys. Rev. **B22**, 477 (1980).

[25] J. A. Krumhansl and J. R. Schrieffer, Phys. Rev. **B11**, 3535 (1975).

[26] G. A. Baker Jr, Phys. Rev. Lett. **60**, 1844 (1988).

[27] C. Domb, Adv. Phys. **9**, 149 (1960).

[28] F. Oberhettinger, *Fourier Transforms of Distributions and their Inverses*, (New York: Academic Press, 1973).

[29] D. Isaacson, Commun. Math. Phys. **53**, 257 (1977).

[30] A. D. Bruce J. Phys. **A18**, L873 (1985).

[31] K. Binder and D. W. Heermann (eds.) *Monte Carlo Simulation in Statistical Physics* (Berlin: Springer, 1988).

[32] N.B. Wilding, A. S. Trew, K.A. Hawick and G.S. Pawley Proc IEEE **79**, 574 (1991).

[33] J. Hubbard and P. Schofield, Phys. Lett. **A40**, 245 (1972).

[34] A. Levelt-Sengers, R. Hocken and J.V. Sengers, Phys. Today. **30**, 42 (1977); P. C. Hohenberg, in *Microscopic Structure and Dynamics of Liquids*, eds. J. Dupuy and A.J. Dianoux (Nato ASI, Corsica, France, 1977); J. V. Sengers, in *Phase Transitions*, eds. M. Levy, J. C. Le Guillou and J. Zinn-Justin (Nato ASI, Cargése, 1980).

[35] J. V. Sengers and J. M. H. Levelt-Sengers, Ann. Rev. Phys. Chem. **37**, 189 (1986).

[36] O. T. Valls and J. A. Hertz, Phys. Rev. B.**18**, 2367 (1978).

[37] J. F. Nicoll and R. K. P. Zia, Phys. Rev. B. **23**, 6157 (1981).

[38] A. Parola and L. Reatto, Phys. Rev. A. **31**, 3309 (1985).

[39] F. Van Dieren and J. M. J. Van Leeuwen, Physica A. **128**, 383 (1984).

[40] L. Reatto, A. Meroni and A. Parola, J. Phys. Condens. Matter **2**, SA121 (1990).

[41] A. Parola and L. Reatto, Phys. Rev. A. **31**, 3309 (1985).

[42] R. E. Goldstein, A. Parola, N.W. Ashcroft, M. W. Pestak, M. W. H. Chan, J.R. de Bruyn and D. A. Balzarini, Phys. Rev. Lett. **58**, 41 (1987).

[43] R.E. Goldstein and A. Parola, J. Chem. Phys. **88**, 7059 (1988).

[44] M. W. Pestak, R. E. Goldstein, M. W. H. Chan, J. R. de Bruyn, D. A. Balzarini and N. W. Ashcroft, Phys. Rev. B. **36**, 599 (1987).

[45] J. J. Rehr and N. D. Mermin, Phys. Rev. A. **8**, 472 (1973).

[46] J. F. Nicoll, Phys. Rev. A. **24**, 2203 (1981).

[47] J. Weiner, K. H. Langley and N. C. Ford, Phys. Rev. Lett. **32**, 879 (1974).

[48] S.C. Greer, B. K. Das, A. Kumar and E. S. R. Gopal, J. Chem. Phys. **79**, 4545 (1983).

[49] S. Jungst, B. Knuth and F. Hensel, Phys. Rev. Lett. **55**, 2167 (1985).

[50] R. R. Singh and K. S. Pitzer, J. Chem. Phys. **92**, 3096 (1990).

[51] U. Narger and D. A.Balzarani, Phys. Rev. B. **42**, 6651 (1990) .

[52] J. A. Barker, D. Henderson, Rev. Mod. Phys. **48**, 587 (1976).

[53] H. K. Kim and M. W. H. Chan, Phys. Rev. Lett. **53**, 170 (1984).

[54] D. J. Adams, Mol. Phys. **37**, 211 (1979).

[55] J. P. Hansen and L. Verlet, Phys. Rev. **184**, 151 (1969).

[56] J. A. Barker, D. Henderson and F. F. Abraham, Physica A. **106**, 226 (1981).

[57] J. J. Nicolas, K. E. Gubbins, W. B. Streett and D. J. Tildesley, Mol. Phys. **37**, 1429 (1979).

[58] K. Binder (ed.) *Applications of Monte-Carlo Methods in Statistical Physics* (Springer, Berlin-Heidelberg, 1984).

[59] M. Rovere, D. W. Heermann and K. Binder, Europhys. Lett. **6**, 585 (1988).

[60] M. Rovere, D. W. Heermann and K. Binder, J. Phys. C. **2**, 7009 (1990).

[61] N. B. Wilding and A. D. Bruce, in preparation (1991).

[62] F. J. Wegner, Phys. Rev. B. **5**, 4529 (1972).

[63] M. P. Allen and D. J. Tildesley. *Computer Simulation of Liquids*, (Oxford University Press 1987).

[64] D. J. Adams, Mol. Phys. **29**, 307 (1975).

[65] K. K. Mon and K. Binder, Mainz preprint (1991).

[66] F. Tsien and J. P. Valleau, Mol. Phys. **27**, 177 (1974).

[67] D. Henderson, Mol. Phys. **34**, 301 (1977).

[68] R. R. Singh, K. S. Pitzer, J. J. de Pablo and K. M. Prausnitz, J. Chem. Phys. **92**, 5463 (1990).

[69] M. Mezei, Mol. Phys. **40**, 901 (1980).

[70] R. H. Swendsen and J. S. Wang, Phys. Rev. Lett. **58**, 86 (1987).

[71] Xiao-Jian Li and A. D. Sokal, Phys. Rev. Lett. **67**, 1482 (1991).

[72] U. Wolff, Phys. Rev. Lett. **62**, 361 (1989).

[73] F. Niedermayer, Phys. Rev. Lett. **61**, 2026 (1988).

[74] R. C. Brower and P. Tamayo, Phys. Rev. Lett. **62**, 1087 (1989).

[75] D. Kandel and E. Domany, Phys. Rev. B. **43**, 8539 (1991).

[76] Z. S. Kooner and W. A. Van Hooke, J. Phys. Chem. **92**, 6414 (1988).

[77] A. I. Kitaigorodsky, *Molecular Crystals and Molecules*, Physical Chemistry **29** (1973).

[78] A. I. Kitaigorodski, "Molekularnyje Kristaly", Izd. Nauka, Moscow (1971).

[79] D. Cavagnat, M. P. Roberts, R. M. Cavagnat and S. Vahedir-Banisaeid, J. Phys. Chem. **95**, 134 (1991).

[80] G. Dosseh, C. Fressigné, B. Rousseau, N. B. Wilding and A. H. Fuchs, J. Chim. Phys. **87**, 1821 (1990).

[81] E. R. Andrew and R. G. Eades, Proc. Roy. Soc. **A216**, 398 (1953).

[82] R. Kahn, R. Fourme, D. André and M. Renaud, Acta. Cryst. **B29**, 131 (1973).

[83] M. Renaud and R. Fourme, J. Chim . Phys. **63**, 27 (1967).

[84] A. Würflinger, Ber. Bunsenges. Phys. Chem. **79**, 1195 (1975).

[85] L. Schulte and A. Würflinger, J. Chem. Thermodynamics, **19**, 363 (1987).

[86] J. Haines and D. F. R. Gilson, J. Phys. Chem. **93**, 7920 (1989).

[87] J. Haines and D. F. R. Gilson, J. Phys. Chem. **94**, 4712 (1990).

[88] W. C-K. Poon, J. C. Crain, P. D. Hatton and A. Cairns-Smith, Edinburgh preprint (1991).

[89] J. Mayer, J. Chrusciel, S. Habrylo, K. Holderna, I. Natkaniec, M. Hartmann, A. Würflinger, S. Urban, W. Zajac, High Pressure Research, **4**, 460 (1990).

[90] J. Mayer, J. Chrusciel, S. Habrylo, K. Holderna, I. Natkaniec, M. Hartmann, A. Würflinger, S. Urban, W. Zajac, Phys. Stat. Sol. **B166**, 381 (1991).

[91] N. B. Wilding, P. D. Hatton and G. S. Pawley, Acta. Cryst. **B47**, 797 (1991).

[92] G. E. Bacon, *Neutron Scattering* (Oxford Univ. Press, 1962).

[93] R. B. von Dreele in Los Alamos Science, Neutron Scattering **19** (1990).

[94] A. W. Hewat and I. Bailey, Nucl. Instrum. Methods **137**, 463 (1976).

[95] E. Baharie and G. S. Pawley, J. Appl. Cryst. **10**, 465 (1977).

[96] R. Shirley, in *Crystallographic Computing*, ed H. Schenk, R. Olthof Hazekamp, H. van Koningsveld, and G. C. Bassi, (Delft University Press, Holland, 221, 1978).

[97] F. Kohlbeck, and E. M. Hörl, J. Appl. Cryst. **11**, 60 (1978).

[98] P. M. de Woolf, J. Appl. Cryst. **1**, 108 (1968).

[99] G. S. Pawley, J. Appl. Cryst. **14**, 357 (1981).

[100] A. S. Trew, G. S. Pawley and A. Cairns–Smith, Acta Cryst. **A46**, 979 (1990).

[101] D. E. Williams, J. Chem. Phys. **47**, 4680 (1967).

[102] H. M. Rietveld, J. Appl. Cryst. **2**, 65, (1969).

[103] J. K. Cockcroft, PROFIL program, ILL Grenoble (1989).

[104] K. B. Wiberg, V. A. Walters and W. P. Dailey, J. Am. Chem. Soc. **107**, 4860 (1985).

[105] V. K. Belsky and P. M. Zorkii, Acta. Cryst. **A33**, 1004 (1977).

[106] K. Refson and G. S. Pawley, Acta. Cryst. **B42**, 402 (1986)

[107] K. Refson and G. S. Pawley, Acta. Cryst. **A43** 727 (1987).

[108] C. J. Craven, P. D. Hatton and G. S. Pawley, Edinburgh preprint (1991).

[109] A. Würflinger and J. Kreutzenbeck, J. Chem. Solids **39**, 193 (1978); K.D. Wisotzki and A. Würflinger, J. Phys. Chem. Solids **43** 13 (1982).

[110] M. Parrinello and A. Rahman, Phys. Rev. Lett. **45**, 1196 (1980).

[111] G. Burns and F. H. Dacol, Solid State Comms. **51**, 773 (1984).

[112] A. S. Trew and G. V. Wilson, (eds.) *Past, Present, Parallel. A Survey of Available Computing Systems.* (London, U. K.: Springer-Verlag, 1991).

[113] G. S. Pawley and G. W. Thomas, J. Comput. Phys. **47**, 165 (1982).